LBL-35119
UC-414

ERNEST ORLANDO LAWRENCE BERKELEY NATIONAL LABORATORY

Microstructure-Interface-Property Relationships in Nanometer-Period X-Ray Multilayers

Tai Dung Nguyen
Materials Sciences Division

December 1996
Ph.D. Thesis

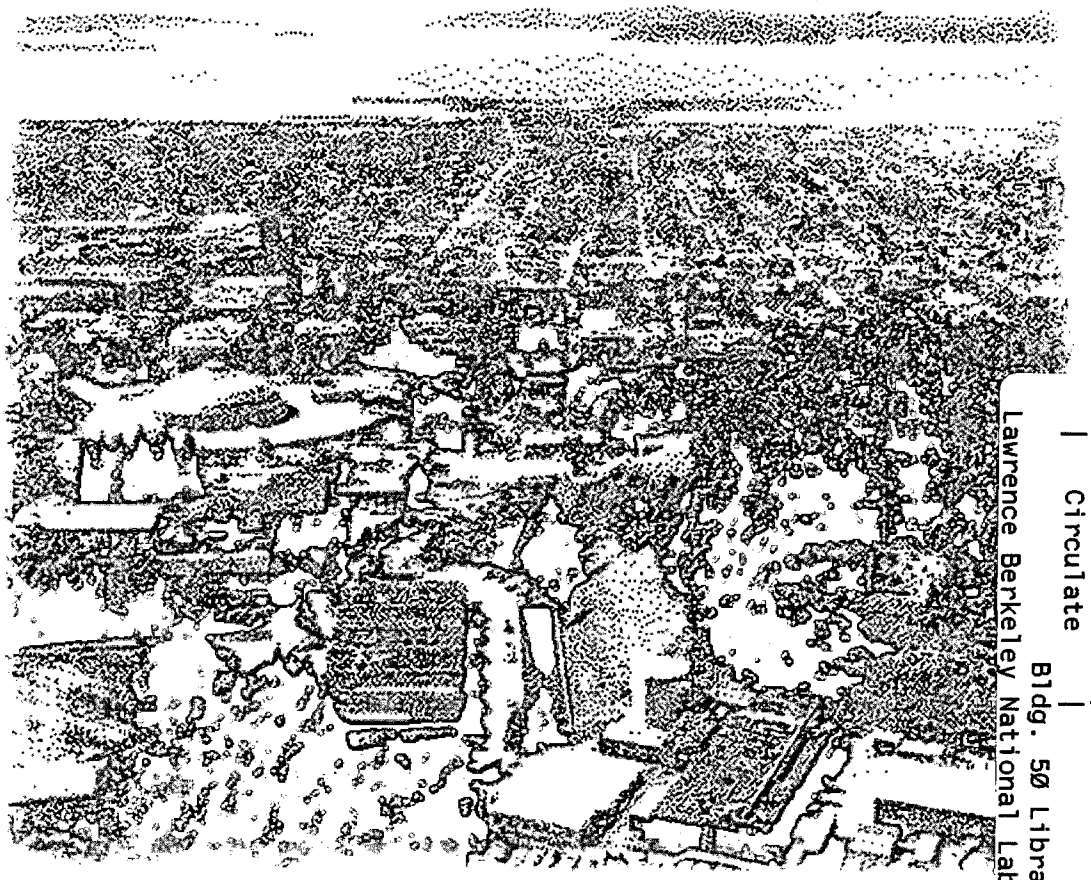

REFERENCE COPY
Does Not
Circulate
Bldg. 50 Library - Ref.
Lawrence Berkeley National Laboratory
Copy 1
LBL-35119

DISCLAIMER

This document was prepared as an account of work sponsored by the United States Government. While this document is believed to contain correct information, neither the United States Government nor any agency thereof, nor the Regents of the University of California, nor any of their employees, makes any warranty, express or implied, or assumes any legal responsibility for the accuracy, completeness, or usefulness of any information, apparatus, product, or process disclosed, or represents that its use would not infringe privately owned rights. Reference herein to any specific commercial product, process, or service by its trade name, trademark, manufacturer, or otherwise, does not necessarily constitute or imply its endorsement, recommendation, or favoring by the United States Government or any agency thereof, or the Regents of the University of California. The views and opinions of authors expressed herein do not necessarily state or reflect those of the United States Government or any agency thereof or the Regents of the University of California.

LBL-35119
UC-414

Microstructure-Interface-Property Relationships in Nanometer-Period X-Ray Multilayers

Tai Dung Nguyen
Ph.D. Thesis

Department of Applied Science and Technology
University of California, Berkeley

and

Materials Sciences Division
Ernest Orlando Lawrence Berkeley National Laboratory
University of California
Berkeley, CA 94720

December 1996

This work was supported by the Director, Office of Energy Research, Office of Basic Energy Sciences, Materials Sciences Division, of the U.S. Department of Energy under Contract No. DE-AC03-76SF00098.

Microstructure - Interface - Property Relationships in Nanometer-Period X-Ray Multilayers

by

Tai Dung Nguyen

B.A. (University of California at Berkeley) 1987
M.S. (University of California at Berkeley) 1990

A dissertation submitted in partial satisfaction of the

requirements for the degree of

Doctor of Philosophy

in

Applied Science and Technology

in the

GRADUATE DIVISION

of the

UNIVERSITY of CALIFORNIA at BERKELEY

Committee in charge:

Professor Ronald Gronsky, Chair
Professor David T. Attwood
Dr. Jeffrey B. Kortright
Professor Andreas Glaeser

1993

Abstract

The microstructure - interface - property relationships in nanometer-period x-ray multilayer mirrors (W/C, WC/C, Cr/C, CrC/C, Cu/C, Ru/C, and Ru/B_4C) were studied using cross-sectional high resolution TEM and x-ray scattering. Microstructural and morphological evolution of as-prepared multilayers, and their behavior under thermal activation were discussed in terms of the materials' thermodynamic and kinetic properties. Effects of the microstructural and the morphological evolution in reactive-component (W-C, Cr-C, and Ru-B_4C) and conjugate-component (Ru-C and Cu-C) multilayers on the normal incidence reflectance and long term stability of the mirrors are presented.

The microstructure of the metal layers in all as-prepared multilayers changes with period, evolving from amorphous at short period to polycrystalline at longer period, while the layers in the alloy/C multilayers retain an amorphous structure for all periods. Formation of the crystalline phase in the metal layers of metal/C multilayers depends on the thickness of the amorphous alloy layers at the interfaces, which result from intermixing and interdiffusion between the layer materials. Immiscibility and limited mutual solubility in conjugate-component multilayers promotes phase separation, and interfacial instead of volume diffusion, which leads to nucleation of the crystalline phase at shorter period than in reactive-component multilayers. As-prepared conjugate-component (Ru/C) exhibit higher normal incidence reflectance than reactive-component (Ru/B_4C) multilayers at $\lambda = 7$ nm.

Annealing of the multilayers at 500°C and 600°C results in compound formation (W_2C, RuB_2 in W/C, Ru/B_4C, respectively), solid state amorphization (Cr/C), and agglomeration (Ru/C) in the metal-rich layers. Crystallization of W_2C occurs at lower temperatures than those recorded in the equilibrium phase diagram due to size effects. Fast C diffuser and interdiffusion lead to solid state amorphization reactions in Cr/C

multilayers. The alloy/C multilayers (WC/C and CrC/C) remains amorphous after annealing, because nucleation and grain growth of stable intermetallic compounds may require uphill diffusion of C atoms. High C content in short period amorphous reactive-component multilayers (W/C, WC/C, Cr/C, CrC/C, and Ru/B_4C) stabilizes the layered structure upon annealing. Crystallization and agglomeration in short period conjugate-component Ru/C multilayers, driven by the reduction of the interface to volume ratio and occur via interfacial diffusion and cross-layer diffusion, are discussed in relation to thin film instability and edge spheroidization. A greater reduction in the reflectance of the Ru/C than in Ru/B_4C multilayers is observed due to this agglomeration. Hence reactive-component multilayers are expected to be more stable than conjugate-component multilayers in high temperature and long term applications.

Con kính cúng Ba ...

và kính Mẹ.

(To my late Father ...

and my Mother.)

TABLE OF CONTENTS

Title page i
Abstract
Dedications iii
Table of contents iv
Acknowledgements vii

1. INTRODUCTION 1
    1.1 Short Period X-Ray Multilayers 1
    1.2 Historical Perpective of X-ray Multilayers 4
    1.3 Motivation for the Study 6
    1.4 Goals and Scope of the Study 12
    1.5 Review of Literature 15
    1.6 Organization of the Thesis 17
    1.7 References 18
    1.8 Figures 20

2. EXPERIMENTAL PROCEDURE 24
    2.1 Fabrication of Multilayers 24
    2.2 Normal Incidence Reflectance Measurement 25
    2.3 Annealing 26
    2.4 X-ray Scattering 27
    2.5 Transmission Electron Microscopy 28
        2.5.1 Cross-section TEM Specimen Preparation 28
        2.5.2 Plan-view Sample Preparation 29
        2.5.3 Transmission Electron Microscopy 30
        2.5.4 Image Interpretation 31
    2.6 References 31
    2.7 Figures 32

3. TEM MICROSTRUCTURAL RESULTS 36
    3.1 W/C System 36
    3.2 WC/C System 37
    3.3 Cr/C System 38
    3.4 CrC/C System 40
    3.5 Ru/C System 40
        3.5.1 Microstructural Evolution 41
        3.5.2 *In-situ* TEM Studies 46
        3.5.3 Ru Grain Size Distribution Studies 48
    3.6 Ru/B_4C System 50
    3.7 Cu/C System 51
    3.8 Tables 52
    3.9 Figures 53

4. DISCUSION ON MICROSTRUCTURAL AND MORPHOLOGICAL EVOLUTION 81
4.1 As-prepared Microstructure 81
4.1.1 Conjugate-Component Multilayers 82
4.1.2 Reactive-Component Multilayers 84
4.2 Thermal Stability 88
4.2.1 Diffusion in Steep Concentration Gradient Multilayer Structures 88
4.2.2 Compound Formation: W/C and Ru/B_4C 90
4.2.3 Solid State Amorphization Reaction: Cr/C 93
4.2.4 Stability of the Amorphous Phase: WC/C and CrC/C 99
4.2.5 Phase Separation: Ru/C and Cu/C 100
4.2.5.1 Agglomeration in Ru/C 100
4.2.5.1.1 Instability and Agglomeration 101
4.2.5.1.2 Discussion on Ru/C 104
4.2.5.2 Immiscibilty in Ru-C and W_2C-C 111
4.2.5.3 Clustering in Cu/C 113
4.3 References 114
4.4 Figures 116

5. IMPLICATIONS TO X-RAY APPLICATIONS 135
5.1 Microstructure and Layered Structure Stability 135
5.1.1 Effects of Microstructural and Interfacial Roughness on Reflectance of Ru/C and Ru/B_4C Multilayers 138
5.1.1.1 Background 138
5.1.1.2 Normal Incidence Reflectance Measurements 138
5.1.1.3 High Angle X-ray Scattering 139
5.1.1.4 Specular and Non-Specular Scattering 139
5.1.1.5 Analysis of X-ray Result 141
5.1.1.6 Effects on X-ray Optical Properties 143
5.2 Period Expansion in Metal/C Multilayers 144
5.3 References 146
5.4 Tables 147
5.5 Figures 147

6. SUMMARY 154
6.1 Conclusions of the Research 154
6.2 Suggestions for Future Research 158

APPENDIX A. OPTICS OF MULTILAYER STRUCTURES 160
A.1 Optical Properties at Short Wavelengths 160
A.2 Reflection at an Interface 162
A.3 Calculation of Multilayer Reflectance 164
A.4 Multilayer Imperfections 165
A.5 References 167

APPENDIX B. EFFECTS OF FRESNEL FRINGES ON INTERPERTATION OF INTERFACIAL STRUCTURES IN MULTILAYERS FROM CROSS-SECTIONAL HRTEM IMAGES 168
B.1 Introduction 168
B.2 Simulation of Fresnel Fringes 171
B.3 Experimental TEM Observation of Fresnel Fringes 173
B.4 Conclusions 174
B.5 References 174
B.6 Figures 175

ACKNOWLEDGEMENTS

I would like to express my appreciation to my two advisors, Prof. Ronald Gronsky and Dr. Jeffrey B. Kortright, for their guidance and support throughout the course of this study. I would like to thank Prof. D. Attwood and Prof. A. M. Glaeser for reviewing this thesis. Special thanks to the whole committee for reading the thesis in such short time.

I would like to thank the scientists, staff, and fellow students at both CXRO and NCEM, for many useful discussions and supports. All those in Gronsky's group, those involed in MRSUC, and electron microscopy deserve a thankyou note. Special thanks to Z. Weng for proof-reading part of this thesis.

I would like to thank all my friends and relatives for their helps and encouragements. Very special thanks to my two brothers and sister-in-law, who always believe in me, and understand of what it took to finish this thesis.

And as for any other achievement, I would like to dedicate this work to my parents, especially my late father. I wish he could be here to see this.

CHAPTER 1

INTRODUCTION

1.1 SHORT PERIOD X-RAY MULTILAYER MIRRORS

Since the day W.C. Roentgen discovered x-rays in 1895, it has been a challenge to find ways to diffract this radiation or otherwise focus it for useful applications. For a long time, metal surfaces were used to diffract and reflect x-rays. The development of x-ray optical technology has relied upon the properties of total external reflection and upon the use of natural crystals to obtain high reflectance from single surfaces. Total external reflection in fact has formed the basis for the oldest known x-ray optical mirror technology with the use of metals as total reflection mirrors. When x-rays are incident on a surface, part of the radiation is diffracted or reflected, and part is transmitted and absorbed. In an analogy to total internal reflection at visible wavelengths, there is a critical angle θ_c measured from the surface, such that if the incident angle is less than θ_c, none of the beam is transmitted or absorbed, and thus 100% of the incident beam is reflected back into the incident medium. Since the index of refraction of materials is slightly less than unity at x-ray wavelengths, however, this property is called total external reflection, the process by which a beam is totally reflected when incident on the surface of materials in a vacuum. The critical angle of most metals is usually very small, typically less than 5°. The use of total external reflection, for example, as reflecting mirrors thus is limited to glancing incidence applications.

High reflection at angles and wavelengths determined by $\lambda = 2 \cdot d \cdot \sin\theta$ however can be obtained from natural crystals in the form of constructive interference of waves reflected from periodic lattice planes in the crystals. This x-ray mirror technology is obviously limited by the availability of natural crystals. Since the lattice spacing of most crystals is only a few angstroms in dimension, these mirrors can provide high reflectance only at hard x-ray wavelengths, namely a few angstroms or less.

At soft x-ray wavelengths and at angles that are higher than the critical angle, reflectance of radiation from a surface is generally very small, typically only 10^{-4} to 10^{-8} of the incident intensity. Reasonable reflectors however can be obtained from structures containing many surfaces or interfaces. Since the intensity is proportional to the square of the electric field amplitude, the amplitude reflection coefficient is proportional to the absolute value of the square root of the reflectivity coefficient, of the order of 10^{-2} to 10^{-4}. Neglecting absorption, a reflectivity approaching 100% thus can be achieved by constructive interference of amplitudes from 100 to 10,000 interfaces with the proper phase relationships.[1]

Multilayer structures of properly designed interfaces provide such constructive interference for high reflectance. Ideally, x-ray reflectors consist of alternating layers of two different materials (e.g., A and B) with different refractive indices, that form an artificially modulated sequence ABAB. The thicknesses of the layers are typically periodic, such that each bilayer (AB) makes up one period of the multilayer. A schematic drawing of such a multilayer is shown in Figure 1-1. The high reflectivity of multilayer structures is achieved from constructive interference of waves reflected from these periodically spaced interfaces. When radiation of wavelength λ is incident at an angle θ on the planes, each interface will specularly reflect and transmit amplitudes given by the Fresnel coefficients.[2] A full treatment of reflection optics from a single

surface and from multilayers is given in appendix A. If the scattered waves constructively add in phase, they will sum to a maximum amplitude at the Bragg angles θ_n, given by:

$$n \cdot \lambda = 2 \cdot d \cdot \sin\theta, \qquad [1\text{-}1]$$

which is known as Bragg's law. Multilayer structures hence are analogous to crystal mirrors, in which the multilayer period is equivalent to the lattice plane spacing which has roughly atomic dimensions. In a manner similar to the crystalline structures then, the multilayers can diffract and reflect incident radiation, but at longer wavelengths since each period is composed of many atomic distances. For applications in the ultra-violet and soft x-ray regions, the period of these multilayers is on the order of nanometers, depending upon the wavelength and angle of incidence.

Multilayer interference reflectors provide certain advantages in experiments over total external reflection and crystal mirrors. As can be seen from Bragg's law, control of the multilayer period can provide high reflectance at a specific angle and wavelength over a broad range. X-ray multilayers, however, have been used mainly in two limiting applications: normal incidence reflecting mirrors at wavelengths in the extreme ultra-violet (EUV) and soft x-ray regions, and grazing incidence mirrors at wavelengths approaching the hard x-ray region. Compared to total external reflection mirrors, multilayers offer high reflectance at an angle higher than θ_c, which has the advantage that in some cases aberrations are reduced. Compared to natural crystals, multilayers extend high reflectance to the region longer than hard x-ray wavelengths. In addition, multilayer mirrors can be coated onto curve surfaces for interesting applications.

1.2 A HISTORICAL PERPECTIVE OF X-RAY MULTILAYERS

The concept of multilayer structures as x-ray reflectors in fact has been realized since the beginning of the century. The principles were suggested as analogous to the methods Gabriel Lippmann used in color photography, work for which he received the 1908 Nobel Prize in Physics.[3] In this method, the silver halide grains in the film plate are exposed to the incident light waves with an intensity corresponding to the nodes and antinodes of the waves. After development of the film plate, the silver grains appear in multiple layers at the planes of the antinodes of the interfering light waves, where these grains received maximum exposure. When the film is exposed with light, the silver layers reflect light of the original wavelength and produce the image. Using the same concept, Koeppe[4] and Deubner[5] reasoned that multilayers of comparable period to x-ray wavelengths will be able to diffract x-rays at high efficiency. They tried to make multilayer structures by electroplating thin layers of Au and Ag onto a substrate, and were able to observe x-ray diffraction from the crystal structures with individual layers, but not from the layered structure.

It was until 1940 that DuMond and Youtz first reported diffraction of Mo K radiation from Au/Cu multilayers.[6] The periodic Au/Cu multilayer structures were prepared by evaporation, having an average interplanar thickness of approximately 10 nm. The superlattice diffraction however decayed in a few weeks due to loss of the modulated structure resulting from interdiffusion between the gold and copper. Attempts to make stable multilayer structures were continued in the 1960s by Dinklage and Frerichs,[7] who used magnesium as one of the components in the structures. Dinklage had reported that iron/magnesium multilayers with a period between 3 and 5 nm remained layered for more than a year.[8] Later developments in the history of multilayer structures concentrated more on fabrication techniques that allowed

deposition of nanoscale layers, and on long term stability of the thin layers. In the 1970s, Spiller made successful multilayer mirrors for normal incidence reflection.[9] These multilayer structures were typically larger than 10 nm in period, and thus applicable in the soft x-ray region. About the same time, Barbee and Keith refined sputtering techniques for depositing layers of materials as thin as a few angstroms.[10] Based on their work, high efficiency dispersing elements for glancing incidence Cu K radiation with a period of about 2 nm were reported. At present, many groups and laboratories are working on the refinement of existing multilayer structures, extension to new material combinations, and a variety of related techniques, to achieve higher reflectivities at all wavelengths.

Recent increased development of multilayer mirrors owes to the increased interests in using x-ray mirrors in x-ray spectroscopy, imaging, laser and synchrotron radiation research. High reflectance mirror optics in x-ray microscopes yield enhanced high energy bandpass, and reduce aberrations.[11-12] Multilayers are used to focus x-ray beams, and are used as cavity mirrors in lasers in the EUV and soft x-ray regions for multipass amplification.[13] Many other uses and applications of multilayer structures were discussed extensively at a conference on applications of thin-film multilayer structures to configured x-ray optics.[14] More recent application of multilayer mirrors is in the optics of reduction x-ray projection lithography.[15-18] In these applications, 50% or higher reflectivity from the multilayers is needed for proposed multiple reflection imaging systems. Normal incidence peak reflectivities of less than 30%, however, have been reported in the 4 to 10 nm region,[1] and in the 30 to 45 nm region. The highest reflectivity in the EUV and soft x-ray regions has been obtained from multilayers containing Mo and Si at wavelengths above the Si $L_{2,3}$ edge. Silicon is chosen as one of the layer materials because it exhibits the least absorption at wavelengths above its absorption edge. Normal incidence reflectance in excess of 60% has been reported by

various groups at wavelengths near 13 nm.[19-22] Below the Si edge, the reflectance from this multilayer system decreases significantly due to the high absorption in the Si layers. At wavelengths shorter than 13 nm, reflectivity of only 30% or less has been achieved with other materials combinations, even near the boron (6.8 nm) and carbon (4.4 nm) edges. In the region between the Si and the C edges, most high efficient normal incident multilayers contain carbon or boron in their layers for absorption. For grazing incidence, reflectivities of higher than 60% have been demonstrated with W/C and other multilayers in the soft x-ray to x-ray spectral regions.[23]

1.3 MOTIVATION FOR THE STUDY

Calculations of optimized reflectivities of radiation with wavelengths from about 1 to 10 nm demonstrate that by selection of optimum materials and number of periods, reflectivities can be quite large, ranging from 40 to 80%.[24] Discrepancies between calculated normal incident reflectance and measured reflectance are quite large, and increase with decreasing wavelength. Practical multilayers have achieved peak reflectivities that are at most only 70% of the calculated values. Figure 1-2 shows the normal incidence reflectance in the wavelength region from approximately 15 to 4.5 nm that has been obtained at the Center for X-Ray Optics, Lawrence Berkeley Laboratory.[25] Included in the figure are the measured reflectivity of Ru/C multilayers, and the calculated reflectivity of these multilayers assuming ideal structure and interfaces. As can be seen from the figure, the calculated reflectivities of the multilayers are found to decrease with wavelength. The ideal reflectivity is approximately 45% at 10 nm, 30% at about 7 nm, and less than 20% at near 4.5 nm wavelength. The measured reflectivities seem to follow the trend of the calculated reflectivities with period. They are near 30% at 10 nm, 12% at 7 nm, and about 6% at 4.5 nm wavelength. The measured reflectivities

however deviate further from the ideal reflectivity as the wavelength decreases. The ratio of the measured to the calculated reflectance at 10 nm is more than 66%, while that of the 4.5 nm wavelength is only 33%. Discrepancies between calculated and experimentally achievable values arise because the idealized model used for the calculations assumes that multilayers are perfectly flat and regular with sharply defined interfaces. Uncertainties in the refractive index data at x-ray wavelengths also add to the discrepancies in the calculations. Typically, the calculated reflectivities are multiplied by a Debye-Waller factor to match with the measured values of the reflectivity. This Debye-Waller factor, among other parameters, includes a rms value σ of the interfacial roughness of the multilayers (see appendix A). For the data in Figure 1-2, a value of the rms interfacial roughness σ between 0.3 and 0.7 nm, with the smaller value for shorter periods, is required for the Debye-Waller factor in the calculation to fit with the measurements.[25] The results suggest that the interfaces in the multilayers are smoother in short period samples.

In practice, the structures of most multilayers are far from the assumed ideal structures. Diffusion and intermixing of the materials at their interfaces for example cause imperfection in the definition of the layers. The evolution of the microstructure inside the layers upon annealing are different for different multilayer systems and depend on the reactions among the materials constituting in the layers. Changes in the microstructure lead to changes in the interfacial structure, and as a result affect the performance and stability of these multilayers. The goals of the research leading to this thesis are: 1) to understand the microstructure-interface-property relationships in nanometer period multilayers that have potential applications at wavelengths less than 10 nm; 2) to understand the effects of the microstructure and different imperfections on the multilayers' performance; 3) to understand the reactions in multilayers in terms of the thermodynamic and kinetic properties of the materials; and 4) to understand the

long term stability of the multilayers under actual operating conditions. The focus of the project is to enhance the performance and the stability of the mirrors, by control of the choice of material combinations and of the reactions of the materials in the multilayers.

The performance of ideally structured multilayers depends upon materials that have sufficiently different x-ray scattering powers, upon the number of bilayer periods, and upon the relative thicknesses of the component layers in a period. In fabrication of the multilayers, the choice of materials depends on their optical properties. The number of periods, and the relative thicknesses of the layers can be controlled during deposition to minimize absorption and maximize diffraction from the layers.[26] Reduction of the multilayer reflectivities from the ideal values results from three main imperfections in the multilayer structures: roughness of the substrate surface that may propagate into the multilayer, variation of the layer thicknesses, and imperfections at the interfaces. The first two factors are extrinsic to the formation of the multilayers, while the last factor is an intrinsic parameter, which depends on the materials characteristics and reactions between the constituents of the multilayers during and after deposition. Imperfections at interfaces can be divided into two different categories: one is the composition gradient across the two materials resulting from interdiffusion of the constituents, and the other is structural roughness at the interfaces. In calculations of the reflectance, the compositional gradient is treated using a step approximation representing the gradient of the optical constants from one layer to the next.[1] Such gradients reduce the calculated reflectance. The effects of the structural roughness at the interfaces are analogous to the thermal diffuse scattering of x-rays in crystals. Structural roughness introduces a diffuse component in the scattering, and reduces the specular reflectance.[27] Optimization of the multilayer performance thus includes choosing constituent materials that undergo minimum inter-layer diffusion and intermixing and that form smooth and uniform interfaces. In real structures, it is often unclear which of the interfacial imperfections,

compositional gradients or structural roughness, has a greater effect on the performance and characteristics of the multilayers. Studies to separate the effects of the intermixing and the structural roughness components on the reduction of the multilayer reflectivity are important because by understanding which effects limit the reflectance, fabrication of improved performance multilayers may be possible. Attempts to determine these effects have been reported recently by different groups.[27-36] Auger depth profiling,[32-33] TEM Fresnel fringe analysis[34-35] and Z-contrast imaging[36] have been used to study the concentration gradients across the interfaces, and specular and non-specular x-ray scattering have been used to quantify the interfacial roughness.[27-31]

The structure at the interfaces in multilayers depends on the microstructures and phases present in the layers of the multilayers. Intermixing from ion bombardment, and interdiffusion between the layers occur during sputtering of the layers. Thermal loading under intense x-ray irradiation in practical applications further induces reactions and phase transformations within the layers, and structural changes at their interfaces within the modulated structures. In normal incidence reflecting mirrors, the thickness of the individual layers in the multilayers is approximately one quarter of the wavelength, which is less than 2.5 nm for wavelengths shorter than 10 nm. Interdiffusion and solid state reactions between the layers occur more readily at thinner layer period such that many phases can be formed at temperatures lower than those recorded in the equilibrium phase diagram. Many systems of artificial modulated structures have been fabricated and studied for different applications such as electronic devices, magnetic multilayers, as well as superlattice and quantum-well structures.[37-43] Modulated structures have also been studied because they provide academically interesting systems to investigate the mechanisms of interdiffusion and reactions in materials.[42-43] Two different types of reactions have been observed in modulated structures under a thermal activation: one in which the layer constituents interdiffuse and react with each others to

form stable compounds or intermetallic alloys (henceforth called reactive-based multilayers), and one in which the layer materials separate from each other (called conjugate-based multilayers). Interdiffusion in modulated structures results from the presence of steep chemical gradients at the interfaces, which provide a driving force for interdiffusion and homogenization of the structures. Depending on the thermodynamic and kinetic characteristics of the materials constituents in reactive-based multilayers, different products may develop under a thermal activation. Interdiffusion and reactions in reactive-based multilayers usually lead to the formation of new phases, which may crystallize or recrystallize from the original crystalline phases in the structures. Coarsening of one of the layers in the structures has been observed in some materials systems under thermal activation.[44] Formation of metastable phases is also highly possible in these small-scale modulated structures. Transformation of an amorphous phase via solid state amorphization reactions of crystalline layers has also been reported in various multilayer systems.[45-47] These reactions result in different interfacial morphologies, including the formation of an interfacial layer, and smoothening or roughening of the interfaces. In conjugate-based multilayers, on the other hand, interdiffusion usually does not occur. The components prefer to remain separated from each other, which in some cases results in more well-defined modulated structures, as observed in spinodally decomposing systems. Agglomeration of the layers however has also been observed in some thin films and multilayers.[48] Crystallization and/or grain growth of the individual component is expected under thermal activation in this type of multilayers. In x-ray multilayers, the individual layer is only of a few atomic layer thick, which causes the system to be very far from an equilibrium state. This strong driving force, and the short diffusion paths in these nano-scale layers, promote the reactions and phase transformation to occur more rapidly, which in some cases results in the presence of equilibrium phases at temperatures lower than those recorded in the bulk equilibrium phase diagrams. Although the as-prepared multilayer structures are not in an

equilibrium state, the equilibrium phase diagrams however can suggest the types of materials components that are suitable for reflective optical applications, and the types of reactions that would occur under a thermal activation. Well-defined layers and sharp interfaces for optimum performance of reflective mirrors require minimum intermixing and interdiffusion between the layers. Materials combinations whose phase diagrams show the presence of a miscibility gap thus are ideal choices, since they possess structures closest to the ideal structures. Conjugate-component multilayers having such materials components hence probably exhibit measured reflectance that are close to the calculated values arising from ideal structures. Long term stability in the performance of the mirrors is also important, and depends on the stability of the layers and of the interfacial structures that result from reactions between the layer constituents under thermal loading in practical applications. It is unclear, however, whether reactions from conjugate- or reactive-component materials produce more dramatic changes in the structures and hence the performance of the mirrors. Studies of conjugate- and reactive-component multilayers and their behavior under thermal treatments would furnish a sound basis for the choice of materials combinations, based on thermodynamic and kinetic properties of these materials, for optimum performance and long term stability.

Studies of the microstructures and phases within the layers of multilayers having different materials combinations, and their evolution under thermal treatments, provide an understanding of the expected reactions in multilayer systems. Studies and comparisons of the microstructures and phases within the layers and at the interfaces of as-prepared and annealed multilayer systems with varying period also provide an understanding of the relationship between microstructure and optical properties in multilayer systems, including the increasing discrepancy between calculated and measured reflectance with decreasing period. Thermal annealing studies of the multilayers provide an understanding of the effects of the choice of the materials and

their reactions upon the long term stability of multilayers. Such understanding would help in the design of high performance, high efficiency, and stable multilayer mirrors.

1.4 GOALS AND SCOPE OF THE STUDY

Although x-ray multilayers have been fabricated and utilized in x-ray optical applications over the last decade, little is known about the structures inside these multilayers, and how they affect the performance and stability of the multilayer mirrors. This research is one of the first to provide a systematic study of different multilayer systems that actually have practical applications in x-ray optics. The goal of this study thus is to develop an understanding of the microstructure - interface - property relationships in x-ray multilayer systems. To understand these relationships, the microstructural evolution of different multilayer systems as a function of periodicity is studied. Thermal annealing of the multilayers is performed to study their behavior under thermal activation, and to obtain an understanding of the effects of the microstructures on the long term stability of the multilayer systems. Reactions and phase transformations observed in multilayers upon annealing are analyzed by comparisons with the known equilibrium materials properties. Although the results obtained in this study are specific to the multilayer systems studied, trends of the microstructural evolution with period under thermal treatments among these different systems can still be observed, and wherever possible, they are related to their optical properties. An understanding of the microstructure - property relationship in these multilayers, while important in itself, may provide a guide to improving current multilayers and in selecting multilayer materials for improved performance and stability in the future. In addition, multilayers are interesting to study because they are novel

nanometer-scale structures with many interesting properties, independent of x-ray applications, and may provide academically stimulating problems and solutions.

In this research, as-prepared and annealed metal and metal-carbon alloy/carbon- and boron-containing multilayers (W/C, WC/C, Cr/C, CrC/C, Cu/C, Ru/C, and Ru/B_4C) of varying periods between 2 and 12 nm are studied by high resolution Transmission Electron Microscopy (HRTEM) and x-ray scattering techniques. X-ray specular and non-specular scattering are sensitive techniques to study the different types of roughness at interfaces, and their evolution with thermal annealing. Cross-section HRTEM, on the other hand, allows a visual observation of the interfaces at an atomic scale. Plan-view TEM observation provides an accurate determination of the phases present in the multilayers over a large area of the samples. Because of the different range of spatial frequencies sampled by each technique, they provide complementary and powerful tools to study the microstructure - interfacial roughness interrelation in many thin film systems. Analysis of specular and diffuse scattering provides a comparative measure of the interfacial roughness. In some cases, the reflectivity of the multilayers is measured using a laser plasma-source soft x-ray reflectometer to study the performance of these multilayer mirrors.

The multilayer systems studied in this research were chosen because they have potential applications at wavelengths shorter than 12.5 nm. The W/C system was also one of the first multilayers that showed utility as an x-ray reflector at short wavelengths. Annealing of W/C multilayers results in interdiffusion between the layers, and formation of a carbide phase in the W-rich layers. The W-C phase diagram shows that the equiatomic tungsten carbide phase WC and C are immiscible, which also motivated the study of WC/C as potential multilayer devices. The W/C and WC/C systems also provide a comparison between the polycrystalline W and amorphous WC alloy

structures within the multilayers. Ru/C multilayers were studied because they have potential as normal incidence reflectance mirrors in the spectral region between 12.5 and 4.5 nm. The presence of the boron edge at λ=6.8 nm motivated the study of Ru/B_4C multilayers for normal incidence reflectance at this wavelength. The fabrication of Ru/B multilayers, which supposedly provide higher normal incidence reflectance near the boron edge, has been attempted. These multilayers, however, do not remain stable after deposition. In addition, Ru/B_4C and Ru/C multilayers provide a comparison of the effects of the microstructure and interfaces on the reflectivity, since both systems show promising performance at the boron wavelength, and they exhibit different reactions upon annealing. Ru and C are immiscible and thus phase separation is expected, which suggests that minimum interdiffusion should occur between the layers, while Ru and B in the Ru/B_4C system should react to form stable compounds. Ru/B4C and Ru/C provide a comparison of the microstructure-property relationships in reactive-component and conjugate-component multilayers. At shorter wavelengths, Cr/C and CrC/C multilayers are possible normal incidence mirrors at the C edge, 4.5 nm. Similar to the W/C and WC/C systems, Cr/C and CrC/C exhibit different microstructures. Comparisons between the W-based and the Cr-based systems also provide information on the microstructural trends in similar systems. Cu/C multilayers were studied because they have potential application as normal incidence reflectors at 4.5 nm wavelength, and also because their phase diagram does not show any compound carbide phase. Studies and comparison of the microstructure and their reactions upon annealing of these multilayer systems provide further understanding of the microstructural and interfacial evolution of multilayers for x-ray optical applications.

1.5 REVIEW OF LITERATURE

The published literature shows that a variety of multilayer structures with different combinations of materials had previously been fabricated and characterized. The higher-Z materials in these x-ray optical multilayers were usually elemental W, Mo, a transition metal, or a metallic alloy, while the low-Z materials were often Si or C. Many techniques have been applied to characterize these multilayer structures. X-ray scattering,[33,49-51] Extended X-ray Absorption Fine Structure (EXAFS),[52-53] and Raman spectroscopy[32-33,54] revealed information on the average interatomic structures within the layers and at their interfaces, while TEM[55-61] confirmed the quality of the layering and the localized nature of the phases within the layers.

Most of the metal/carbon systems that were formerly studied had applications or potential applications in x-ray optics. The most extensively studied system has been W/C, which was one of the first system used to demonstrate the utility of multilayer structures as x-ray diffracting elements. Significant contrast between atomic numbers and scattering powers of W and C provides efficient x-ray dispersing elements, and their high melting points ensure high stability in power intensive applications. However, even though it has been the most studied multilayer system, several discrepancies in their performance and understanding still exist. In general, the C-rich layers in the W/C multilayers, as well as in other metal/carbon systems, are amorphous. The structures of the W-rich layers have been observed to vary from amorphous to microcrystalline, or even polycrystalline, for both elemental W and tungsten carbide phases. The W-rich layers in the as-prepared multilayers have predominantly been amorphous within short periods and crystalline within longer periods.[49,60] It has also been observed that these layers remain amorphous for W-layer thickness up to 4 nm,[61] although microcrystalline WC has also been reported at above 1 nm W-layer thickness.[55] EXAFS studies reveal

that the W atoms in the W-rich layers are in a local environment of substantially rich carbon content, suggesting interdiffusion during deposition.[53] Evidence of intermixing of W and C in as-prepared amorphous W/C multilayers has also been reported.[49]

Annealing of the multilayers in the temperature range between 300 to 500°C leads to dramatic changes in the W-rich layer structures, while the layers still remain primarily intact. Crystallization of the amorphous phase or recrystallization of the bcc W combined with reaction with C to form W_2C upon annealing has generally been observed,[49-50,53,60] while observation of crystalline W in a 3.2 nm W-layer thickness W/C multilayer after annealing at 770°C has also been reported.[55] Formation of the crystalline carbide phases during annealing seems to depend upon the initial W layer thickness and the W to C layer thickness ratio.[50,52-53] Expansion of the multilayer periods after moderate annealing has also been reported for many metal/carbon systems, independent of crystallization of the initial W-rich layers. Lamble et al.,[52] however, reported a slight decrease in the period of the sample as a result of annealing.

The layers in the multilayers and their interfaces are more uniform and well defined at larger periods than at low periods. It has been proposed that the limit for the W layers to retain their continuity is approximately 1 nm,[62] which has been confirmed by the observation of discontinuity of the W layers in multilayers having a W-layer thickness of less than 1 nm.[61] High-Resolution TEM (HRTEM) studies[51] however, have demonstrated that the layered structures remain continuous and quite uniform in a 2 nm period W/C multilayer, or effectively 0.8 nm nominal thickness of the W-rich layers, after annealing at 500°C for 4 hours.

Intermixing between the constituents in the layers across their interfaces has been observed in many metal/carbon systems, as well as in the W/C system. Data fitting of

measured x-ray reflectance with calculated profiles indicated a mean interfacial roughness of 5 Å at each interface in the W/C system.[51] Ruterana et al.[61] suggested that amorphous layers have a lower interfacial roughness than crystalline layers which results in higher reflectivity. An observation of reduction of reflectivity by more than a factor of 10 after annealing at 400°C for 4 hours in Fe, Ni, Co/C multilayers was attributed to the roughening of the layer boundaries produced by microcrystallites that form during a transition from an amorphous to a polycrystalline state upon annealing.[63] Peak reflectivity in Ru/C multilayers with a mean roughness of 3.5 Å at the interfaces, however, remained unchanged after annealing.

1.6 ORGANIZATION OF THE THESIS

The organization of this thesis is as follows. Experimental techniques utilized in this study are described in chapter 2. Results of microstructural characterization of the multilayers subjected to various thermal treatments are presented in chapter 3. Discussion on the as-prepared microstructures, and their microstructural evolution upon annealing, which includes compound formation, amorphization, and phase separation, and of their morphological stability appears in chapter 4, which alludes to equilibrium phase diagrams and free energy-composition plots for detailed comparisons. In chapter 5, implications of the microstructural results on the performance and stability of x-ray multilayer mirrors are drawn. Chapter 6 summarizes the results and trends observed from the full study. In appendices A and B, respectively, the physics of multilayer mirrors and the effects of Fresnel fringes on interpretation of the TEM images on the multilayer interfaces are given. Optical properties at short wavelengths of materials, and discussion leading to the Fresnel equations which describe the reflection from a single surface and multilayers are included in appendix A. In appendix B, a discussion

on the possible use of Fresnel fringes in TEM images for characterization of the multilayer interfaces is given.

1.7 REFERENCES

1. J. H. Underwood and T. W. Barbee, Nature **294** (1981) 429.
2. M. Born and E. Wolf, *Principles of Optics*, 6th ed. (Pergamon Press, NY, 1980).
3. J.H. Underwood, Optics News **12** (1986) 3.
4. H. Koeppe, Dissertation, Giessen (1923).
5. W. Deubner, Ann. Phys. Leipzig **5** (1930) 261.
6. J. DuMond and J.P. Youtz, J. Appl. Phys. **11** (1940) 357.
7. J. Dinklage and R. Frerichs, J. Appl. Phys. **34** (1963) 2633.
8. E. Spiller, Appl. Phys. Lett. **20** (1972) 365.
9. E. Spiller, Appl. Optics **15** (1976) 2333.
10. T.W. Barbee, Jr. and D.C. Keith, in Workshop on Instrumentation for Synchrotron Radiation Research, H. Winick and G. Brown, eds., SSRL Report 78/04 (May 1987) III-36.
11. J.H. Underwood, T.W. Barbee, Jr., and C. Frieber, Appl. Opt. **25**, 1730 (1986).
12. A.C. Thompson, Y. Wu, J.H. Underwood, and T.W. Barbee, Jr., Nucl. Instrum. and Met. in Phys. Rev. **A255** (1987) 603.
13. N. M. Ceglio, D. G. Stearns, D. P. Gaines, A. M. Hawryluk, and J. E. Trebes, Optics Letters (1988).
14. G. F. Marshall, ed., *Applications of Thin-Film Multilayer Structures to Figured X-Ray Optics* (Proc. Soc. Photo-Opt. Instrum. Eng. **563**, 1985).
15. Soft X-Ray Projection Lithography (OSA Proc. **12**, 1991).
16. Soft X-Ray Projection Lithography (OSA Tech. Digest **8**, 1992).
17. Physics of X-Ray Multilayer Structures (OSA Tech. Digest **7**, 1992).
18. Soft X-Ray Projection Lithography (OSA Tech. Digest, 1993).
19. E.M. Gullikson, J.H. Underwood, P.C. Batson, and V. Nikitin, J. X-Ray Sci. Tech. **3** (1992) 283.
20. D.G. Stearns, R.S. Rosen, and S.P. Vernon, J. Vac. Sci. Technol. **A9**, 5 (1991) 2662.
21. D.G. Stearns, R.S. Rosen, and S.P. Vernon, submitted to Appl. Optics.
22. J.B. Kortright, D.G. Stearns, and D. Windt, OSA Tech. Digest **7** (1992).
23. J.B. Kortright, St. Joksch, and E. Ziegler, J. Appl. Phys. **69**, 1 (1991) 168.

24. A. Rosenbluth, Doctoral Dissertation, Institute of Optics, University of Rochester, NY (1982).
25. J.B. Kortright, private communication.
26. A.V. Vinogradov and B.Y. Zeldovich, Appl. Opt. **16** (1977) 89.
27. J. B. Kortright, J. Appl. Phys. **70** (1991) 3620.
28. D. E. Savage, J. Kleiner, N. Schimke, Y.-H. Phang, T. Jankowski, J. Jacobs, R. Kariotis, and M. G. Lagally, J. Appl. Phys. **69** (1991) 1411.
29. D. E. Savage, N. Schimke, Y.-H. Phang, and M. G. Lagally, J. Appl. Phys. **71**, 7 (1992) 3283.
30. D. G. Stearns, J. Appl. Phys. **65** (1989) 491.
31. D. G. Stearns, J. Appl. Phys. **71**, 9 (1992) 4286.
32. S.S. Chao, D.A. Pawlik, J. Gonzalez-hernandez, Q. Wang, and D.D. Allred, Solid State Comm. **79**, 3 (1991) 205.
33. J. Gonzalez-Hernandez, B.S. Chao, D.A. Pawlik, D.D. Allred, and Q. Wang, J. Vac. Sci. Technol. **A10**, 1 (1992) 145.
34. W.C. Shih and W.M. Stobbs, Ultramicros. **32** (1990) 219.
35. T.D. Nguyen, R. Gronsky, and J.B. Kortright, ICEM Proc. **4** (1990) 442.
36. T.D. Nguyen (unpublished).
37. T.W. Barbee, Jr, F. Spaepen, and A.L. Greer, eds., *Multilayers: Synthesis, Properties and Non-Electronic Applications* (MRS Proc. **103**, 1988).
38. L.L. Chang and B.C. Giessen, eds., *Synthetic Modulated Structures* (Academic Press, Inc., 1985).
39. Metallic Multilayers, First International Symposium (March, 1993, Kyoto, Japan), to be published in J. of Mag. and Mag. Mat.
40. A. Jankowski and T. Tsakalakos, J. Appl. Phys. **57**, 6 (1985) 1835
41. N. Nakayama, T. Okuyama, and T. Shinjo, J. Phys.: Condens. Matter. **5** (1993) 1173.
42. A.L. Greer and F. Spaepen, in *Synthetic Modulated Structures*, L.L. Chang and B.C. Giessen, eds. (Academic Press, Inc., 1985) 419.
43. R.S. Rosen, D.G. Stearns, M.A. Viliardos, M.E. Kassner, and S.P. Vernon, OSA Tech. Dig. **7** (1993) 157.
44. A.L. Greer, presented at the First International Symposium on Metallic Multilayers (March, 1993, Kyoto, Japan).
45. W.L. Johnson, Prog. Mater. Sci. **30** (1986) 81.
46. B.M. Clemens and M.J. Suchoski, Appl. Phys. Lett. **47** (1985) 943.
47. B.M. Clemens, Phys. Rev. **B33**, 11 (1986) 7615.
48. T.D. Nguyen, R. Gronsky, and J.B. Kortright, in *Thin Film Structures and Phase*

Stability (MRS Proc. **187**, 1990) 95.
49. J.B. Kortright and J.D. Denlinger, in *Multilayers: Synthesis, Properties and Non-Electronic Applications* (MRS Proc. **103**, 1988) 95.
50. Y. Takagi, S.A. Flessa, K.L. Hart, D.A. Pawlik, A.M. Kaden, J.L. Wood, J.E. Keem, J.E. Tyler, in *Applications of Thin-Film Multilayered Structures to Figured X-Ray Optics* (Proc. SPIE **563**, 1985) 66.
51. B.A. Vidal and J.C. Marfaing, J. Appl. Phys. **65** (1989) 3453.
52. G.M. Lamble, S.M. Heald, D.E. Sayers, and E. Zeigler, in *Multilayers: Synthesis, Properties and Non-Electronic Applications* (Proc. MRS **103**, 1988).
53. G.M. Lamble, S.M. Heald, D.E. Sayers, E. Ziegler, and P.J. Viccaro, J. Appl. Phys. **65** (1989) 4250.
54. D.D. Allred, Q. Wang, and J. Gonzalez-Hernandez (MRS Proc. **106**, 1990) 605.
55. E. Ziegler, Y. Lepetre, I.K. Schuller, and E. Spiller, Apl. Phys. Let. **48** (1986) 1354.
56. Y. Lepetre, E. Ziegler, I.K. Schuller, and R. Rivoira, J. Appl. Phys. **64** (1986) 2301.
57. A.K. Petford-Long, M.b. Stearns, C.-H. Chang, S.R. Nutt, D.G. Stearns, N.M. Ceglio, and A.M. Hawryluk, J. Appl. Phys. **61** (1987) 1422.
58. S.R. Nutt and J.E. Keem, in *Multilayers: Synthesis, Properties and Non-Electronic Applications* (MRS Proc. **103**, 1988) 87.
59. K. Holloway, K.B. Do, and R. Sinclair, in *Multilayers: Synthesis, Properties and Non-Electronic Applications* (MRS Proc. **103**, 1988) 167.
60. T.D. Nguyen, R. Gronsky, and J.B. Kortright, in *High-Resolution Microscopy of Materials* (MRS Proc. **139**, 1989) 357.
61. R. Ruterana, J.-P. Chevalier, and P. Houdy, J. Appl. Phys. **65** (1989) 3907.
62. Y. Lepetre, I.K. Schuller, G. Rasigni, R. Rivoira, R. Philip, and P. Dhez, Opt. Eng. **25** (1986) 849.
63. L. Golub, E. Spiller, R.J. Bartlett, M.P. Hockaday, D.R. Kania, W.J. Trela, and R. Tatchyn, Appl. Opt. **23** (1984) 3529.

1.8 FIGURES

Figure 1-1. Schematic diagram of a periodic multilayer structure. High reflectance is obtained from constructive interference of reflected rays from the interfaces according to Bragg's law.

Figure 1-2. Status of normal incidence reflectance measured at the Center for X-Ray Optics, Lawrence Berkeley Laboratory. The calculated and measured reflectance of Ru/C multilayers show the deviation of the measured from the calculated as the wavelength decreases. Figure courtesy of J. B. Kortright.

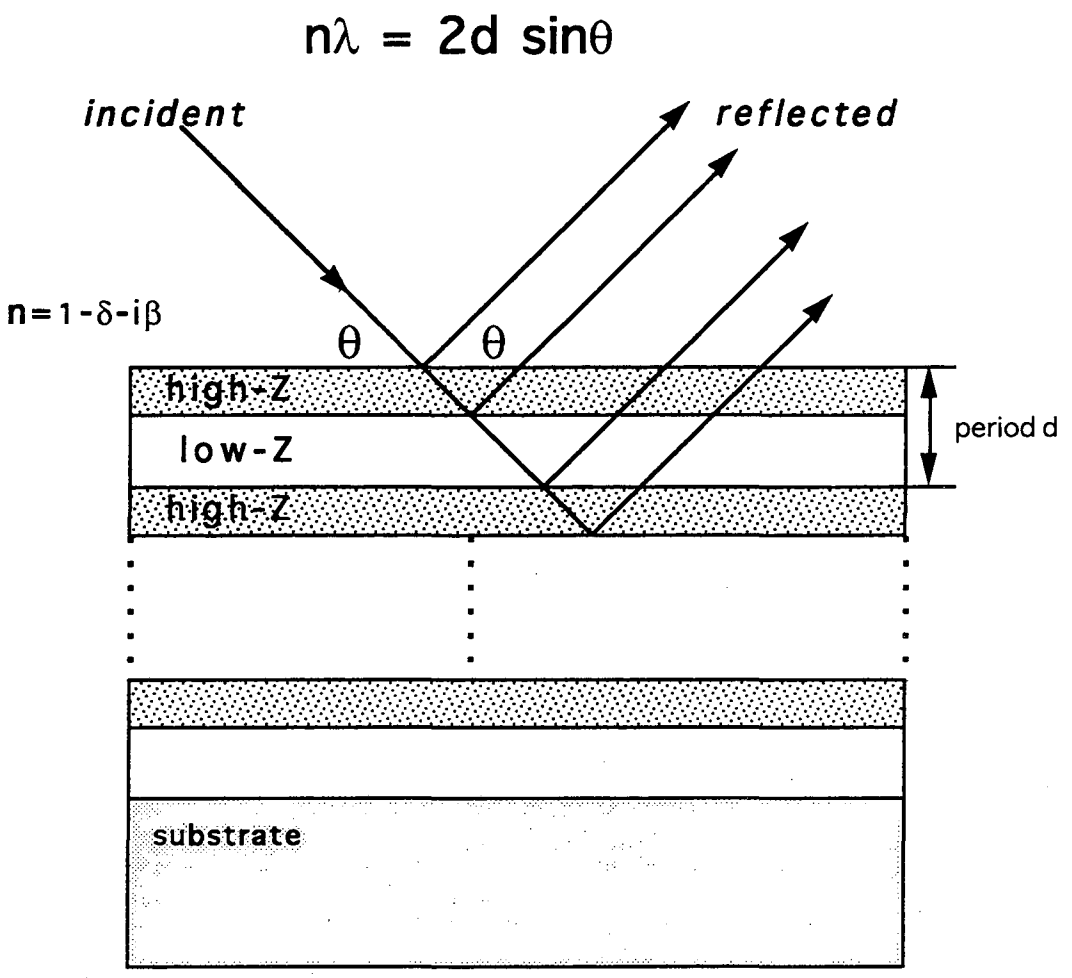
nλ = 2d sinθ
incident
reflected
n=1-δ-iβ
θ
θ
high-Z
low-Z
high-Z
period d
substrate

Figure 1-1

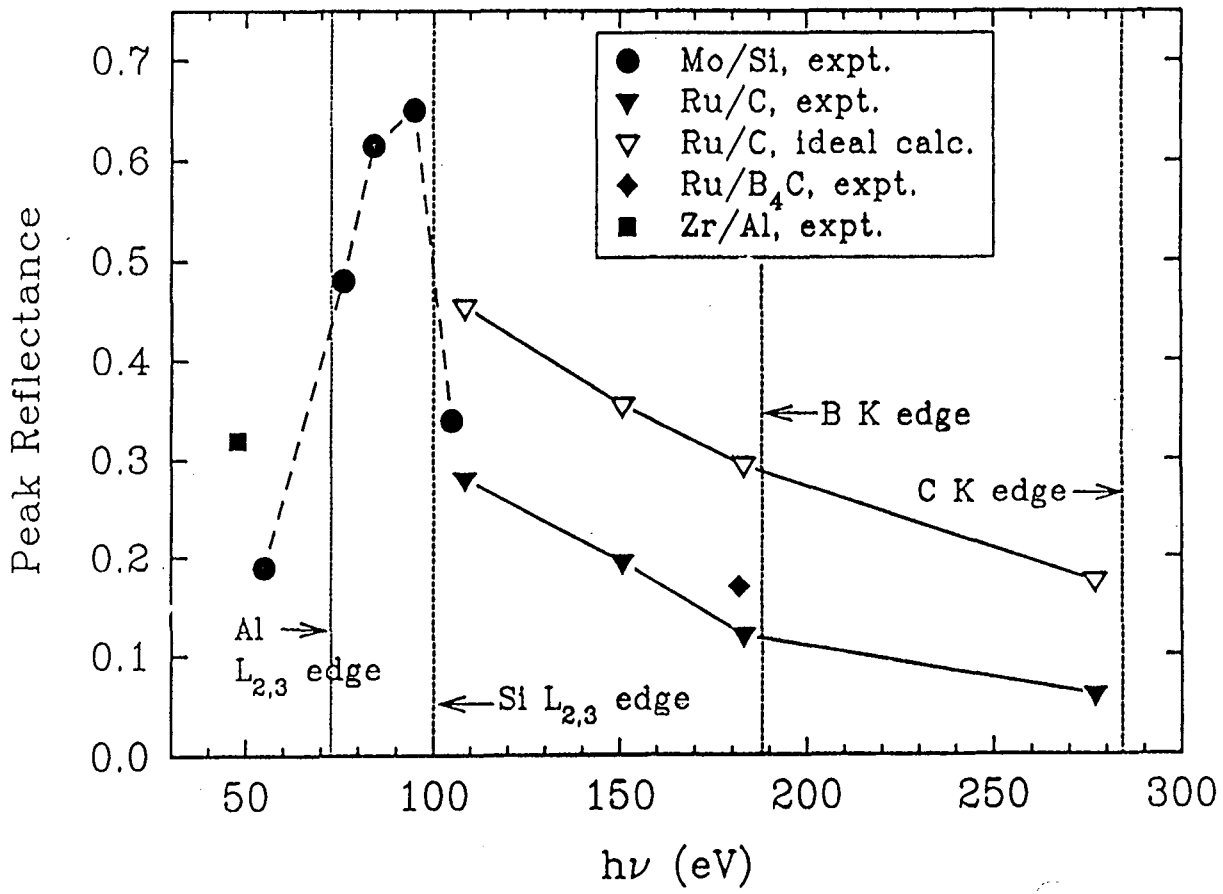
Mo/Si, expt.
Ru/C, expt.
Ru/C, ideal calc.
Ru/B4C, expt.
Zr/Al, expt.
Peak Reflectance
0.0
0.1
0.2
0.3
0.4
0.5
0.6
0.7
50
100
150
200
250
300
hν (eV)
Al L2,3 edge
Si L2,3 edge
B K edge
C K edge

Figure 1-2

CHAPTER 2

EXPERIMENTAL TECHNIQUES

2.1 FABRICATION OF MULTILAYERS

Multilayers were prepared by DC magnetron sputtering at the Center for X-ray Optics, Lawrence Berkeley Laboratory. A schematic diagram of the sputtering chamber is shown in Figure 2-1. The positions of the sources are fixed while the substrates are moving during deposition. The sources and their targets are mounted in the same radius as the circular path of the substrates. During deposition, the substrates rotate in turn over two elemental targets. One multilayer period is deposited during one single revolution of the substrates. The substrate table is about 100 mm above the targets, and the argon sputter gas pressure is 0.002 torr. The sputtering rates of different materials targets are controlled by the current of the power supplies. The period of the multilayers is controlled by the rotational velocity of the substrates over the targets. The substrates are not cooled by any mechanisms and thus the temperature of the substrates is allowed to float during deposition. The temperature however is typically below 150°C after a deposition run of more than 3 hours.

Multilayers of different nominal period were prepared for this study. Different thicknesses of the multilayer periods of the samples were controlled by keeping the target sputtering rates fixed and varying only the rotation velocity of the substrates. The nominal relative thicknesses of the metal-rich and the carbon-rich layers based on the sputtering rates of the individual targets, were the same for all the samples, such that the

metal-rich layer would make up 40%, and the carbon-rich layer makes up 60% of the period. This layer thickness percentile has been calculated to yield optimum reflection and is typical of that in multilayers used in x-ray optical applications.[1]

Multilayers were prepared on two types of substrates: 3-inch semiconductor-grade (111) Si wafers provide samples for cross-sectional TEM observation, and TEM copper grids provide samples for plan-view TEM characterization. In addition, some multilayers were also prepared on superpolished optical flat substrates for reflectivity measurements and x-ray diffraction studies. For each run, the substrates were first coated with an amorphous carbon buffer layer of approximately 10 nm thick. The multilayers were then deposited to yield total multilayer thicknesses ranging from 150 to 350 nm. Each deposition run spans about 2.5 hours.

2.2 Normal Incidence Reflectance Measurement

Measurements of the normal incidence reflectance at soft x-ray wavelengths are performed using a laser-produced plasma x-ray source. The apparatus was designed by the researchers at the Center for X-Ray Optics, Lawrence Berkeley Laboratory. A detailed description and characterization of the reflectometer has been described elsewhere.[2] The source is produced by focusing 0.532 mm light form a Q-switched Nd:YAG laser on a solid target. The produced x-ray is continuously tunable over the range between 4 and 40 nm. The wavelength used is defined using a high throughput spherical monochromator. After the monochromator, the beam passes through a small I_0 box, which measures the reference intensity, and into the measurement chamber. Inside the chamber, the sample is mounted at the center. The detector, which sits on an arm that rests on the same rotational axis as the sample, is about 25 cm from the axis of

rotation. The minimum angle between the incoming and reflected beams is 5°. During measurements, the chamber is kept under a vacuum of 10^{-7} torr by a cryopump.

To measure the absolute reflectance, the sample is first measured over the range of wavelengths near the Bragg condition. The sample is then translated out of the beam path, and the direct beam is then measured over the same range of wavelengths. The absolute reflectance of the multilayers is the ratio of the intensity reflected from the sample to the intensity of the direct beam. The role of the reference intensity I_o is to eliminate any fluctuation in the intensities between the measurements of the sample and the direct beam.

2.3 ANNEALING

One sample from each of the multilayers prepared was annealed in a tube furnace in a vacuum of 10^{-6} torr. The vacuum system contains a mechanical roughing pump, and a turbomolecular pump that can provide a vacuum of 10^{-7} torr in the vacuum tube at room temperature. The samples were heated by an electric coil furnace, which was calibrated by a thermocouple meter. The temperatures were arbitrary chosen at 500 or 600°C. The annealing condition was at 500°C for 4 hours, or at 600°C for 30 minutes or one hour, depending on the experiment. The error in the annealing temperature was ±10°C. Samples annealed under the same condition were compared with each other, although the melting and eutectic temperatures of the materials in the samples are different from each other. These annealing temperatures are approximately near or less than one third of the respective eutectic temperatures of the materials systems. The samples were subsequently cooled under vacuum, and usually reached room temperature in about 4 hours.

2.4 X-RAY SCATTERING

X-ray measurements were used to determine the periodicity of the multilayers and the absolute reflectance profile. The low-angle region spanning the total reflection regime and the first few multilayer Bragg peaks were measured in a two crystal, Bragg geometry diffractometer utilizing Cu $K_{\alpha 1}$ radiation with the multilayers in the position of the second crystal. During reflectance measurements, both the detector and the sample move in steps by motors, such that the detector moves twice as fast as the sample, to establish the θ - 2θ relationship. Absolute reflectance profiles were measured in step of 0.010° at 30 seconds per step. Bragg peaks from the multilayers were used to determine the period of the multilayers, using Bragg's law $n \cdot \lambda = 2 \cdot d \cdot \sin\theta$. A high number of Bragg peaks was measured to increase the accuracy of period determination.[3]

X-ray scattering measurements were performed at Stanford Synchrotron Radiation Laboratory (SSRL) using 1.38Å wavelength. Symmetric (θ-2θ) and asymmetric (fixed θ) high-angle scattering was used to determine the microstructures in the multilayers. The asymmetric geometry has the advantage that a larger volume of the sample is examined than in the symmetric geometry. The combined scans give information regarding the preferred orientation of the poly-crystalline films perpendicular to the surface. Specular and non-specular x-ray scattering of multilayers has been described in many papers.[4-7] In this study, two low angle measurements were made to study the quality of the multilayers and the roughness: specular and off-set, diffuse scans. The specular measurement uses the standard symmetric θ-2θ Bragg geometry. The offset measurement similarly scans two angles synchronously, but with a small θ offset from the specular condition ($\theta+\Delta\theta$, 2θ). Offset scans measure diffuse intensity in direction nearly parallel to the specular direction in reciprocal space.

2.5 TRANSMISSION ELECTRON MICROSCOPY

2.5.1 Cross-sectional TEM Specimen Preparation

As-prepared and annealed multilayer samples on Si substrates were prepared for cross-sectional TEM observation by the conventional mechanical thinning and ion beam milling technique.[8-9] The specimen preparation procedure follows from Figure 2-2a. First, two slabs of the silicon substrate sample, 10 mm long by 3 mm wide, were cut, with the longer side of the slabs parallel to the flat edge of the Si wafer, using a diamond-scribe. The orientation of the cut was chosen to yield the <110> direction parallel to the electron beam when viewed in the microscope. This direction provides a projection of the Si lattice that can be resolved in the electron microscope. Next, the two slabs were glued together using Devcon 2-ton epoxy, with the deposited films facing each other, as shown in Figure 2-2b.

The glued sample was then mechanically thinned using sandpaper on a rotating grinding wheel, and polished using alumina powder on polishing cloths. To start, the sandwiched sample was mounted on a 1 inch-diameter 5/8 inch-thick piece of Pyrex glass, using Crystal Bond 509 wax by Aremco Products, Inc. The sample was carefully mounted on top of the glass, ensuring that the film surfaces were perpendicular to the surface of the glass, so that the sample was mechanically thinned perpendicular to the <110> direction (Figure 2-2c).

On one side, the sample was not thinned, but only ground and polished to a flat surface parallel to the glass surface. The sample was pre-polished by moving back and forth on 2400-grit paper (5 μm), with a little distilled water to keep it cool. The sample was then polished using 1 μm alumina, and followed by 0.05 μm alumina, on a polishing

cloth and rotating wheel (Figure 2-2d). After polishing the first side, the sample was turned over, so that the polished side was facing toward the glass piece. Following the same steps as before, the unpolished side was thinned and polished, using 600-grit paper, 2400-grit paper, 1 μm alumina, and 0.05 μm alumina. The sample was now thinned to about 20 μm before being polished. In general, the specimen was usually thinned until the edges start to regress. This was a sign that the specimen is ready for ion polishing.

The 20 μm-thick sample is next mounted on a TEM grid to be ion milled. The 0.5 mm-width oval-slot TEM grids were glued on top of the thinned sample using the Devcon epoxy, such that the film surfaces or interfaces were parallel to the longer side of the slot, and the sample covered the entire slot, as shown in Figure 2-2e. After curing, the specimens were removed from the glass piece and ready for ion-milling. The sample was ion-milled in a cold stage, with argon ion guns bombarding on both sides of the specimen, schematically shown in Figure 2-2f. The argon ions were accelerated with a voltage of 5 kV, drawing a specimen current of 0.5 milliamps, at a specimen tilt angle of 13°, under 10^{-4} torr pressure during milling. The ions created a hole along the epoxy about 1 mm long, as illustrated in Figure 2-2g. The result of such a multilayer is shown in Figure 2-2h.

2.5.2 Plan-view Sample Preparation

Multilayers were prepared for TEM plan-view observation to complement the cross-sectional studies. Figure 2-3 shows the steps in preparing plan-view samples for TEM observation.[10] The substrates on which the multilayers were grown consisted of 3 mm-diameter 300-mesh copper microscope grids, mounted on a glass slide with Crystalbond vacuum adhesive, as shown in Figure 2-3a. Multilayers were then

deposited on the grids and the glass slide (Figure 2-3b). After a deposition of a few bilayers of the multilayers, to make up total multilayer thickness of about 30 nm, the glass slide holding the samples was soaked in acetone to dissolve the Crystalbond (Figure 2-3c), leaving the multilayer spanning the holes of the copper grids, as shown in Figure 2-3d.

2.5.3 Transmission Electron Microscopy

High resolution Transmission Electron Microscopy (TEM) was performed in a double-tilt top-entry high-resolution JOEL JEM 200CX microscope, equipped with high resolution goniometer, at the National Center for Electron Microscopy. The operating voltage was 200 kV which yields a nominal point-to-point resolution of better than 2.4 Å. The specimens were aligned so that the electron beam was parallel to the <110> direction of the Si substrate, so that the {111} planes (d_{111} = 0.3135 nm) were resolved in high-resolution electron microscopy and used for image calibration. Image observation and acquisition under the electron beam was carried out quickly, and carefully, to ensure that minimum exposure to the beam was achieved, and little or no radiation damage occurred. When a thin region was identified, the sample was tilted to a [110] Si pole while the beam was on the silicon substrate, not the multilayers. The beam was then defocused, and moved to the multilayer region. The multilayer was then focused and adjusted for astigmatism at as low a defocused beam as possible, to reduce radiation exposure from the electron beam. A through-focus-series of images was then recorded.

Plan-view samples were studied in a Philips 301 operating at 100 kV. The area of observation in the plan-view samples was much larger than that of the cross-sectional samples, hence providing more conclusive information than the cross-sectional samples about larger-scale microstructural features.

2.5.4 Image Interpretation

Image interpretation in electron microscopy is an important step in providing information about the samples. Artifacts induced during the specimen preparation process, or under the electron beam during TEM observation, can lead to erroneous interpretation of the images. Examination of the specimen over a wide area was performed to ensure the accuracy of the results. The thicknesses of the layers can not always be determined precisely due to possible projection errors in a transmission image, or due to the presence of interfacial layers between the layers. Interpretation of the microstructures inside the layers and at their interfaces is also complicated by the great difference in contrast between the metal-rich and the carbon-rich layers imaged in the micrographs, and by the differences in images taken at different defocus values arising from Fresnel fringe effects at interfaces between two high contrast layers.[11-12] Observation of Fresnel fringes in through-focus-series of TEM images, simulation of the fringes to study their characteristics are presented, and their implication to quantification of interfacial structure is discussed in Appendix B. In this study, the images of different samples were taken at approximately the same defocus value for uniformity, and attention was paid to all sources of artifacts during interpretation of results.

2.6 REFERENCES

1. A.V. Vinogradov and B.Y. Zeldovich, Appl. Opt. **16** (1977) 89.
2. E.M. Gullikson, J.H. Underwood, P.C. Batson, and V. Nikitin, J. X-Ray Sci. Tech. **3** (1992) 283.
3. A.E. Rosenbluth and J.M. Forsyth, AIP Conf. Proc. **75** (1981) 280.
4. J.B. Kortright, J. Appl. Phys. **70**, 7 (1991) 3620.

5. D.E. Savage, J. Kleiner, N. Schimke, Y.H. Phang, T. Janskowski, J. Jacobs, R. Kariotis, and M.G. Lagally, J. Appl. Phys. **69** (1991) 1411.
6. D.G. Stearns, J. Appl. Phys. **71** (1992) 4286.
7. Y.H. Phang, R. Kariotis, D.E. Savage, and M.G. Lagally, J. Appl. Phys. **72**, 10 (1992) 4627.
8. T.D. Nguyen, R. Gronsky, and J.B. Kortright, J. Elec. Microsc. Tech. **19** (1991) 473.
9. J.C. Bravman, and R. Sinclair, J. Electron. Microsc. Tech. **1** (1984) 53.
10. T.D. Nguyen, R. Gronsky, and J.B. Kortright, EMSA Proc. (1989) 680.
11. C.S. Baxter and W.M. Stobbs, Appl. Phys. Lett. **48** (1986) 1202.
12. T.D. Nguyen, R. Gronsky, and J.B. Kortright, ICEM Proc. **4** (1990) 442.

2.7 FIGURES

Figure 2-1. A schematic diagram of the sputtering chamber.

Figure 2-2. Cross-sectional TEM specimen preparation steps: a) cutting, b) gluing the samples together, c) grinding, d) polishing, e) intalling the TEM grids, f) ion milling, g) the final TEM sample, and h) TEM image of a multilayer in cross-section.

Figure 2-3. Plan-view TEM specimen preparation steps: a) TEM grids are mounted onto a glass slide by a layer of wax, b) the assembly are placed in the sputtering chamber, c) the samples are soaked in acetone to dissolve the wax, and d) the final TEM sample.

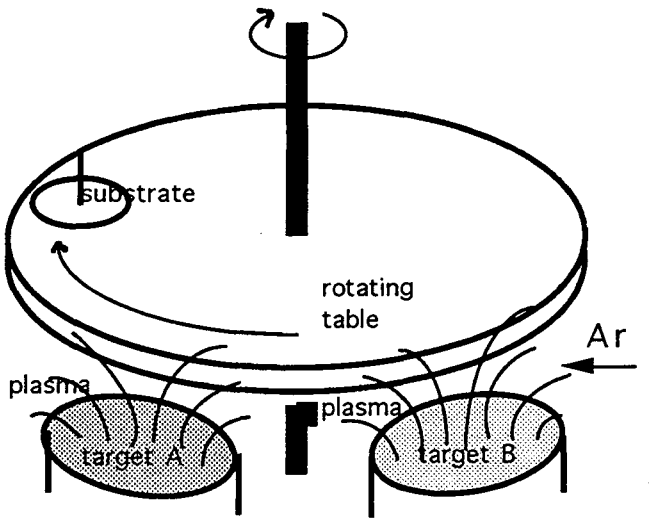
substrate
rotating
table
Ar
plasma
plasma
target A
target B

Figure 2-1

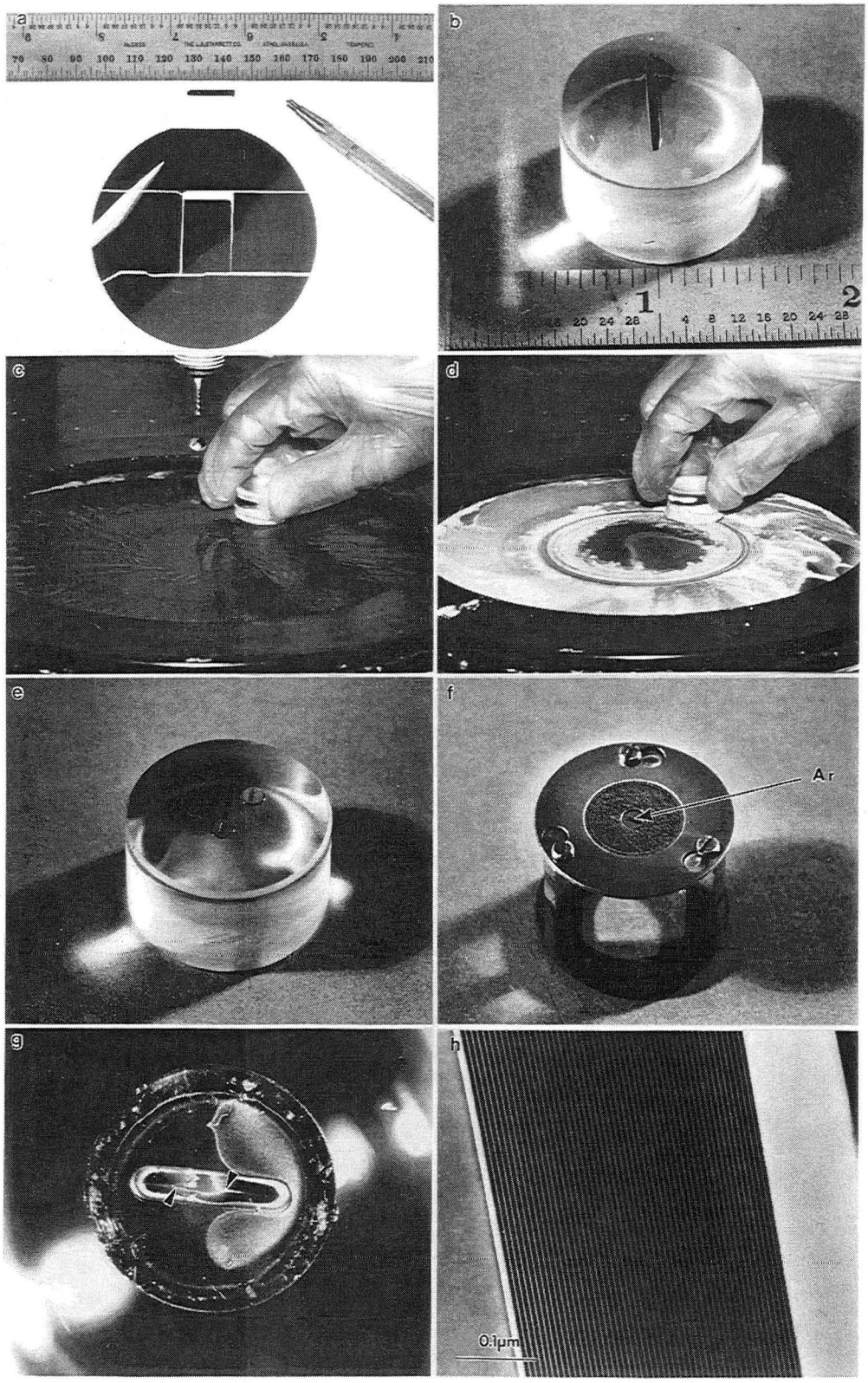

Figure 2-2

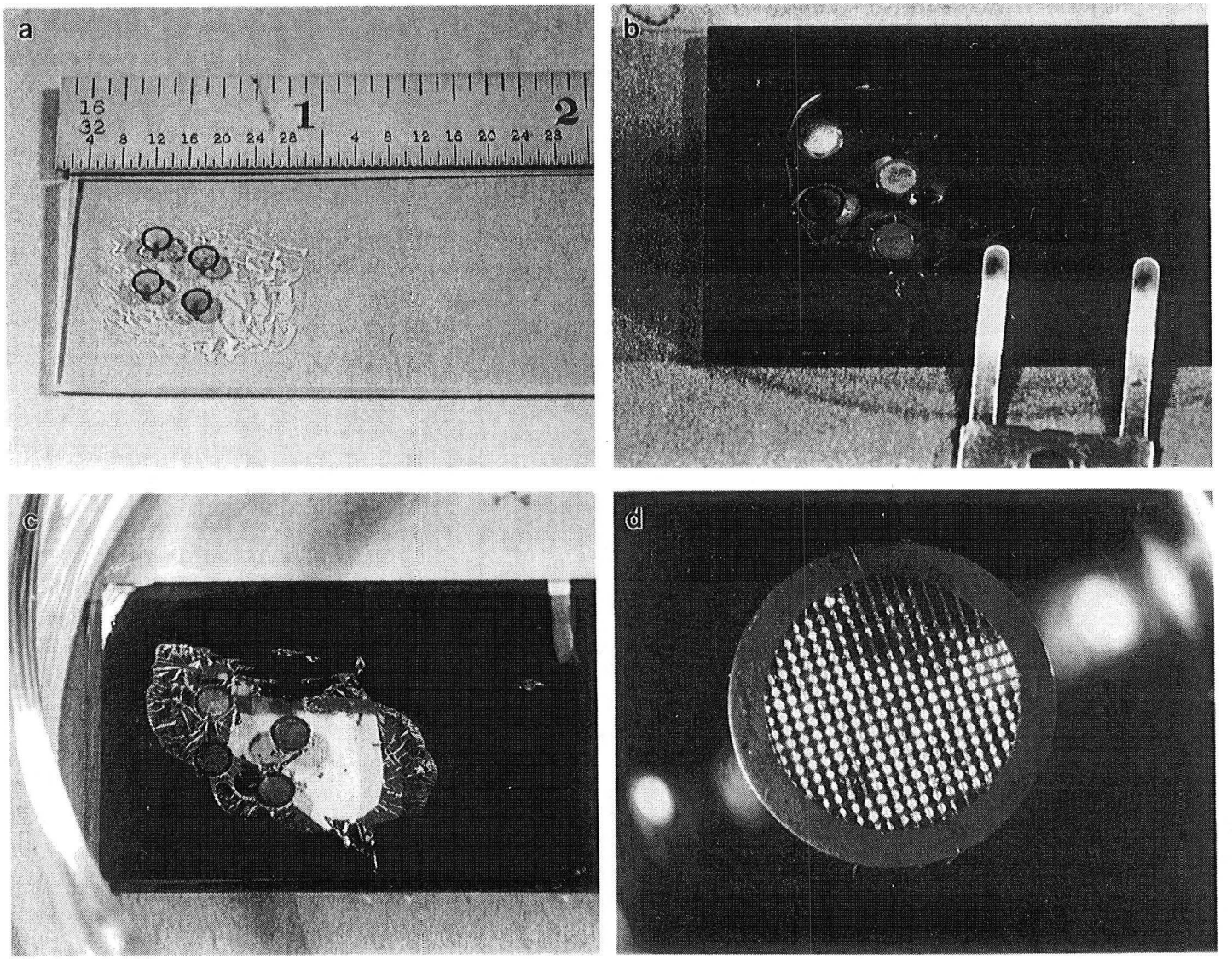

Figure 2-3

CHAPTER 3

TEM MICROSTRUCTURAL RESULTS

3.1 W/C SYSTEM

Characteristics of the phases in the W-rich layers in the as-prepared and annealed W/C multilayers are summarized in Table 3-1. Short period as-prepared W/C multilayers have an amorphous structure, while longer period structures contain elemental W microcrystallites in the W-rich layers. Figure 3-1 shows the plan-view TEM bright field images and their corresponding diffraction patterns for as-prepared and annealed 2 nm-period W/C samples. Examination of the multilayers in cross-section also indicates that both the metal and the C layers are amorphous. The exact nature of the metal amorphous structure in the short period multilayers could not be conclusively determined by TEM alone. It could be amorphous W, or a W_xC_{1-x} mixture that resulted from interdiffusion of the C into the W-rich layers. Upon annealing, the W-rich layers in the 2 nm-period sample remain amorphous, as indicated by the plan-view image shown in Figure 3-1b. Studies of the 4 nm period multilayers also indicate that both as-prepared and annealed samples have an amorphous structure.

Longer period W/C multilayers show the presence of a crystalline phase in the as-prepared samples, and phase transformation upon annealing. Examination of the high resolution TEM bright field image and its diffraction pattern of the 7 nm-period sample reveals signs of micro-crystallinity in the W-rich layers, along with the presence of an amorphous phase. The 12 nm-period sample contains the crystalline W phase.

Figure 3-2 shows the TEM images and their corresponding diffraction patterns of as-prepared and annealed 12 nm-period W/C multilayers. The bright field image of the as-prepared sample (Figure 3-2a) shows the polycrystalline grains in the layers, and the sharp rings in the electron diffraction pattern indicate the dominant presence of the elemental BCC tungsten phase in the W-rich layers. Upon annealing, reaction between the C and the W layers produces a carbide phase. Comparison of the bright field images in Figure 3-2 indicates that the crystalline grains in the annealed sample are larger than those in the as-prepared sample. The diffraction ring patterns of the annealed 12 nm period shown in the Figure 3-2b were consistent with the identification of W_2C. These rings are continuous and have equal intensity around the circumference which suggests that there is no preferred orientation of the crystallites in the plane of the layers. The W crystallites in the as-prepared sample hence have recrystallized and grown into the carbide phase. The smallest rings present in the annealed 12 nm diffraction patterns, showing large spacing of approximately 3.81Å, could not be identified with a carbide phase, but may result from crystalline oxide or metastable carbide phases.

3.2 WC/C SYSTEM

Figure 3-3 shows the high-resolution cross-sectional TEM images of as-prepared and annealed 2 nm period WC/C multilayers. The layers are quite uniform and continuous. The microstructure remains layered after annealing, and shows amorphous characteristics, similar to the W/C multilayers of the same period. For longer periods, in contrast to the finding of the crystalline phases in the metal-rich layers, the microstructure in the WC/C multilayers appears amorphous for both as-prepared and annealed samples. A cross-sectional view of the as-prepared and annealed 12 nm-period WC/C multilayers showing the smooth interfaces and amorphous microstructure

is shown in Figure 3-4. The amorphous structure is further confirmed by observation of diffuse rings in the electron diffraction patterns taken over larger areas in the plan-view orientation. Figure 3-5 shows the plan-view TEM images and diffraction patterns of the 12 nm-period samples. Both images in Figure 3-5 show that the microstructure is predominantly amorphous. The faint polycrystalline rings in Figure 3-5b suggest that there may be some micro-carbide crystallites in the annealed 12 nm-period samples. High resolution examination of the corresponding sample in cross-section however does not show any lattice fringes of a crystalline phase.

3.3 Cr/C SYSTEM

The evolution of the microstructure of as-prepared Cr/C multilayers with multilayer period is similar to that of the W/C system. The microstructure of the Cr-rich layers in short-period multilayers is amorphous, while that in the longer-period shows the presence of a crystalline structure. Figure 3-6 shows a cross-sectional high resolution TEM image of an as-prepared 5 nm-period Cr/C multilayer. The layers and interfaces between the layers seem to be quite flat and smooth. Both the Cr and C layers have amorphous structures at this period. The microstructural characteristics of Figure 3-7 shows the plan-view electron diffraction patterns of as-prepared and annealed 5 nm and 10 nm-period Cr/C multilayers. The diffuse rings in the diffraction patterns in Figure 3-7a confirm the amorphous structure of the 5 nm-period as-prepared multilayers. The diffraction pattern of the annealed sample, shown in Figure 3-7b also shows the diffuse rings. The microstructure of the 5 nm period multilayer thus is amorphous, and remains amorphous after annealing. Longer period as-prepared multilayers have a polycrystalline microstructure. The diffraction pattern of the as-prepared 10 nm period multilayer (Figure 3-7c) contains sharp rings, which are

identified as the [110], [200], and [211] of the BCC Cr phase. Bright field TEM images of this sample indicate that the Cr grains are roughly a few nanometers in diameter, comparable to the thickness of the Cr layers. Upon annealing at 600°C for 30 minutes, the structure amorphizes, as indicated by the disappearance of the crystalline rings in the diffraction patterns. Figure 3-7d shows the diffuse rings of an amorphous structure in the annealed 10 nm period sample.

Cross sections confirm the occurrence of a phase transformation in the 10 nm period Cr/C multilayer. Figure 3-8 shows a cross-sectional high resolution TEM image of the annealed sample at low magnification. Shown in this figure are the Si substrate and many bilayer periods of the Cr/C layered structure. At this magnification, the layers seem well defined and uniform. The presence of interfacial layers indicates intermixing and diffusion between the layers. The corresponding electron diffraction pattern exhibits large spacing diffraction spots from the Si substrate, fine spacing spots (not resolved) arising from the periodicity of the multilayer, and diffuse rings from the amorphous region of the multilayer microstructure.

Examination of the sample at high magnification shows interdiffusion between the layers more readily. Figure 3-9 shows a high magnification high resolution TEM image of the same sample. As can be seen from the figure, the layers are well defined, though the interfaces are not quite flat. The microstructures in both the Cr and C layers are amorphous. No signs of crystallinity or lattice fringes are observed in the bright field image. The selected area diffraction (SAD) pattern, also shown in the figure, shows the diffuse rings of an amorphous structure. The diffraction spots of the Si substrate are not present in this pattern because the SAD aperture only includes the multilayer and not the substrate. The bright field image indicates that significant intermixing between the Cr and C layers has occurred during annealing. The result suggests that interdiffusion at

the interfaces, or diffusion of the C into the Cr layers to create the amorphous interfacial layers, amorphizes the initially crystalline Cr layers.

3.4 CrC/C SYSTEM

Similar to the W/C and WC/C systems, CrC/C multilayers were studied because of possible mixing of Cr and C in the multilayers after annealing, as predicted by the equilibrium phase diagram. Both plan-view and cross-sectional TEM and electron diffraction indicate that CrC/C multilayers are amorphous for all periods. Upon annealing, all the multilayers remain amorphous, similar to the results found in the WC/C system. The microstructures and phases of as-prepared and annealed Cr/C, and CrC/C multilayers are summarized in Table 3-2.

3.5 Ru/C SYSTEM

Agglomeration of the Ru layers, and nucleation and grain growth of the elemental Ru phase are observed in Ru/C multilayers after annealing. Agglomeration and crystallization of the Ru layers, which occur in short period multilayers, in particular are interesting and different from the results of other multilayers of comparable period. Agglomeration depends on the thickness of the Ru layers, while crystallization and grain growth of Ru crystallites depend on the thickness of both the Ru and the C layers, which results in different grain size and morphology. To obtain an understanding of the microstructural evolution of the Ru layers upon annealing, different experimental studies were designed. In the following subsections, the results from three experiments are presented. First, the microstructural and morphological evolution of various period

samples upon annealing is examined by cross-sectional high resolution TEM. *In-situ* TEM results of a 2 nm period multilayer, which provides a dynamical observation of agglomeration and crystallization of the Ru layers, then follows. The dynamical experiments were performed in an attempt to determine the order of occurrence between agglomeration of the Ru layers and crystallization of the Ru crystallites. Since the Ru layers are approximately 0.8 nm thick in this sample, they may agglomerate to a critical nucleation radius or thickness before crystallization occurs. On the other hand, the amorphous Ru layers may crystallize before agglomeration occur. Grain size distribution in multilayers of different Ru and C layer thicknesses in annealed samples, studied by plan-view TEM, is presented in the last subsection.

3.5.1 Microstructural Evolution

A summary of the structural characteristics of the Ru/C multilayers is presented in Table 3-3. The microstructural evolution of the Ru layers in as-prepared Ru/C multilayers is similar to that of the W layers in W/C multilayers. The microstructure is amorphous at short period and shows the elemental phase of the metals at longer periods. The Ru layers however seem to crystallize at a shorter period than the W layers. High resolution TEM bright-field images of a 4.3 nm-period Ru/C multilayer show lattice fringes of the Ru crystallites in the Ru layers (Figure 3-10). Signs of crystallinity are also evident in a 3.5 nm-period sample. The nominal thickness of the Ru layers in this sample is 1.4 nm, which is only a few atomic layers thick. In contrast to the Ru/C system, W/C multilayers show a predominantly amorphous structure at 4 nm period, or nominally 1.6 nm W layer thickness.

Nucleation and grain growth are observed in short period Ru/C multilayers after annealing. Figure 3-11 shows the cross-sectional TEM images of the as-prepared and

annealed 2 nm period Ru/C multilayers. Figure 3-11a shows that the as-prepared layered microstructure is amorphous, which is evidenced by the lack of any indication of crystallinity in the corresponding diffraction pattern. Upon annealing, the Ru has agglomerated to form almost-spherical crystallites of about 4 nm in diameter, as shown in Figure 3-11b. The layered structures are destroyed, in contrast to the behavior of multilayers of other systems at comparable period. From its diffraction pattern, the crystalline phase was identified as elemental hexagonal Ru.

Longer period as-prepared and annealed Ru/C multilayers contain the elemental phase of the metal, as confirmed by both cross-section and plan-view TEM observation. Figure 3-12 shows the cross-sectional high resolution TEM images of as-prepared and annealed 10 nm-period Ru/C multilayers. Both images show polycrystalline structure within the Ru-rich layers. Examination of larger areas of the sample reveals that the grain size of the crystallites in the film plane of the as-prepared multilayers shown in Figure 3-12a is approximately ten times smaller than those in the annealed sample. The arrows in Figure 3-12a show a smooth grain boundary between two Ru grains in the layer. The two sets of arrows in Figure 3-12b indicate one Ru grain which has a [101] direction perpendicular to the layer plane, as observed in the texture in the cross-sectional electron diffraction patterns. A Ru grain boundary at the Ru/C interface is shown at arrows B in Figure 3-12b. At such a boundary, mismatch between crystal planes of the grains causes roughening of the boundaries, which extends into the interfaces of the layers. Upon annealing, these crystallites grow to sizes that are tens of nanometers in the lateral direction, the same order as the Ru-rich layer thickness in the multilayer. The electron diffraction patterns of the plan-view samples indicate no signs of preferred orientation in the plane of the layers, while diffraction patterns of the elemental Ru in the cross-sectional samples show a strong [101] texture perpendicular to the layer interfaces. Bright field images of the as-prepared 5 nm period show a

crystalline phase in the Ru-rich layers, although exact structures could not be identified. Its electron diffraction pattern shows diffuse rings having six-fold symmetry, which may indicate that the layers contain very small crystallites of hexagonal structures. The 2 nm period multilayer agglomerates under this annealing condition, while longer period 3.5, 5, and 10 nm samples remain layered.

Samples of 1nm Ru / 1nm C treated under various annealing conditions were examined in cross-section to study the evolution of the microstructure and morphology, and of agglomeration in the short period multilayers. Figure 3-13 illustrates the evolution of microstructure of this multilayer with different thermal treatments. Shown in each frame of Figure 13 a-d are the cross-sectional HRTEM images of ten bilayers of Ru and C films deposited on a thick C buffer layer over a Si substrate (not shown), and its corresponding electron diffraction pattern. The amorphous layer on top of the multilayers is the epoxy adhesive used in the cross-sectional TEM specimen preparation process. The small-lattice-spacing diffraction spots in the diffraction patterns of Figures 3-13 a-c arise from the epitaxial Si substrate.

The layered structure of the as-prepared sample is shown in Figure 3-13a. Both the bright field image and the diffraction pattern indicate that the structure is predominantly amorphous. After a thermal treatment of 400°C for 2 minutes in vacuum, the layered structure is still stable and displays an amorphous structure within the layers, as seen in Figure 3-13b. Annealing at 600°C for 30 minutes, however, results in destruction of the layered structure by agglomeration of the Ru films, shown in Figure 3-13c. The Ru films have agglomerated and crystallized into almost spherical crystallites with diameters on the order of a few nanometers, similar to that observed in the plan-view samples. The sizes of these crystallites are much larger than the initial bilayer thickness of the multilayer, which suggests that during agglomeration, Ru from

adjacent layers may coalesce. The rings in the diffraction pattern indicate a preferred orientation with the <101> direction of the elemental Ru normal to the film surface.

The interface between the agglomerated multilayer and the C buffer layer appears quite uniform and continuous in Figure 3-13c. After the sample is ion-milled to a thickness transparent to the electron beam, the multilayer has a trapezoid configuration in the wedged-shape TEM specimen where the multilayer/carbon interface is the base of the trapezoid. Imaging with the electron beam parallel to the base of the trapezoid thus produces an image from a thick region of many Ru grains, and results in an image of a smooth and uniform interface. A single layer of Ru grains at one corner of the base of the trapezoid sample can be viewed by tilting the TEM specimen in the direction perpendicular to the film surface. The interface then appears like that of an agglomerated structure, as seen in Figure 3-13d. The morphology of single Ru grains is almost spherical crystallites that appear to be separated from each other in a carbon matrix. Similar morphologies occur at the surface of the agglomerated structure, which is the interface between the multilayer and the epoxy layer in this figure.

Partial agglomeration of the Ru layers is observed in a 3.5 nm period Ru/C multilayer with 1.4 nm thick Ru layers when annealed for a longer time. The as-prepared multilayer has a predominantly amorphous structure, with evidence of Ru micro-crystallites in the Ru layers. After annealing at 600°C for one hour, grain growth and agglomeration are observed in the Ru layers, as shown in Figure 3-14. The size of the Ru grains ranges from approximately 2 to 12 nm in the plane of the layers and extends up to 3 nm in the perpendicular direction. The multilayer structure is still apparent, as indicated by the multilayer spots in the diffraction pattern. The interfaces however are no longer smooth and flat. Low angle x-ray diffraction of the annealed sample still shows pronounced peaks at the Bragg angles, although these peaks have

decreased substantially after annealing. A map of sinusoidal shape can be traced at the interfaces between the Ru and the C layers in Figure 3-14, although the sinusoidal waves from different interfaces do not conform to each other in the direction perpendicular to the interface. The Ru grains in each layer appear to be separated from each other, which results in discontinuous layers, as can be seen in the thinner region of the sample.

To study the effects of Ru and C layer thickness on stability of the Ru layers, samples of two thickness combinations were prepared and studied: one with the thickness of the C layers doubled, and one with the thickness of the Ru layers doubled, while keeping the thickness of the other material layers constant at 1 nm. The microstructure of a 1 nm Ru / 2 nm C, and a 2 nm Ru / 1 nm C multilayer, annealed at 600°C for 30 minutes, are shown in Figure 3-15a and 3-15b, respectively. As can be seen from Figure 3-15a, the 1 nm Ru layers sandwiched between the 2 nm C layers have clearly agglomerated, similar to the observation of the 1 nm Ru / 1 nm C structure annealed under the same condition. The 2 nm Ru layers sandwiched between the 1 nm C layers in Figure 3-15b however still remain stable under the same annealing condition. Close examination of the Ru layers in this sample shows that the Ru grains span the whole thickness of the layers, and are as big as a few ten of nanometers wide in the plane of the layers. Under the same annealing condition, evidently, agglomeration of the Ru layers depends more on the thickness of the Ru layers than that of the C layers in such a Ru/C sandwich structure. The starting microstructures of the Ru layers in these two samples before annealing, however, are different from each other. The Ru layers in the as-prepared 1 nm Ru / 2 nm C sample are predominantly amorphous, while those in the 2 nm Ru / 1 nm C are polycrystalline. Grain growth was observed in the thicker crystalline sample, and the layered structure remains stable. In the thinner samples, the as-deposited amorphous Ru layers represent a very different initial state of higher free energy, from which different kinetic pathways leading to agglomeration are followed.

Annealing of the thicker Ru layers for longer time, however, results in agglomeration of the layers. Figure 3-16 shows the cross-sectional images of 2 nm Ru / 1 nm C, and of 2 nm Ru / 2 nm C multilayers, annealed at 600°C for 10 hours. Both structures show that they clearly agglomerated under this annealing condition. The Ru grains in the 2 nm Ru / 1 nm C sample seem to span the thickness of the whole multilayer, which is approximately 15 nm thick, while the 2 nm Ru / 2 nm C sample shows evidence of partial layering, with the thickness of the agglomerated Ru layers at no more than 5 nm thick. The thinner C layers in the first sample thus provide a shorter diffusion path for the Ru atoms from different layers to form larger grains.

3.5.2 *In-Situ* TEM Studies

To understand the mechanism of agglomeration in the 2 nm period Ru/C multilayers, *in-situ* TEM in cross-section was used to obtain a dynamical examination of the microstructural and morphological evolution of the layers. For the *in-situ* TEM experiment, M-Bond 610 epoxy was used to prepared the samples. The samples were studied in a JEOL JEM 200CX AEM equipped with a hot stage single tilt side entry holder, operating at 200 kV. The specimen was loaded such that the tilt direction was perpendicular to the film interface to allow observation of the multilayer in a direction as close to the cross section as possible. Bright field images and selected area diffraction (SAD) patterns were taken at various temperatures during heating, and at various times while keeping at a constant temperature, 500°C. Careful recording of the SAD patterns was used to determine the order of occurrence of agglomeration and crystallization in the Ru layers by observing the disappearance of the multilayer periodicity diffraction spots, and the appearance of the Ru polycrystalline rings, respectively, in the diffraction patterns.

Figure 3-17 shows a series of TEM images and their corresponding diffraction patterns taken during heating in the microscope. The as-prepared sample, shown earlier in Figure 3-11a, shows flat and continuous layers with well-defined interfaces. This layered structure is stable up to approximately 500°C. Figure 3-17a shows a cross-sectional TEM bright field image of the multilayer and its corresponding SAD pattern taken at 423°C. The SAD pattern shows the [110] spots of the Si substrate, and the finely spaced spots produced by electron scattering from the periodicity of the multilayer. The presence of the high order multilayer diffraction spots provides a good indication of the uniform layers and the layered structure of the multilayer.

The temperature was kept constant at 500°C after ramping, with an uncertainty of ±10°. After 10 minutes, the interfaces appear sinusoidal with a wavelength comparable to the multilayer period. The layered structure however is apparent, as can be seen in Figure 3-17b. Some of the high order multilayer spots are indeed still present in the corresponding SAD pattern, which indicates that the layers are still periodic though not as uniform as before. The SAD pattern also shows a faint diffuse ring at the approximate spacing of the (101) planes of elemental Ru, which indicates either some short range order or some initial nucleation of the crystalline Ru phase. Higher order multilayer diffraction spots in the SAD pattern begin to disappear after about 15 minutes at 500°C, and at the same time, other rings of the hexagonal Ru phase become more visible, confirming the formation of the crystalline Ru phase. Figure 3-17c shows the multilayer after 25 minutes in the *in-situ* microscope. The multilayer has almost lost its layered structure, and all but the first order diffraction spots have disappeared. Most of the long Ru grains seen in Figure 17b have grown into a more spherical structure (arrow A). Some larger Ru grains grow to combine with grains from the adjacent Ru layers and form grains that are larger than the initial multilayer period (B). After approximately 30 minutes, the Ru layers have completely agglomerated into almost

spherical grains. The periodicity of the multilayer is destroyed, and accordingly, the remaining multilayer spot in the SAD pattern disappears and the Ru rings become more visible. Figure 3-17d shows the multilayer microstructures of the sample after annealing for 90 minutes and subsequently cooled back to room temperature. The microstructure is not significantly different from that at elevated temperature, and shows Ru grains of approximately 4 nm in diameter, a dimension that is approximately twice the initial bilayer period.

The evolution observed in the *in-situ* experiment is consistent with *ex-situ* annealing experiments. A piece of sample was heated in a vacuum furnace before being prepared for cross-sectional TEM observation. The sample was then studied in the high resolution electron microscope. A bright field image of the *ex-situ* sample is shown in Figure 3-17e. The figure shows a microstructure similar to that in Figure 3-17d, and the grain size of the Ru crystallites in both images is approximately the same. The *in-situ* results suggest that diffusion of the Ru and/or C atoms leads to agglomeration of the Ru layers and subsequently to nucleation of the Ru crystallites, although crystallization and grain growth occur before completion of the agglomeration process. Continuous recording by means of video-taping, and *in-situ* high resolution TEM would be helpful in determining more conclusively the order of agglomeration and crystallization.

3.5.3 Grain Size Distribution Studies

For the Ru grain size evolution study, samples of nominally 1, 2, and 4 nm Ru layer thicknesses were prepared as multilayers sandwiched between various thicknesses of C films. Three thicknesses of C were deposited for each Ru thickness, such that the Ru-to-C layer thickness ratios were 0.5, 1, and 2. The nanometer thicknesses of the Ru and C layers in the Ru/C multilayer samples containing the 1 nm thick Ru layers hence

were 1/2, 1/1, and 1/0.5. Similarly, the layer thicknesses of the samples containing the 2 and 4 nm thick Ru layers were 2/4, 2/2, 2/1, and 4/8, 4/4, and 4/2, respectively.

The as-prepared Ru films exhibit a predominantly amorphous structure in the 1 and 2 nm films, and have some micro-crystallites in the 4 nm Ru films, for all thicknesses of C films prepared. The plan-view TEM samples annealed at 400°C for 2 minutes and for 30 minutes show no significant differences in their microstructure from the as-prepared samples. The electron diffraction patterns from all three post-annealed Ru film thicknesses show very diffuse rings signifying a predominantly amorphous structure. Further annealing at 600°C for 30 minutes results in elemental Ru micro-crystallites with grain size of the order of a few nanometers. Annealing at higher temperature or longer time is required to induce further grain growth or coarsening of these grains.

The microstructure of Ru crystallites for the three thicknesses of Ru films sandwiched between different thicknesses of C films after annealing at 800°C for 30 minutes is shown in Figure 3-18. The bright field images in Figures 3-18 a-i display the images of samples with the same Ru layer thickness in each row; 1 nm, 2 nm, and 4 nm thick Ru layers are in the first, second, and third row, respectively. Each column in Figure 3-18 has the same Ru-to-C layer thickness ratio of 0.5, 1, and 2, in the right, center, and left column, respectively. The electron diffraction patterns of the 4 nm Ru layer samples in Figures 3-18 g-i are shown as example in Figures 3-18 k-m. The polycrystalline rings in these diffraction patterns originate from elemental Ru crystallites.

Several trends in Ru grain size are apparent from Figure 3-18. First, the grain size distribution in samples with 2 and 4 nm thick Ru layers in Figures 3-18 d-i is relatively constant. The Ru grain size in these samples is approximately on the same order as the

Ru film thickness, which is consistent with the grain size observed from cross-sectional TEM samples. Second, in contrast to the 2 and 4 Ru layers, the grain size in the 1 nm Ru film increases with decreasing C film thickness. The thinnest as-deposited Ru layers studied are the most highly disordered and hence have the strongest driving force for crystallization. Higher surface-to-volume ratios of structures with thinner C layers also provide additional driving force for crystallization and grain growth of the Ru crystallites. Indeed it is possible that the thinnest C layers in Figure 3-18c may not be continuous in the as-deposited sample. The microstructure of the 1 nm Ru / 2 nm C multilayer in Figure 3-18a shows a highly dispersed composite of approximately one-nanometer diameter grains of Ru in a C matrix. Third, comparison of Figures 3-18 c, f, and i showing samples with the same Ru-to-C layer thickness ratio also indicates that the grain size increases with decreasing layer thickness of Ru and/or C. Thus thinner as-deposited Ru or C layers result in larger Ru grain sizes, contrary to the expectation that grain size is proportional to the film thickness.

3.6 Ru/B_4C SYSTEM

The microstructure of as-prepared Ru/B_4C multilayers shows similar evolution to that of the other elemental metal/C systems. The Ru layers in the Ru/B_4C multilayers have an amorphous structure at short period, and a polycrystalline structure at longer period. Their responses to thermal annealing however are more similar to those of the W/C multilayers to those of the Ru/C system. Cross-sectional TEM observation of a 2.6 nm-period Ru/B_4C multilayer annealed at 600°C for 30 minutes reveals a predominantly amorphous structure in both the Ru and the B_4C layers. Crystallization or recrystallization of the Ru layers to form a boride phase (RuB_2) is observed in longer period multilayers after annealing. Figure 3-19 shows a) the cross-sectional TEM image

of the annealed 2.6 nm-period multilayer, and b) the plan-view diffraction pattern of an annealed 5 nm-period multilayer. The polycrystalline rings in the electron diffraction pattern are identified as those of the RuB_2 phase. Crystallization of the boride phase however occurs in annealed multilayers with period as short as 3.5 nm. Figure 3-20 shows the cross-sectional high resolution TEM image of a 3.5 nm-period multilayer that has been annealed at 600°C for one hour. The nominal thickness of the Ru layer is 1.4 nm in this sample. Lattice fringes of the boride phase can be observed readily in the Ru-rich layers. The grain size of the boride grains is of the same order as the thickness of the layers. Formation of the boride phase in the Ru-rich layers suggests that boron atoms from the amorphous B_4C layers diffuse into the metal-rich layers during annealing. It is expected then that the remaining amorphous layers are richer in carbon than they were before annealing. The microstructures of as-prepared and annealed Ru/B_4C multilayers are summarized also in Table 3-3.

3.7 Cu/C SYSTEM

Attempts to fabricate short period Cu/C multilayers have been unsuccessful,[32] and in this study, sequential sputtering was used to fabricate a 3 nm-period multilayer, but the result was random clustering of the Cu crystallites in a C matrix (Figure 3-21). From Figure 3-21, the Cu crystallites measure approximately 2 nm in diameter, which is significantly thicker than the supposed 1.2 nm Cu layer. The clustered structure of the Cu/C multilayer shown in Figure 3-21 is similar to the agglomerated structure of the annealed 2 nm-period Ru/C shown in Figure 3-11b. Both the Cu clusters and the Ru crystallites have diameters that are larger than the initial or intended layer thicknesses. The Ru/C system however is layered during deposition and agglomerates upon annealing, while the Cu/C system clusters during deposition.

Annealing behavior of different period Cu/C multilayers differs from that of the Ru/C system. Agglomeration, crystallization and grain growth of elemental Ru crystallites were observed in the Ru/C multilayers after annealing. In the Cu/C system, however, the Cu in short period multilayers forms amorphous clusters, while grain growth of Cu crystallites is observed in longer period multilayers. Figure 3-22 shows the plan-view electron diffraction patterns of as-prepared and annealed 3 nm-period and 10 nm-period Cu/C multilayers. Both as-prepared samples show the presence of polycrystalline Cu. Upon annealing, the polycrystalline rings in the diffraction pattern of the 3 nm-period as-prepared sample (Figure 3-22a) disappeared (Figure 3-22b), which indicates that the crystalline structure has amorphized. The polycrystalline rings in the diffraction pattern of the 10 nm-period as-prepared multilayer (Figure 3-22c), on the other hand, became sharper, which signifies the presence of larger grains in the annealed sample (Figure 3-22d).

3.8 TABLES

Table 3-1. Summary of the microstructures and phases in W/C and WC/C multilayers. As-prepared and annealed WC/C multilayers show an amorphous microstructure at all periods, while W/C multilayers show amorphous microstructure at short periods, and crystalline BCC W and hexagonal W_2C in respectively as-prepared and annealed longer periods.

Table 3-2. Summary of the microstructures and phases in Cr/C and CrC/C multilayers. All CrC/C multilayers are amorphous, while the microstructure of Cr/C changes with period and upon annealing.

Table 3-3. Summary of the microstructures and phases in Ru/C and Ru/B_4C multilayers. The as-prepared samples show amorphous microstructure at short periods and crystalline Ru at longer periods. The Ru grains in Ru/C multilayers grow into larger

crystallites upon annealing, while those in Ru/B_4C multilayers recrystallize to form the boride phase.

3.9 FIGURES

Figure 3-1. Plan-view TEM images of 2 nm-period a) as-prepared and b) annealed W/C multilayers showing the amorphous microstructure.

Figure 3-2. Plan-view TEM images of 12 nm-period a) as-prepared and b) annealed W/C multilayers. The rings in the diffraction pattern in a) are identified as those of BCC W, and those in b) are of W_2C.

Figure 3-3. Cross-sectional high resolution TEM images of 2 nm period a) as-prepared, and b) annealed, WC/C multilayers, showing the stability of the predominantly amorphous layered microstructures upon annealing at 500°C for 4 hours.

Figure 3-4. Cross-sectional high resolution TEM images of 12 nm period a) as-prepared, and b) annealed, WC/C multilayers, showing the stability of the predominantly amorphous layered microstructures upon annealing at 500°C for 4 hours.

Figure 3-5. Plan-view TEM images of 12 nm period a) as-prepared and b) annealed WC/C multilayers confirming the amorphous structure found from cross-sectional observation. The faint rings in the annealed diffraction pattern indicate the possibility of a small fraction of the W_2C crystallites present in the structure along with the amorphous phase.

Figure 3-6. Cross-sectional high resolution TEM image of 5 nm-period Cr/C multilayer showing the amorphous structure.

Figure 3-7. Plan-view electron diffraction patterns of as-prepared and annealed 5 nm and 10 nm-period Cr/C multilayers.

Figure 3-8. A low magnification cross-sectional TEM image of an annealed 10 nm period Cr/C multilayer.

Figure 3-9. Cross-sectional high resolution TEM image of the annealed 10 nm period Cr/C multilayer showing the amorphous microstructure results from diffusion of the C atoms into the Cr layers.

Figure 3-10. Cross-sectional high resolution TEM image of as-prepared 4.3 nm period Ru/C multilayers. Lattice fringes of the Ru phase are observed in the Ru layers.

Figure 3-11. Cross-sectional high resolution TEM images of 2 nm period a) as-prepared and b) annealed multilayers. The Ru-rich layers in the as-prepared sample have agglomerated to form elemental Ru crystallites upon annealing at 500°C for 4 hours.

Figure 3-12. Cross-sectional high resolution TEM images of 10 nm period Ru/C multilayers. The Ru-rich layers in both a) as-prepared and b) annealed samples show elemental Ru microstructure. The arrows show the Ru grain boundaries at the Ru/C interfaces.

Figure 3-13. TEM images of as-prepared and annealed 1 nm Ru / 1 nm carbon multilayers: a) as-prepared, b) 400°C for 2 minutes, c) 600°C for 30 minutes, showing agglomeration in the Ru films, and d) sample in c) tilted perpendicular to the film surface to show the morphology and the crystallites and the interface.

Figure 3-14. Partial agglomeration of 1.4 nm thick Ru layers in 3.5 nm-period Ru/C multilayers after annealed at 600°C for one hour.

Figure 3-15. Cross-sectional TEM images of a) 1 nm Ru / 2 nm C, and b) 2 nm Ru / 1 nm C multilayers, both annealed at 600°C for 30 minutes. The thinner Ru layer multilayer agglomerates after annealing, while the other still remains layered.

Figure 3-16. Cross-sectional TEM images of annealed a) 2 nm Ru / 1 nm C, and b) 2 nm Ru / 2 nm C multilayers. Both multilayers agglomerate after annealed at 600°C for 10 hours.

Figure 3-17. Cross-sectional TEM image and diffraction pattern of 2 nm period Ru/C at a) 423°C, b) 500°C for 10 minutes, showing the Rayleigh instability-like structure, c)

500°C for 25 minutes of same area as in b), and d) same area after in-situ annealed at 500°C for 90 minutes, and cooled to room temperature.

Figure 3-18. Plan-view TEM images of a) 1/2, b) 1/1, c) 1/0.5, d) 2/4, e) 2/2, f) 2/1, g) 4/8, h) 4/4, i) 4 nm Ru / 2 nm carbon multilayers after annealing at 800°C for 30 minutes. The electron diffraction patterns in j)-l) correspond to the bright field images in g)-i), respectively.

Figure 3-19. a) Cross-sectional TEM image of an annealed 2.6 nm-period Ru/B_4C multilayer, b) Plan-view electron diffraction pattern of an annealed 5 nm period Ru/B_4C multilayer showing the polycrystalline rings of a boride (RuB_2) phase.

Figure 3-20. Cross-sectional high resolution TEM image of an annealed 3.5 nm period Ru/B_4C multilayer showing the lattice fringes of RuB_2 crystallites.

Figure 3-21. Attempt in fabrication of a 3 nm period Cu/C multilayer results in clustering of the Cu aggregates in a C matrix.

Figure 3-22. Plan-view electron diffraction patterns of as-prepared and annealed 3 nm period (attempted) and 10 nm period Cu/C multilayers.

	W/C		WC/C	
period	as-prepared	annealed	as-prepared	annealed
2 nm	amorphous	amorphous	amorphous	amorphous
4 nm	amorphous	amorphous	amorphous	amorphous
7 nm	amorphous + crystalline	xtalline	amorphous	amorphous
12 nm	amorphous + BCC W	BCC W + hex. W_2C	amorphous	amorphous

Table 3-1

Cr/C			Cr_3C_2/C	
period	as-prepared	annealed	as-prepared	annealed
2 nm	amorphous	amorphous	amorphous	amorphous
5 nm	amorphous	amorphous	amorphous	amorphous
10 nm	amorphous + BCC Cr	amorphous	amorphous	amorphous

Table 3-2

Ru/C			Ru/B_4C	
period	as-prepared	annealed	as-prepared	annealed
2 nm	amorphous	hex. Ru (agglom.)	amorphous (2.7 nm)	amorphous
5 nm	crystalline	hex. Ru	hex. Ru	RuB_2
10 nm	hex. Ru	hex. Ru	hex. Ru	RuB_2

Table 3-3

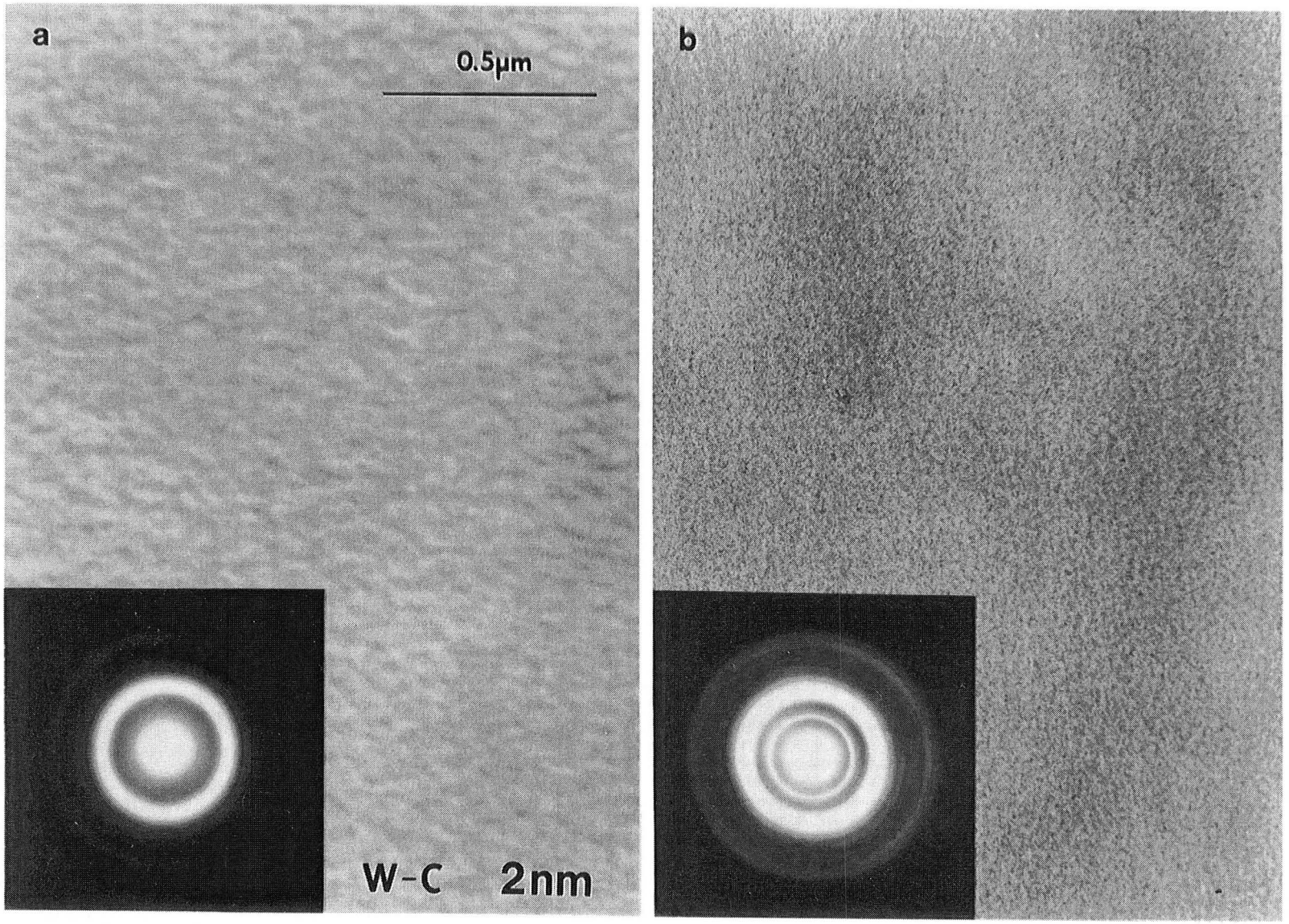

Figure 3-1

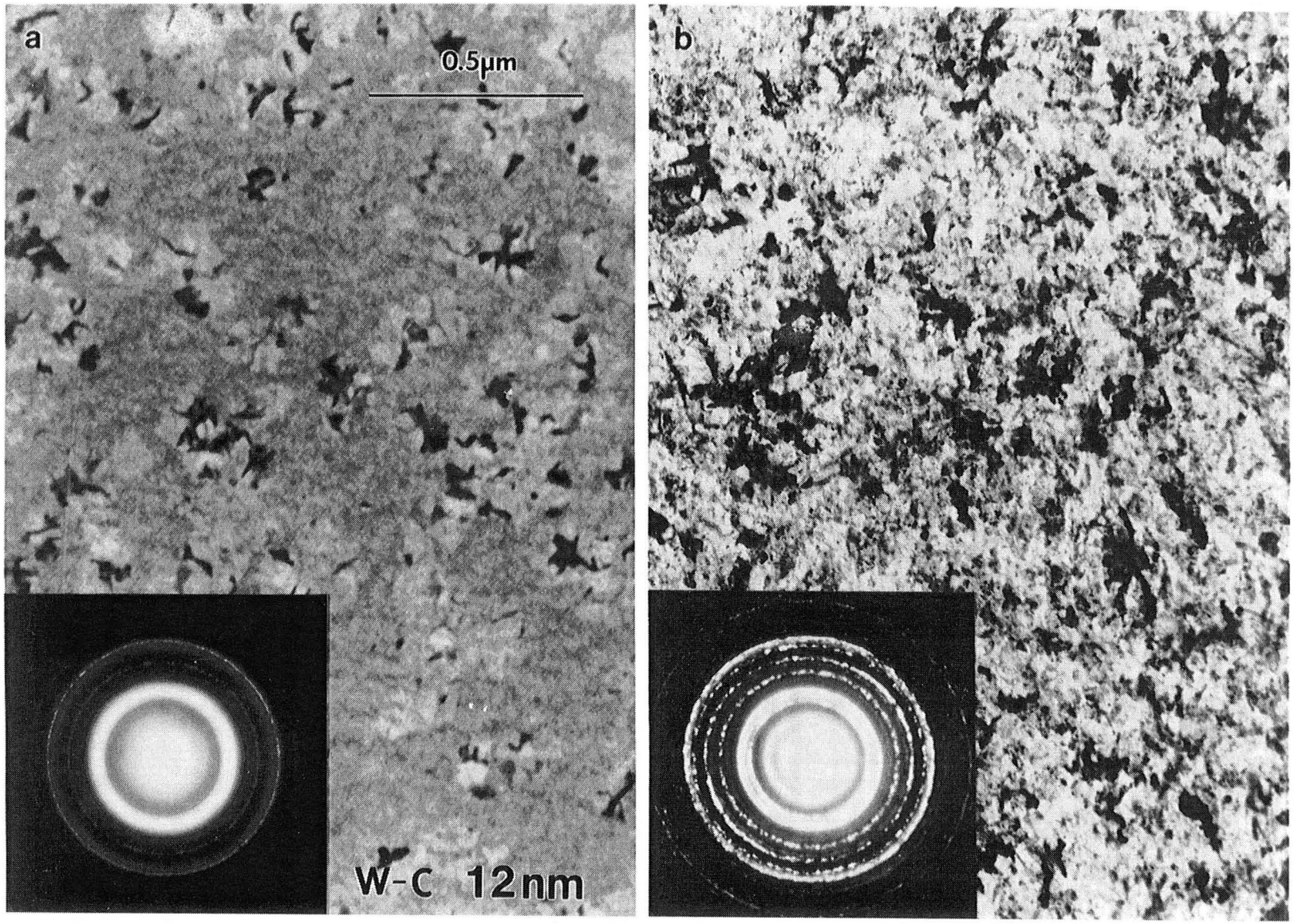

Figure 3-2

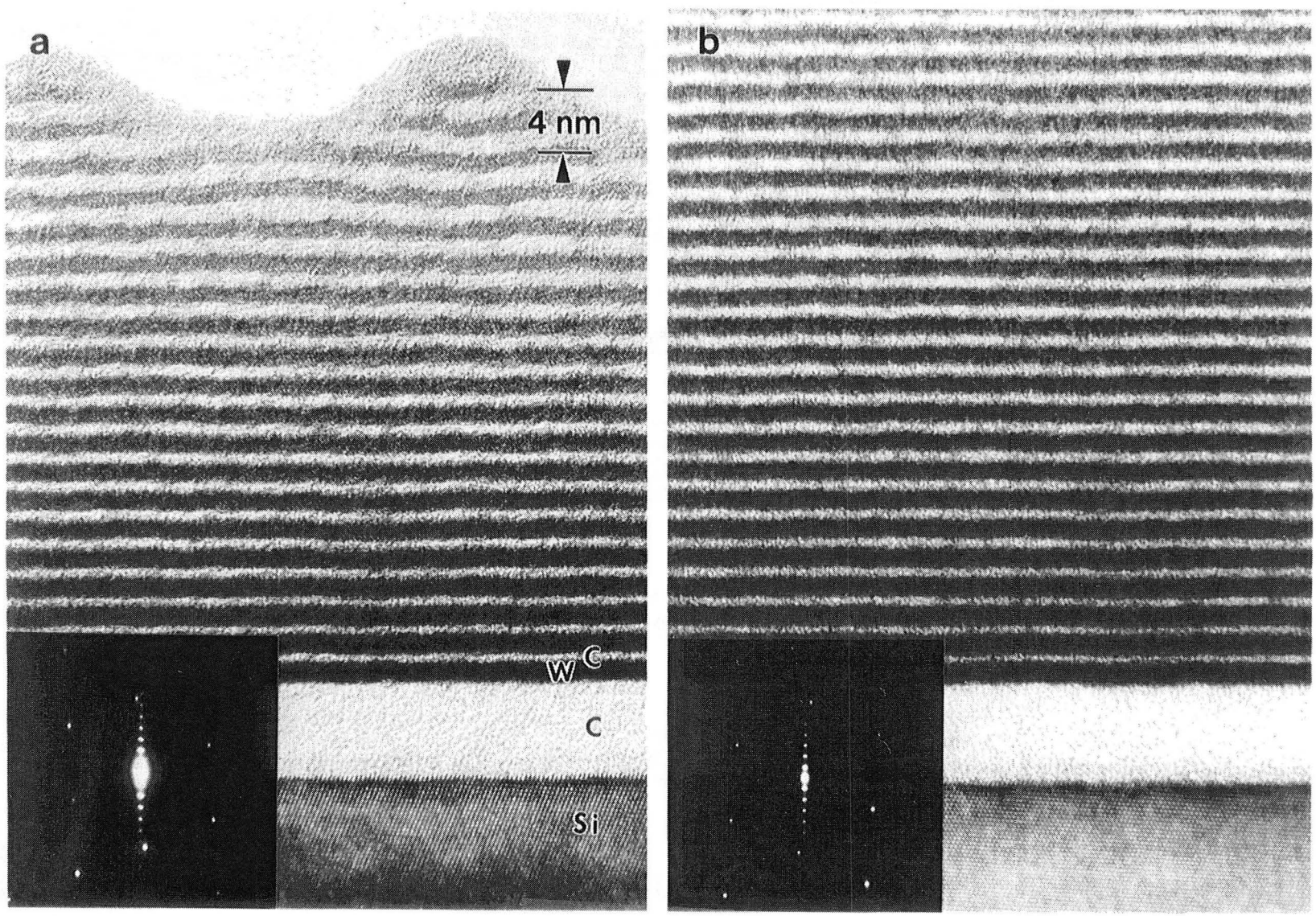

Figure 3-3

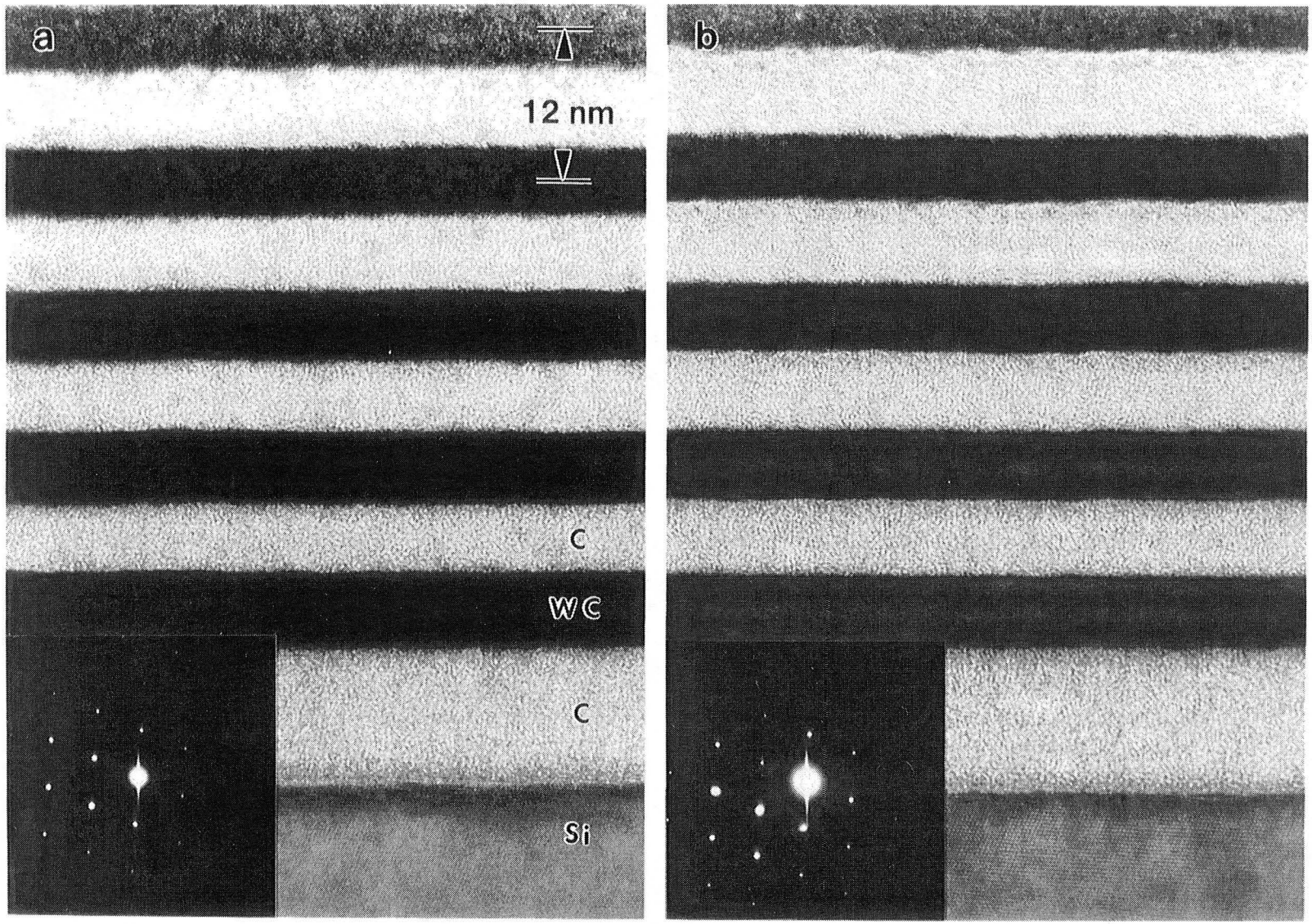

Figure 3-4

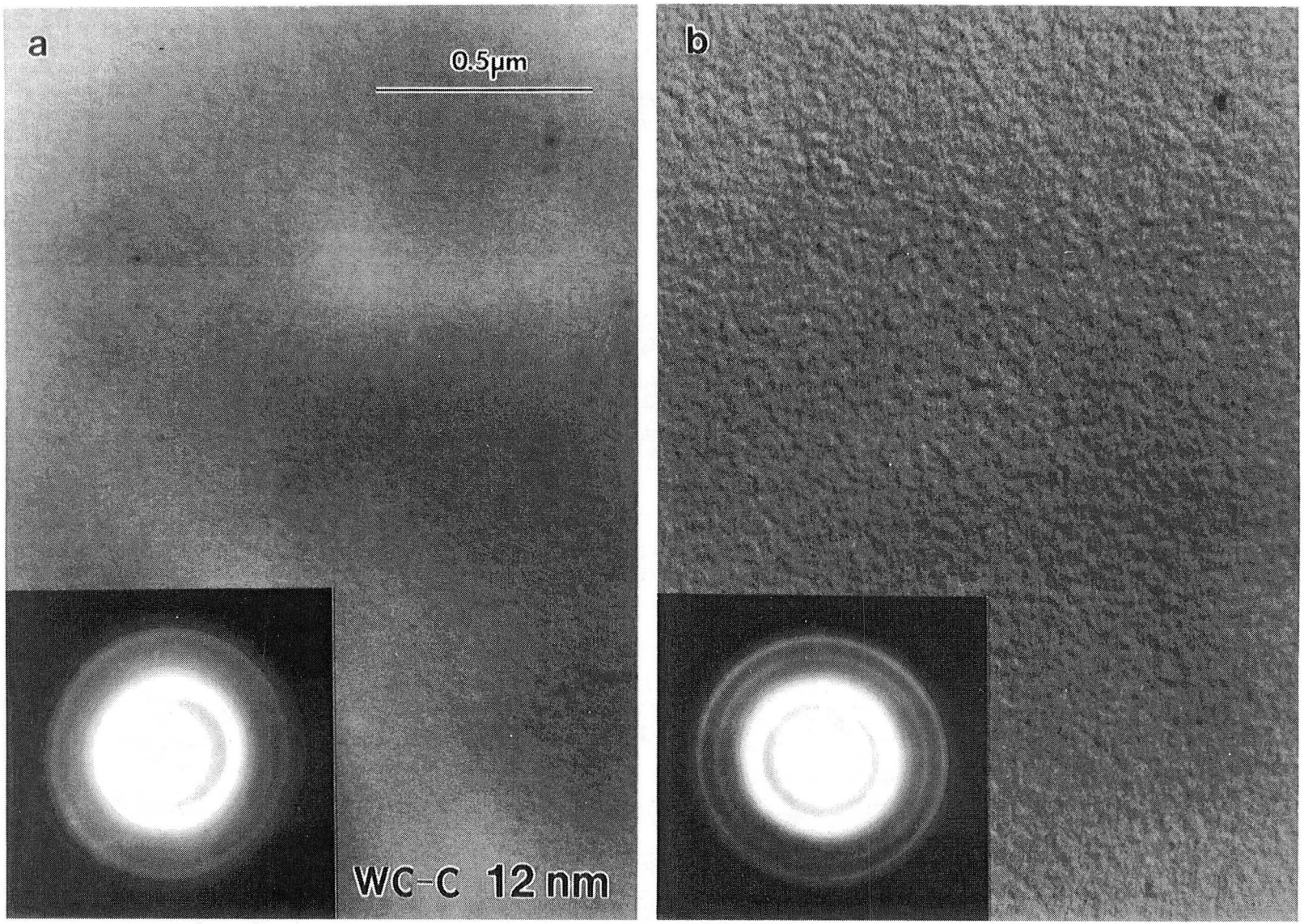

Figure 3-5

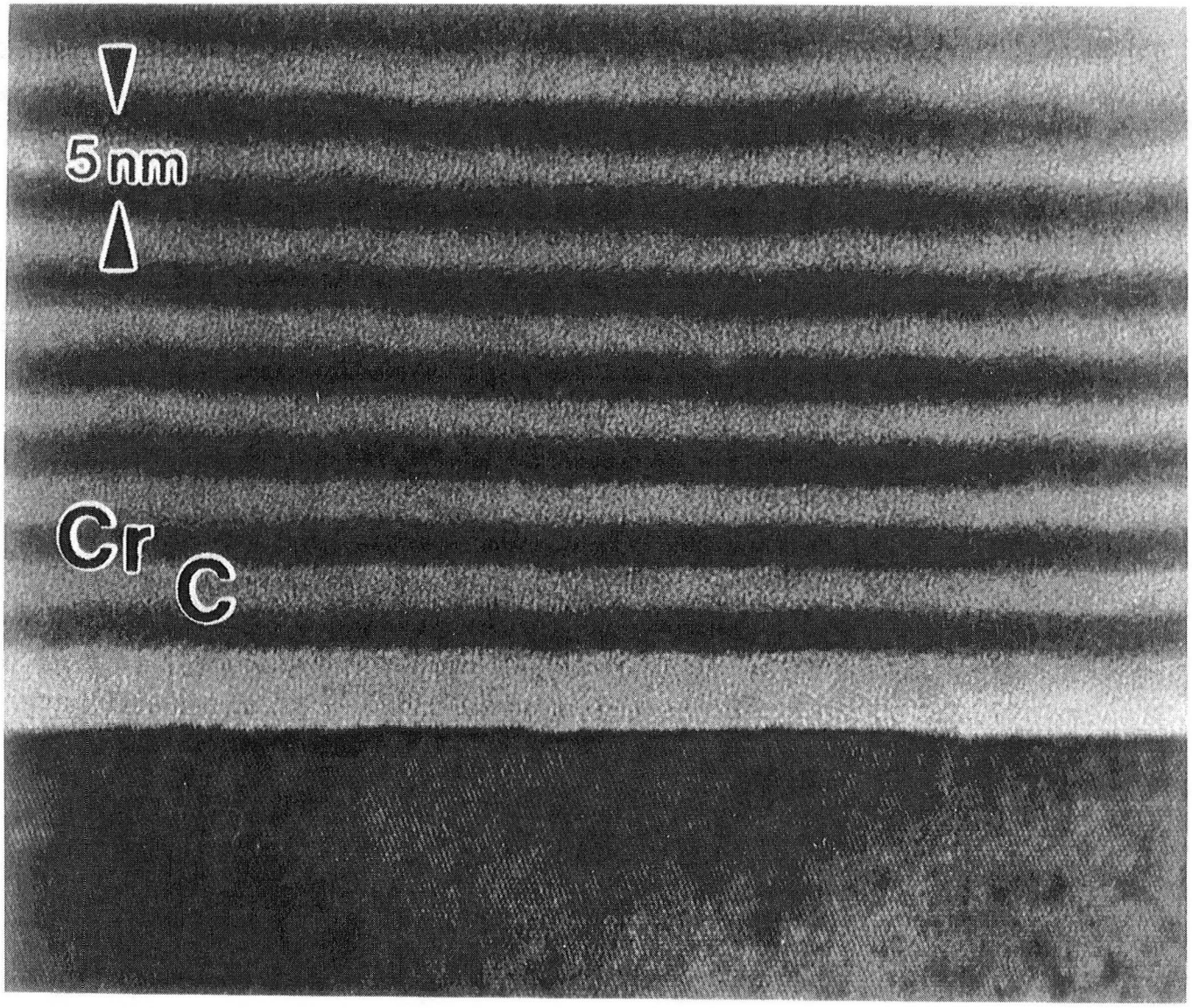

Figure 3-6

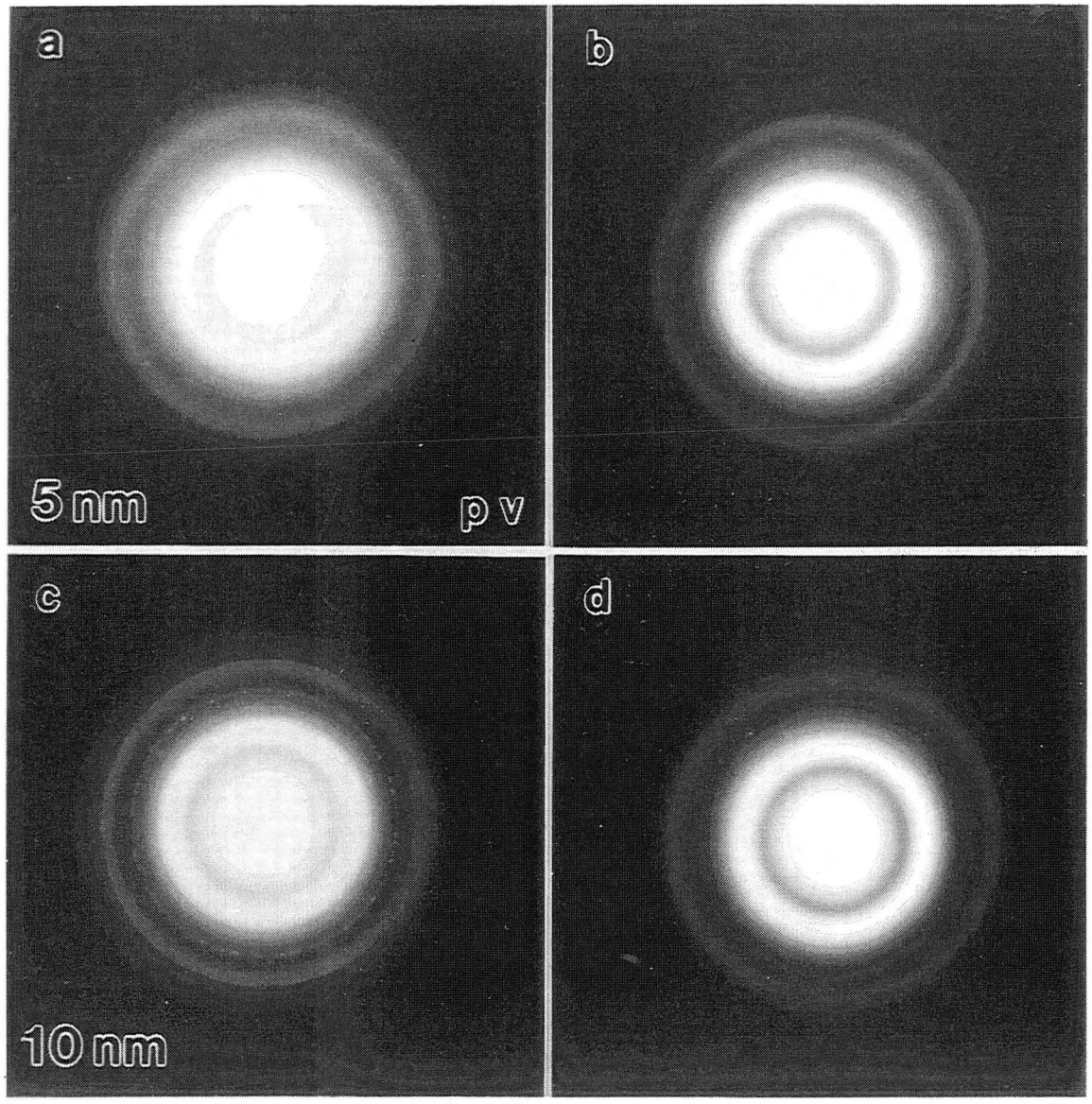

Figure 3-7

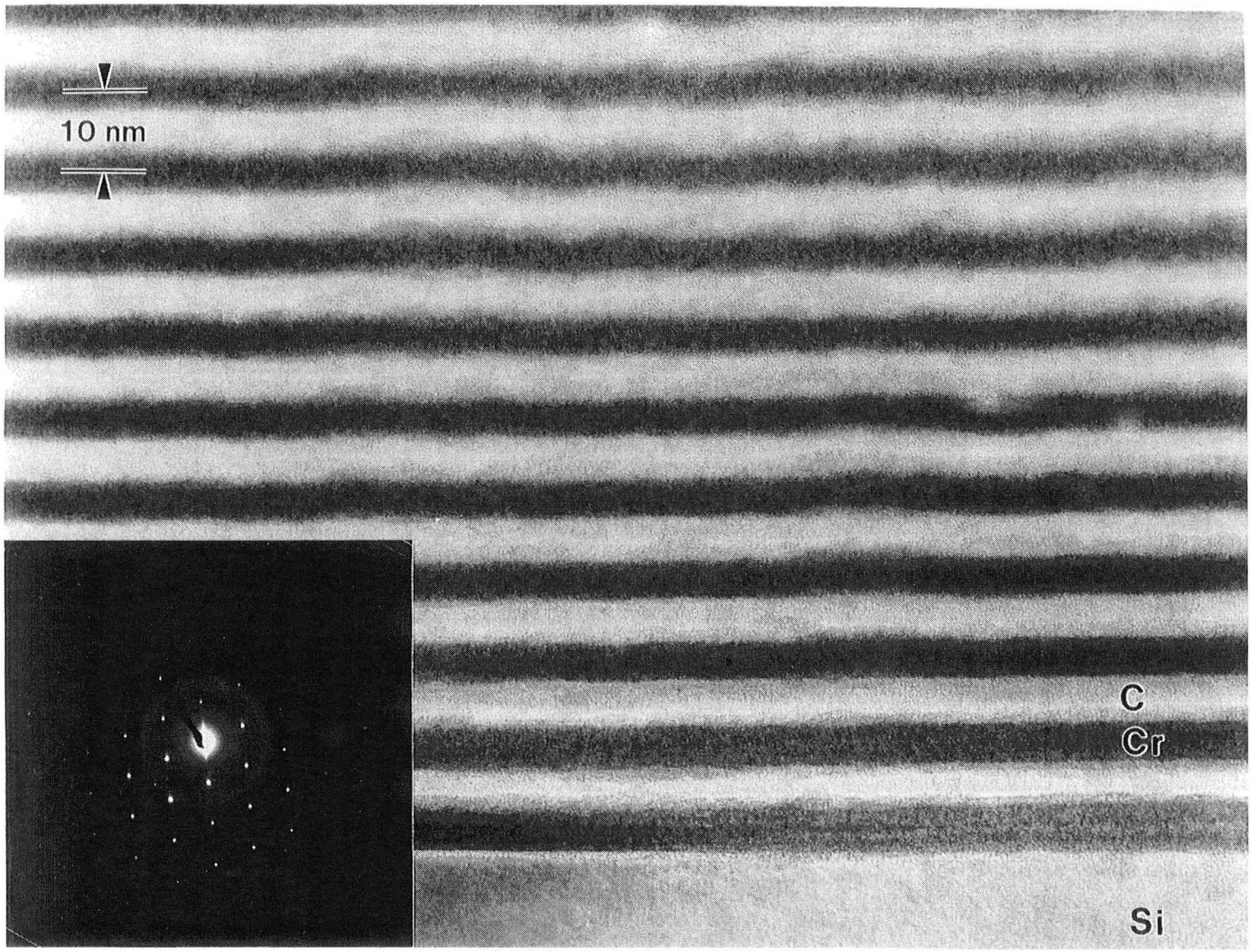

Figure 3-8

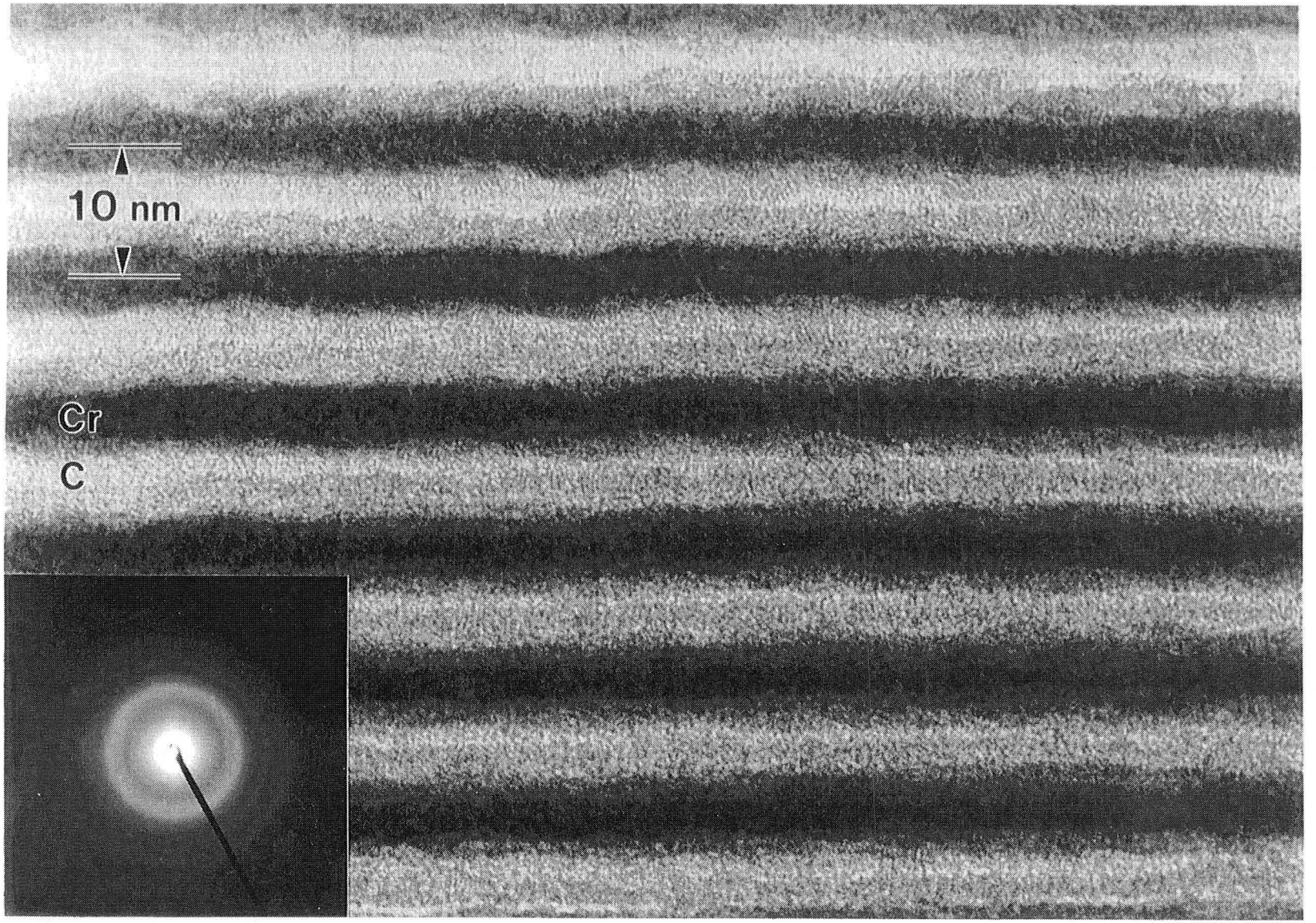

Figure 3-9

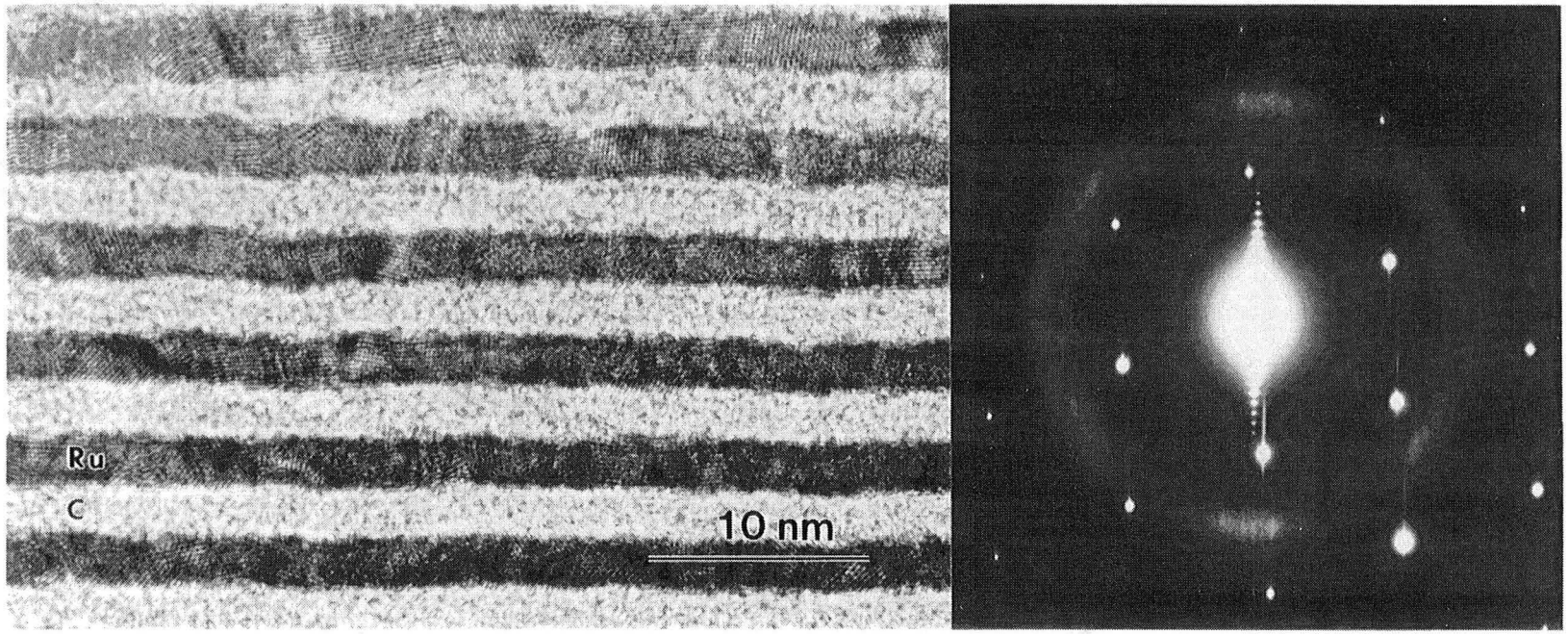

Figure 3-10

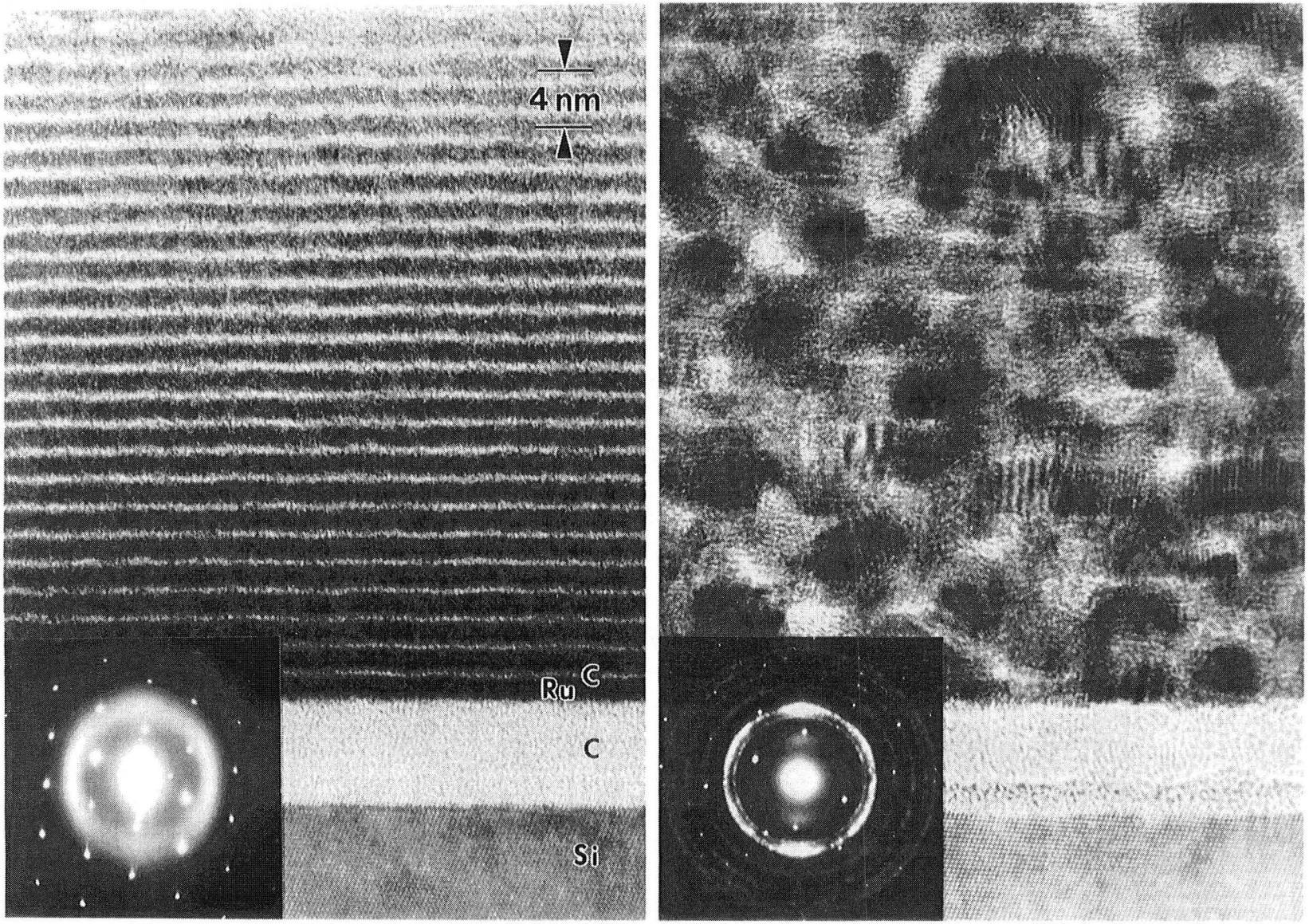

Figure 3-11

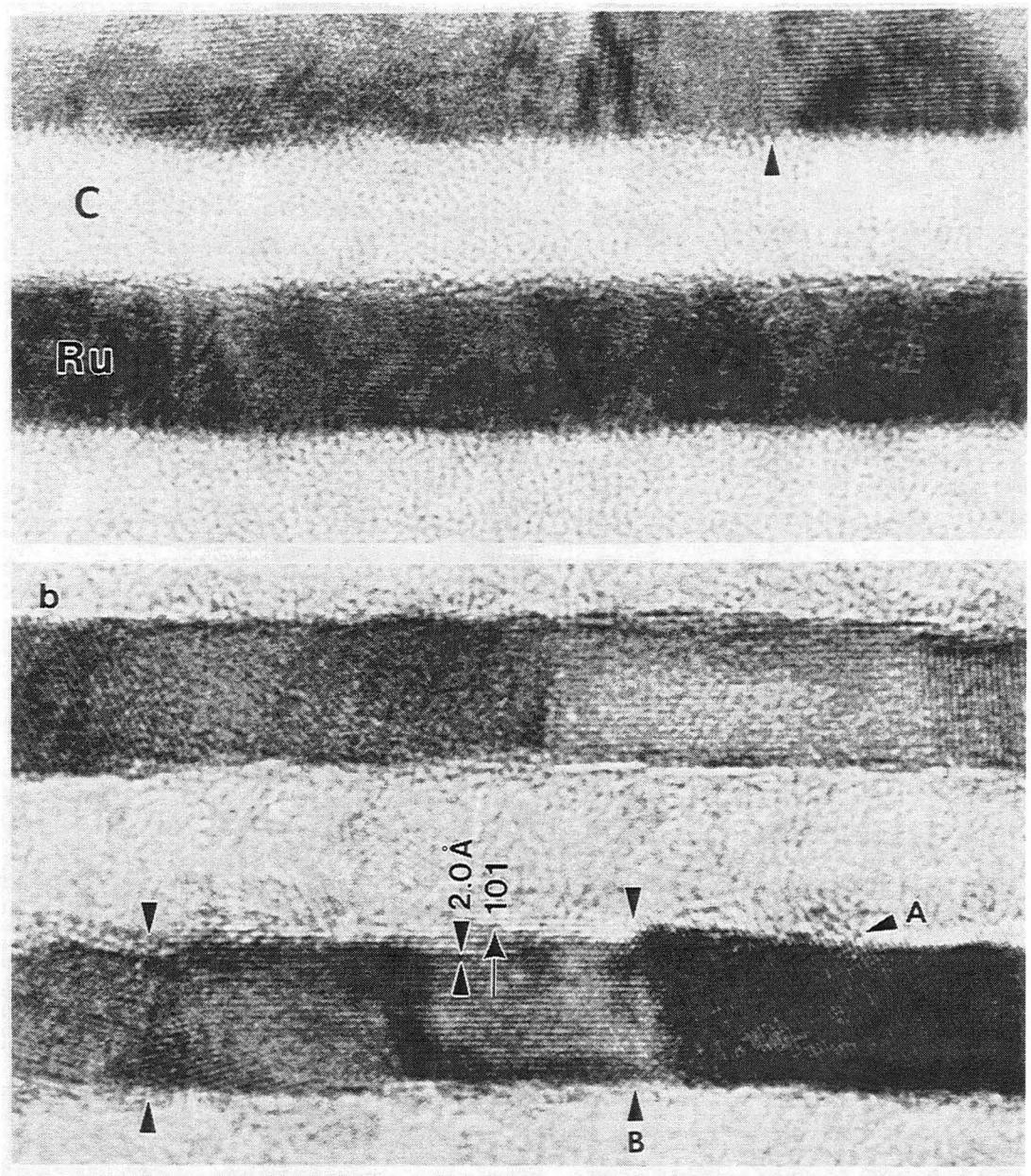

Figure 3-12

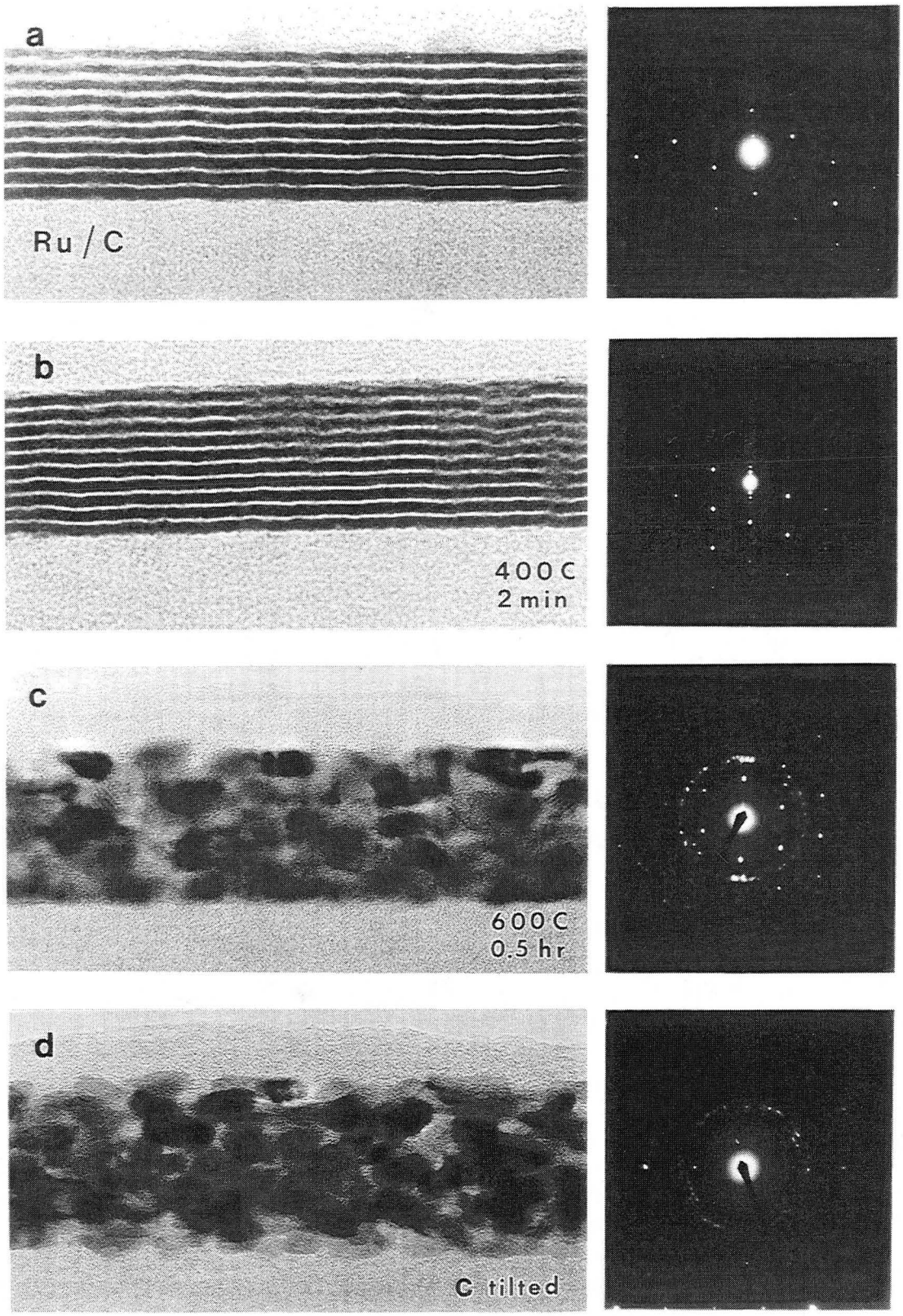

Figure 3-13

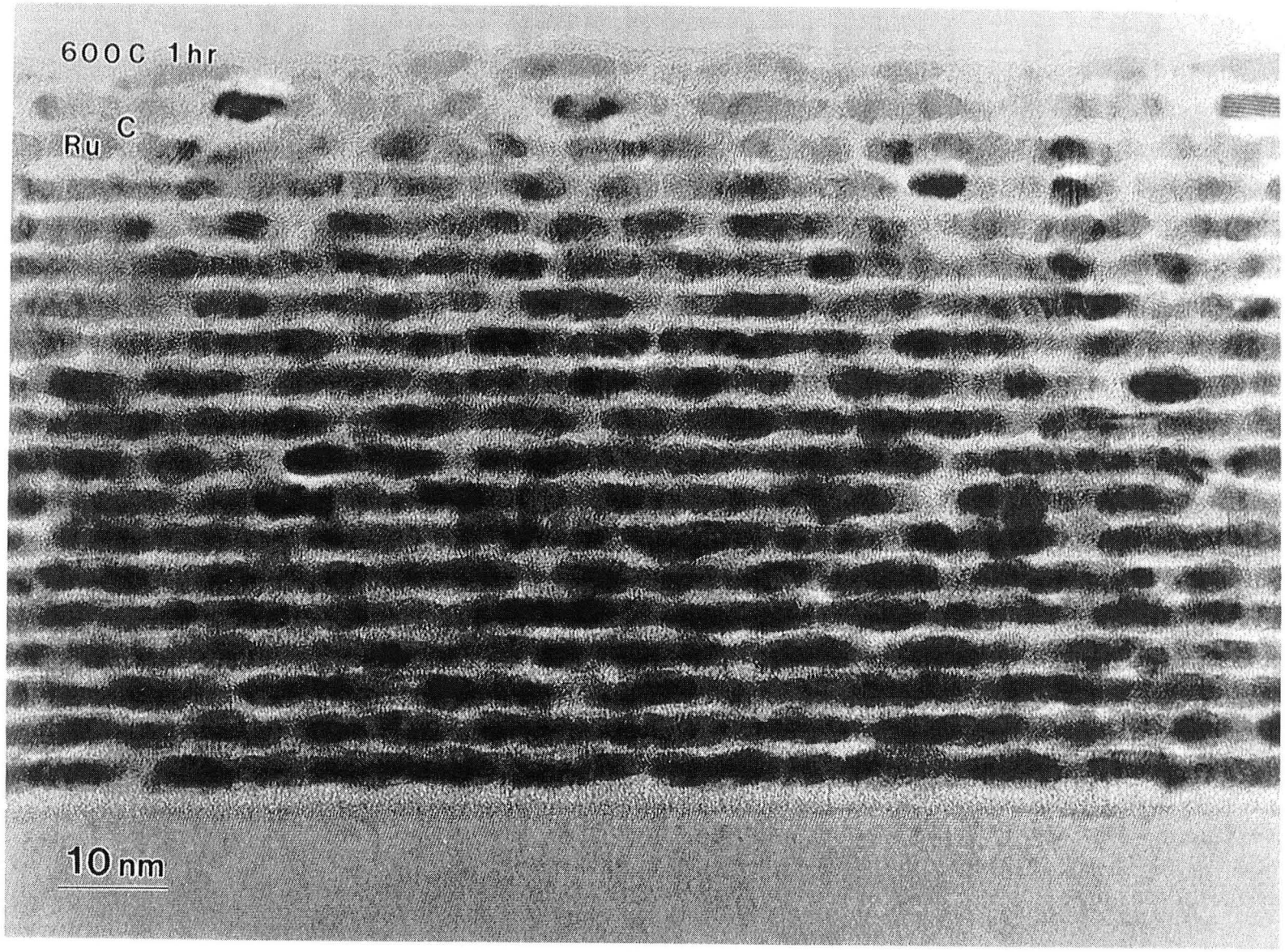

Figure 3-14

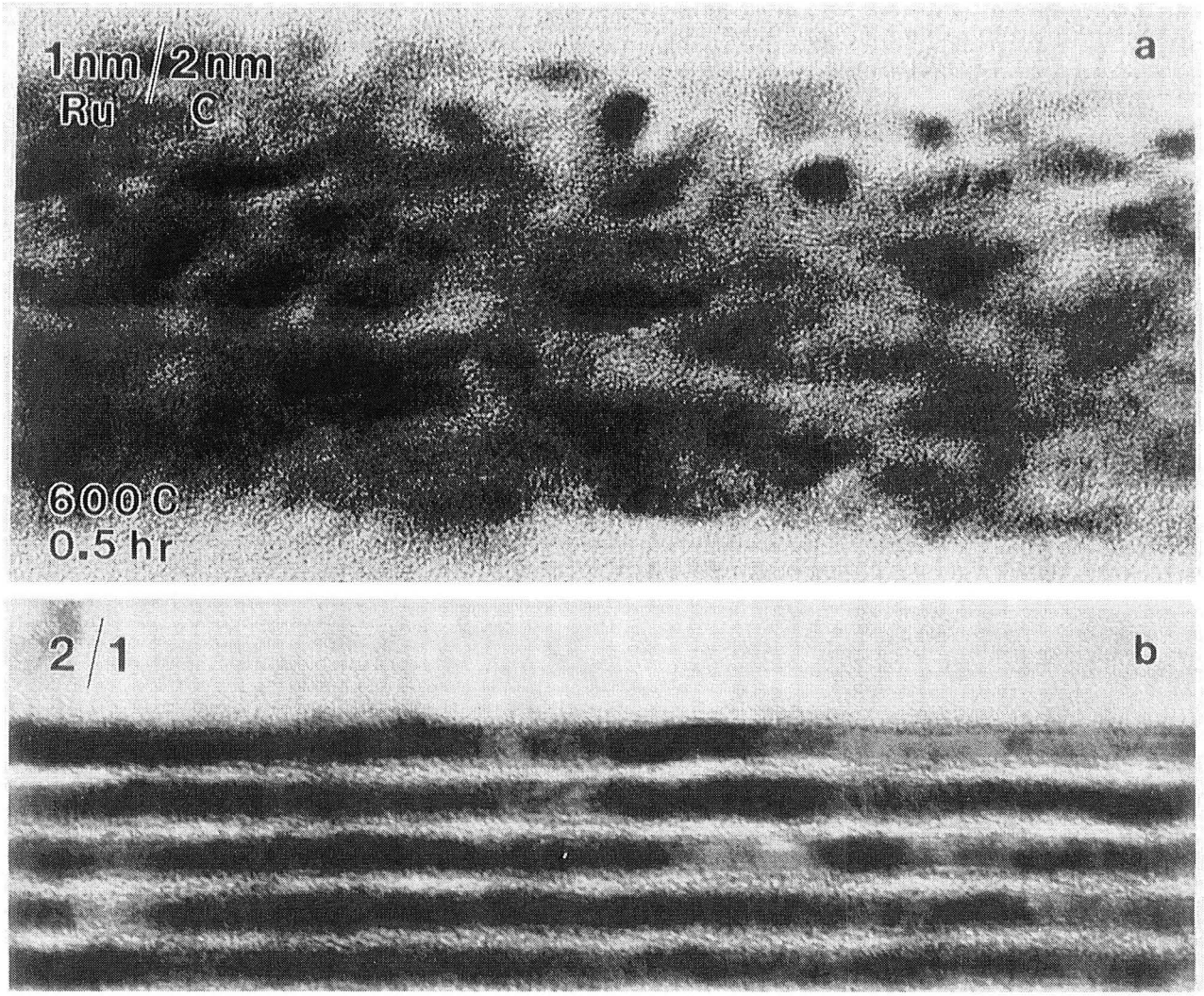

0.5 hr

Figure 3-15

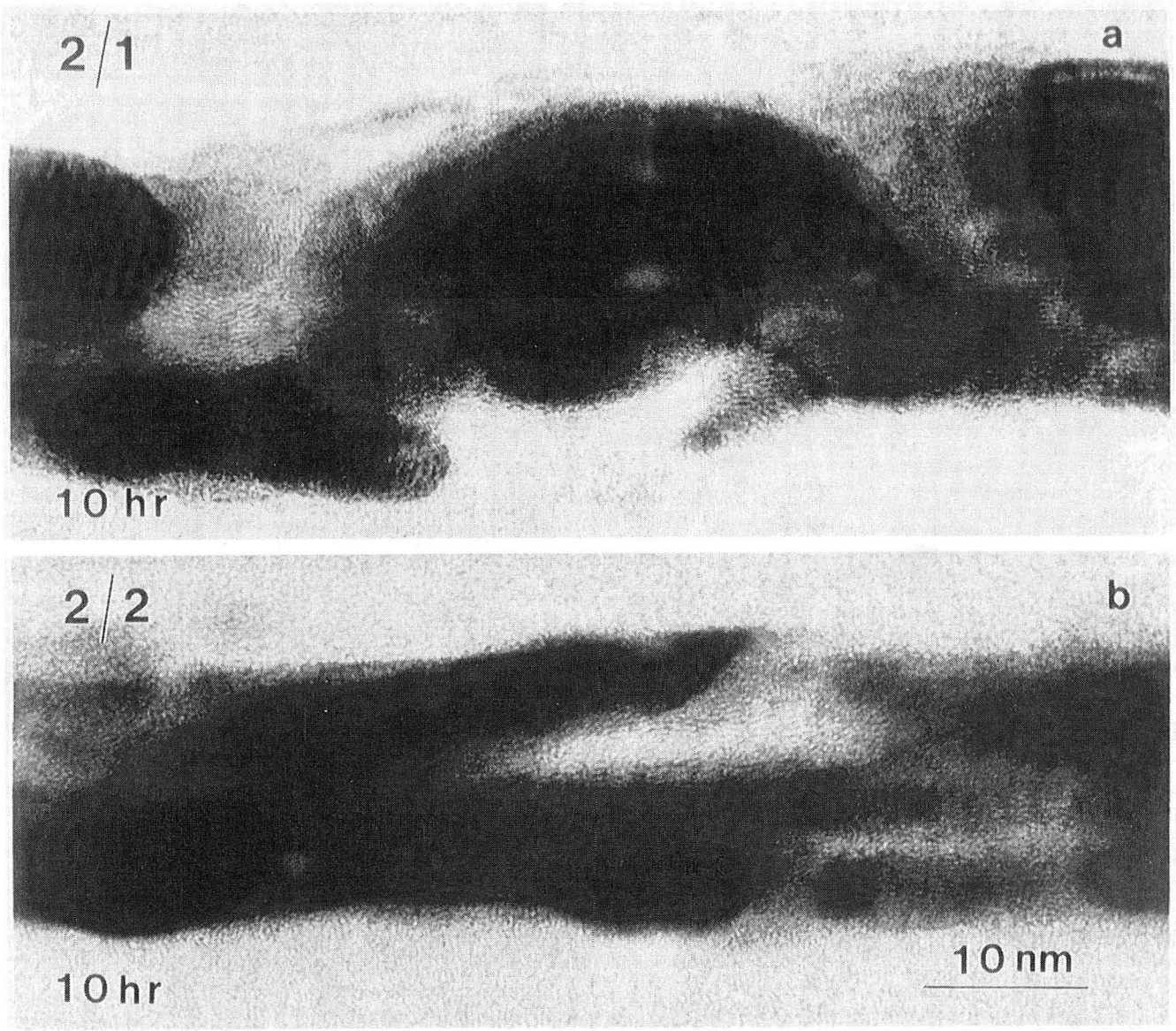

Figure 3-16

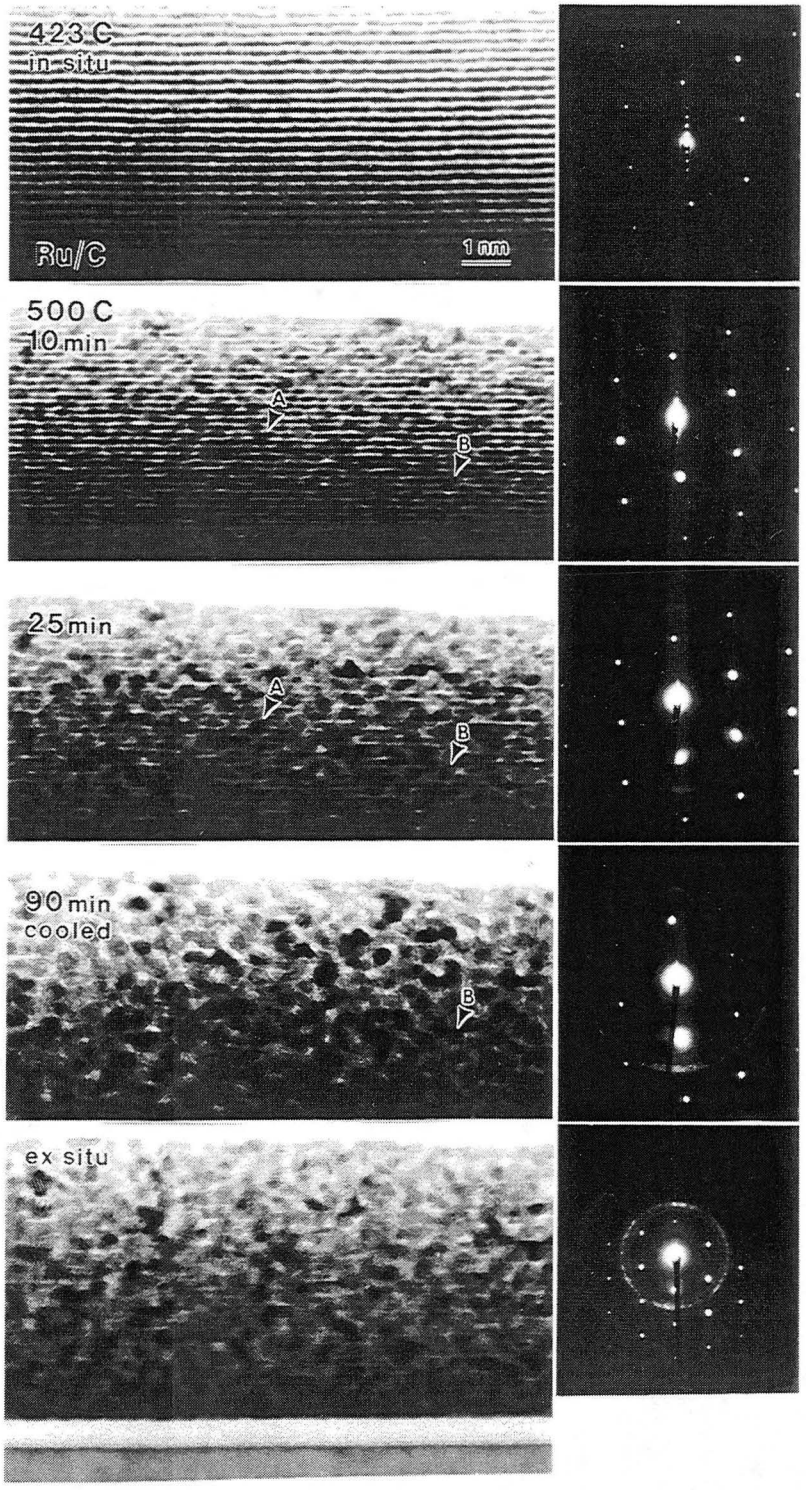
423 C
in situ
Ru/C
1 nm
500 C
10 min
A
B
25 min
A
B
90 min
cooled
B
ex situ

Figure 3-17

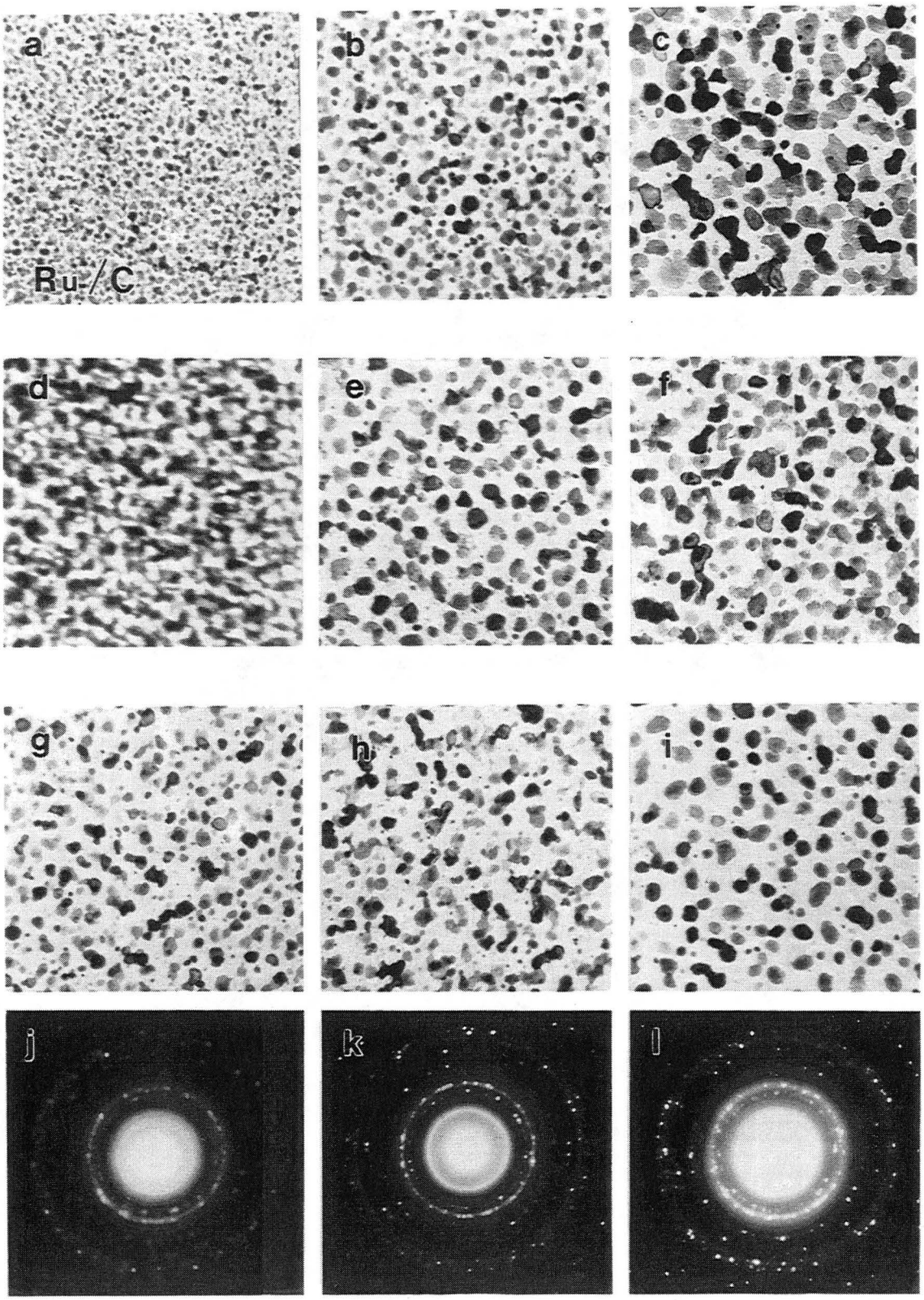

Figure 3-18

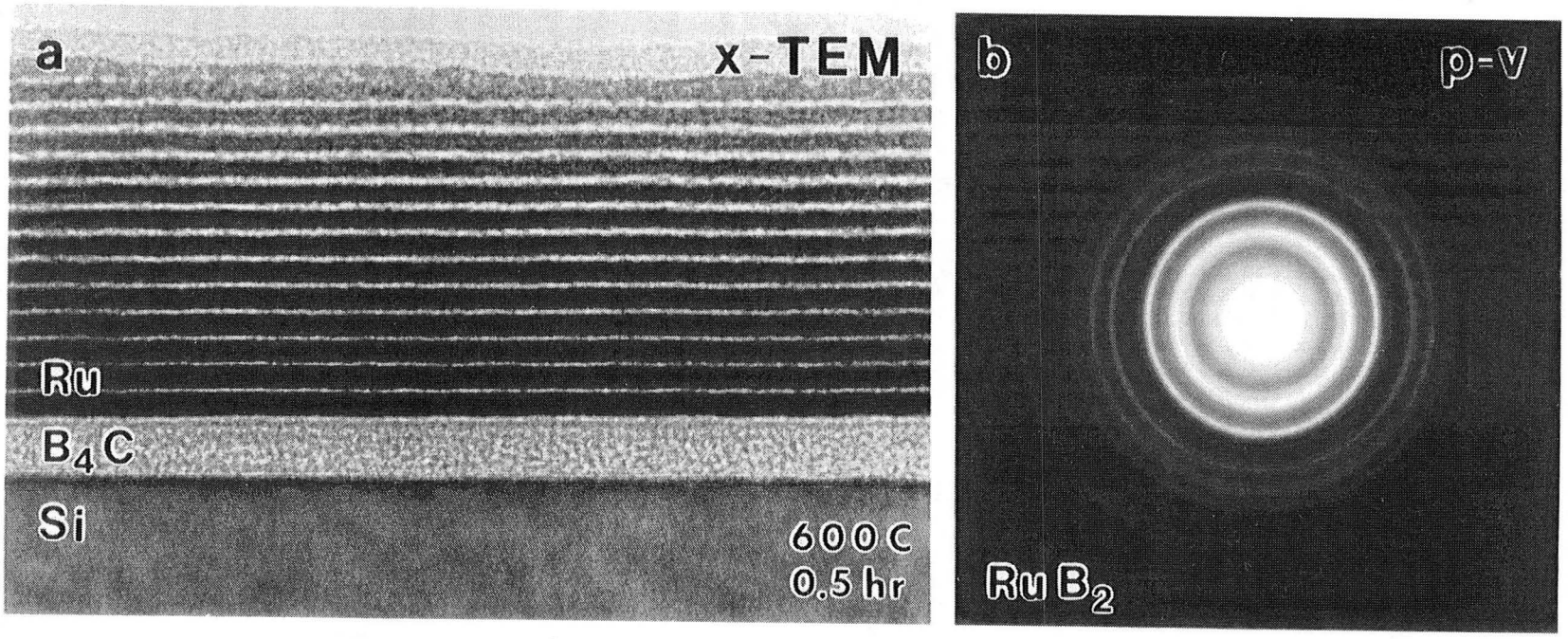

Figure 3-19

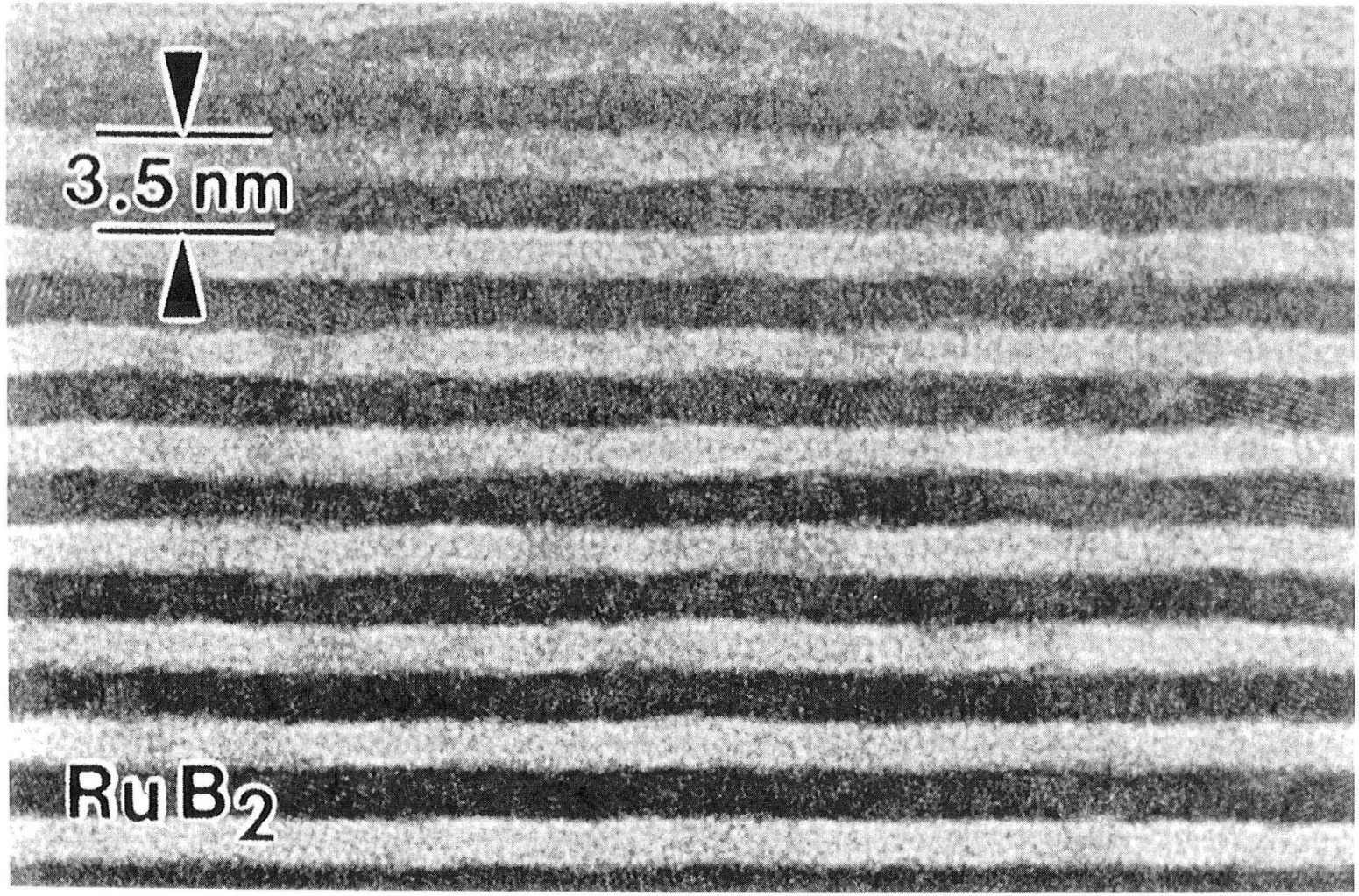

Figure 3-20

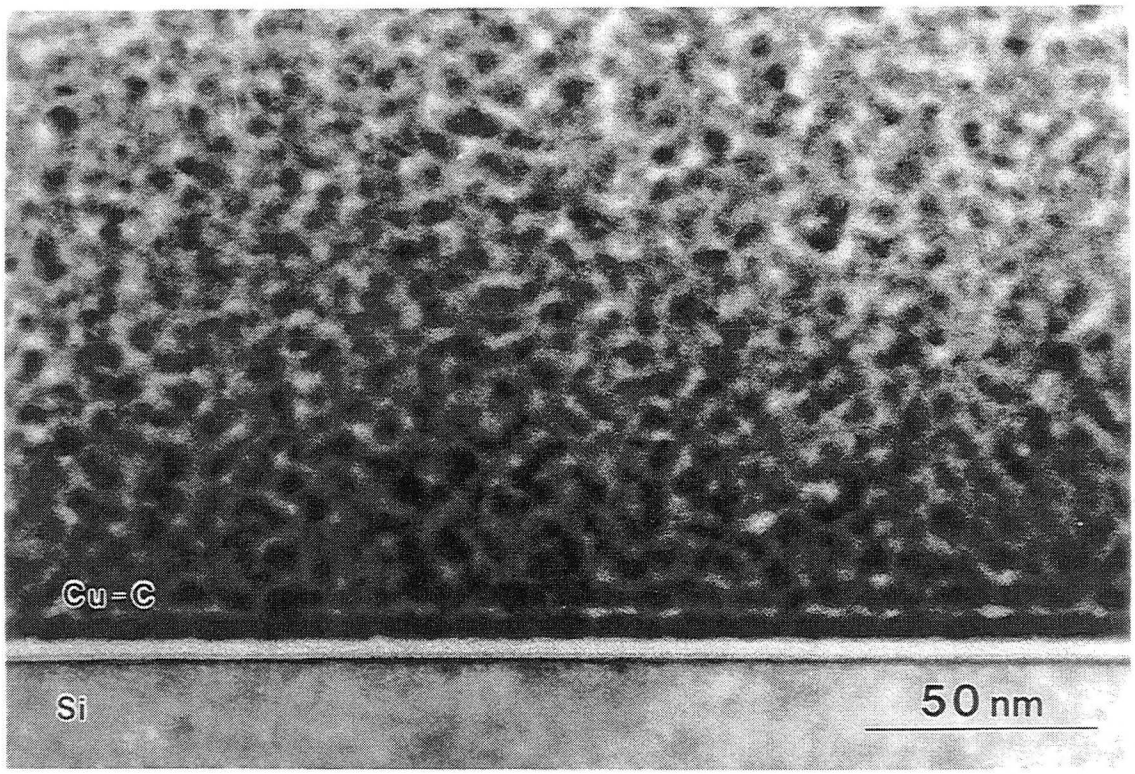

Figure 3-21

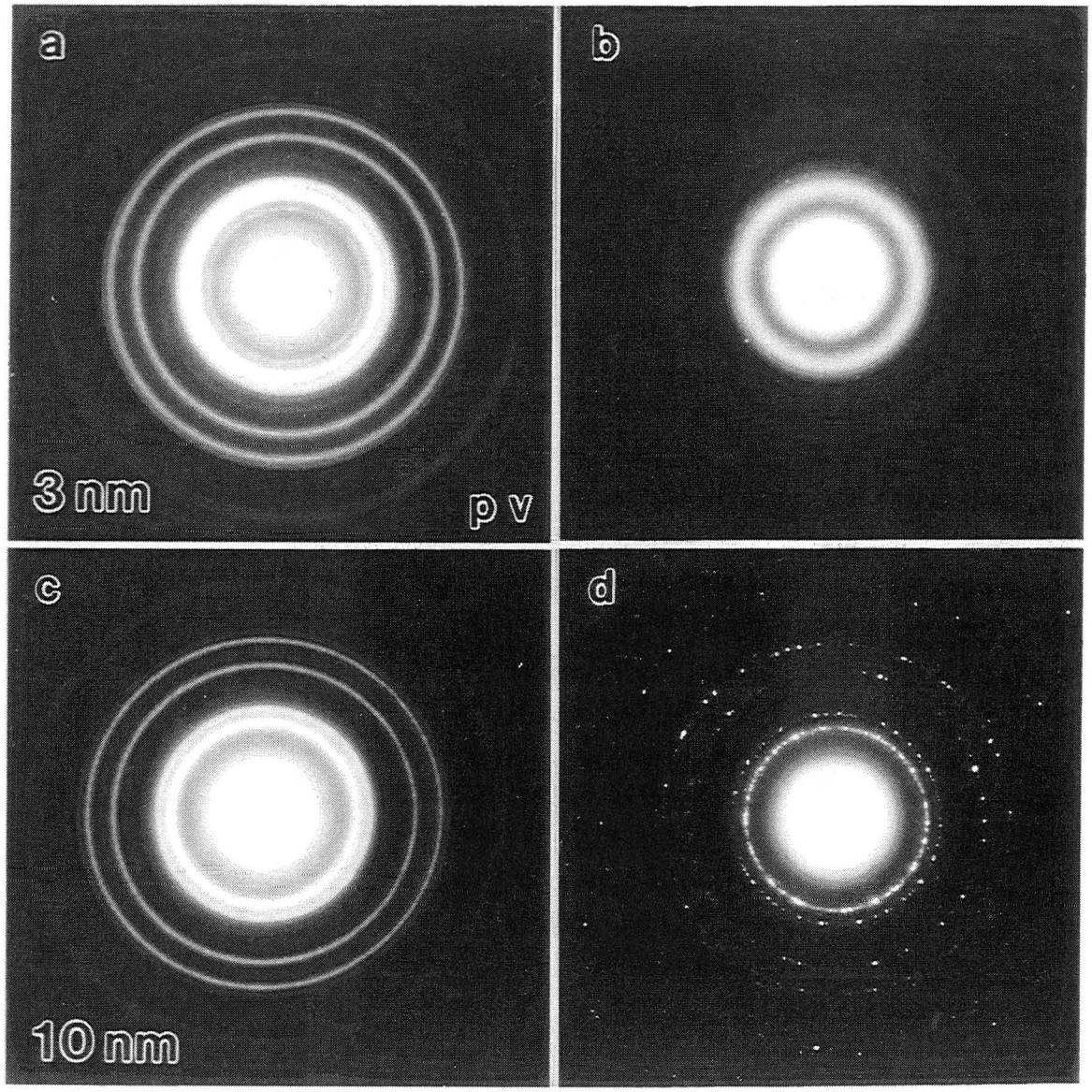

Figure 3-22

CHAPTER 4

DISCUSSION ON MICROSTRUCTURAL AND MORPHOLOGICAL EVOLUTION

The microstructure in as-prepared multilayers, and their behavior upon annealing are related to the thermodynamic and kinetic properties of the materials. In as-prepared multilayers, formation of the phases in the metal-rich layers is discussed in terms of critical nucleation thickness of the crystalline phases, amorphous phase formation, which depends on intermixing and interdiffusion between the materials components during deposition. Reactions between materials components in multilayers upon annealing lead to formation of intermetallic compounds, amorphous phase formation via solid state reactions, and grain growth of elemental phases. The different final structures result from a reduction in the free energy of the systems, and from interdiffusion between the layer materials. Understanding of the mechanisms of these phase transformations is academically stimulating, and may help in the prevention of some undesirable microstructural and morphological changes in these multilayer structures.

4.1 AS-PREPARED MICROSTRUCTURE

The microstructure of the metal layers evolves from amorphous to polycrystalline as the multilayer period increases for all as-prepared metal/C multilayers, while the microstructure of the C layers is amorphous, which is typical for sputtered deposition.

Transition from amorphous to crystalline microstructure in the metal layers, however, occurs at different thicknesses for different materials systems. Formation of the crystalline phase in as-prepared multilayers occurs when the thickness of the "pure" metal layers is greater than the critical nucleation thickness. Intermixing and interdiffusion between the metal and the C produce an amorphous alloy layer at the interfaces during deposition (Figure 4-1), and reduce the thickness of the "pure" metal layers. The metal layers thus are thinner than the nominal thickness. The thickness of the amorphous interfacial layers however depends on the interactions between the materials. Nucleation of a crystalline phase occurs at shorter period in multilayers that exhibit less intermixing and interdiffusion between the layer constituents, which results in thicker "pure" metal layer thickness.

The microstructure of the metal layers thus depends upon the diffusion of the C atoms into the metal layers. There are two sources for C diffusion during deposition: interdiffusion (or intermixing) from kinetic bombardment of energetic atoms from sputtering, and thermal diffusion at the floating temperature of the substrate. The thermal source for diffusion results from transferring of kinetic energy of the bombarded atoms into heat. Thermal diffusion thus occurs subsequently after the atoms have been sputtered onto the substrate.

4.1.1 Conjugate-Component Multilayers

The argument above suggests that conjugate-component multilayers such as Ru/C, which are characterized by a wide immiscible region in the equilibrium phase diagrams, and limited mutual solubility at low temperatures (Figure 4-1),[1] possess thinner interfacial layers than reactive-component multilayers, such as W/C and Cr/C whose phase diagrams contain many intermetallic compounds (Figure 4-2 and 4-3,

respectively).[1] Intermixing from kinetic bombardment of sputtered atoms is assumed to be the same for both types of multilayers. In this picture, the energetic atoms may penetrate into one or two atomic layers of the surface layer until they loose their kinetic energy. The thermal source, however, results in different mechanisms of diffusion for the two systems. The high chemical concentration gradient across the interfaces provides a strong driving force for further interdiffusion. In reactive-component multilayers, high solubility between the constituents allows further intermixing through volume diffusion. Limited solubility in conjugate-component multilayers, on the other hand, promotes interfacial diffusion instead of volume diffusion. The thermal source may also allow the penetrated atoms to diffuse back to the interfaces, which results in thinner intermixed layers.

Observation of the metal crystalline phase in Ru/C multilayers of shorter period than in W/C and Cr/C multilayers can be explained by the model described above. The presence of the intermetallic compounds in the W-C and Cr-C systems suggests that the metals and the C atoms in these systems want to react with each other, while the miscibility gap in the Ru-C system implies that like-atom bonds are preferred to unlike-atom bonds. In other words, the W and Cr atoms prefer to bond to C atoms as they would to their own kind. This is seen in the presence of the amorphous alloy layers at the interfaces in W/C and Cr/C multilayers, which results from intermixing of the metal and the C atoms during deposition. In the case of Ru/C multilayers, on the other hand, interfacial diffusion instead of volume diffusion occurs. Phase separation between the Ru and the C atoms at the interfaces thus reduces the thickness of the interfacial layers in Ru/C multilayers compared to that in W/C and Cr/C multilayers. As a result, for the same nominal period or metal layer thickness, the thickness of the relatively pure Ru layers is thicker than that of the W and Cr layers, and nucleation of a crystalline Ru phase occurs more readily.

4.1.2 Reactive-Component Multilayers

Nucleation of the metal layers in reactive-component multilayers thus depends on interdiffusion, or diffusion of the C atoms into the metal layers. Neglecting surface diffusion, and using Fick's law of non steady-state diffusion,[2] the diffusion length for C from the thermal source is expressed as:

$$x = \sqrt{D \cdot t} \qquad [4\text{-}1]$$

where x is the diffusion length, D is the diffusion coefficient which depends on the temperature, and t is the time of diffusion. The diffusion length of C into the W layers from a thermal source during deposition, at the same temperature, thus is predicted to increase with power of 1/2 of the period thickness. Consider two W layers of different thicknesses, the ratio of diffusion length x_1 / x_2 is proportional to the square root of the ratio of their diffusion time t_1 / t_2, under the same conditions. Since the time for deposition of one layer of the multilayers is linearly proportional to the layer period, then x_1 / x_2 is also proportional to the square root of the ratio of the layer thicknesses d_1 / d_2. Thus for a multilayer of period d_1 that is 3 times of period d_2, for example, the diffusion length x_1 of C into the W layer is only $\sqrt{3}$ or 1.7 times x_2. Applying these numbers to the 4 nm period amorphous W/C multilayer, assuming that the C diffuses completely through the W-rich layer in this sample, or a distance of about 1.6 nm of the W layer thickness, the diffusion length of C in the W-rich layer in the 12 nm period then is approximately only (1.6 nm x 1.7) or 2.7 nm. Since the nominal thickness of the W-rich layer in this sample is 4.8 nm, the "pure" W layer, that can nucleate to form the crystalline phase before deposition of the next C layer, is 2.1 nm. Although this value is a lower limit of the diffusion length, it still illustrates the mechanism for formation of the crystalline structure inside the W-rich layer.

Interdiffusion during deposition in reactive-component multilayers is likely to result from energetic bombardment of the sputtered atoms than from thermal diffusion. Preliminary calculation of the diffusion length x during deposition of one W-rich layer in the 12 nm period W/C multilayer, assuming a maximum substrate deposition temperature of 150°C for the sputtering time of 3 hours, using:

$$D = D_o \cdot e^{-Q/RT} \qquad [4\text{-}2]$$

where D_O is the frequency factor, Q is the activation energy for diffusion, and R and T are the gas constant and the absolute temperature in K, and:

$$D_o = 3.15 \times 10^{-3} cm^2 / sec,$$

$$Q = 172 \text{ Kcal / mole}$$

for the temperature range 100-400°C,[3] yields an insignificant value of the diffusion length of C into W ($x < 10^{-100}$ nm). Thus kinetic-source interdiffusion from atom bombardment, instead of thermal interdiffusion, is probably the dominant process in intermixing of the layers during deposition. The average energies of the atoms reaching the substrate in sputtering processes could be as high as 30 eV.[4] This suggests that the W-rich layers in the short period as-prepared W/C multilayers can contain a high C content, and there is an interfacial layer of intermetallic alloy at each interface in longer period samples. The images of as-prepared 12 nm W/C multilayer in Figure 4-4 indeed do show the presence of interfacial layers, which may be interpreted as intermixing layers resulting from bombardment of energetic atoms onto the existing layers.

The amorphous phases in short period multilayers as well as the crystalline elemental metals in longer period multilayers can be explained by this model. Consider

the moment during which a layer of metal atoms is sputtered onto the surface of a previously deposited C layer. Intermixing and diffusion of the metal and C create an amorphous alloy of a defined thickness for a specific deposition condition at the interfaces. In short period multilayers, this interfacial alloy layer is as thick or almost as thick as the thickness of the metal layers so that an amorphous structure results. In longer period samples, however, this intermixed layer is small compared to the intended thickness of the metal layer so that deposition of subsequent metal atoms results in a relatively pure metal layer. As the period of the multilayers increases, so does the thickness of the metal layers. When the thickness of the pure metal layers in the multilayer is greater than the critical nucleation layer thickness for crystallization, nucleation of a stable crystalline phase occurs at the expense of the decreasing growth rate of the amorphous intermetallic phase. The argument above implies that crystallization of the elemental metal phase in the metal layers in as-prepared samples depends only on the thickness of the metal layers, and is independent of the metal to C layer thickness ratio. Observation of the crystalline W structure in the W layers of the 12 nm period W/C multilayer, or effectively 4.8 nm W layer thickness, is consistent with results of other studies.[5-7]

The model of C atoms sputtered onto a metal layer is similar to that of metal atoms onto a C layer. Intermixing at the surface results in an amorphous interfacial layer that is similar to that below the metal layer. The lighter C atoms however have lower kinetic bombardment energy than the heavier metal atoms, so that they penetrate a shorter distance into the existing metal layer than the metal atoms would into the existing C layer. As a result, the interfacial layers of C on metal layers are usually thinner than those of metal on C layers. The same asymmetry in the interfacial layer thickness in fact has been observed in many other multilayers.[8-9] Intermixing between

the metal and the C thus stabilizes the amorphous structure, which is consistent with the interpretation of Kortright and Denlinger from their results.[5]

It is likely that a high concentration of C is present in the metal layers of reactive -component multilayers after deposition. Once the crystalline metal layer has been formed, however, C atoms from the next deposited layer can diffuse interstitially into the structure, and do not amorphize the already existing crystalline structure. Quantitative analysis of EXAFS studies by Lamble et al. deduced that the coordination number of C neighbors for each W in the W-rich layers is 1 in as-prepared multilayers with 4.3 nm W thick layers, and 0.6 in multilayers with 6.5 nm W thick layers, which indicates a high C content in the W-rich layers.[7] Concentration depth profiles of W/C[10] and Ni/C[11-12] multilayers obtained by sputtered Auger electron spectroscopy (AES) also indicates the presence of C in almost the entire thickness of the 2 nm thick metal layers. The presence of C in the metal layers in as-prepared samples in fact may be necessary for the formation of the carbide phase in the case of long period annealed W/C multilayers. Interdiffusion in a multilayer structure having a steep concentration gradient includes diffusion of both constituents. The relationship between the interdiffusion coefficient and the tracer diffusion coefficients will be discussed in the following section. Diffusion of W in C is assumed to be small compared to that of C in W, and thus C is the dominant diffuser in the structure. This assumption is plausible since the crystalline carbide phase is found in the initial W layers after annealing, which requires diffusion of C into the W layers. Diffusion data for C in W is not available at 500°C, but extrapolation from the values of Q and D_o given earlier yields a diffusion length of only 10^{-38} nm for an annealing condition of 500°C for 4 hours. A carbide phase thus may not have been formed if C atoms were not already present in the W layers.

4.2 THERMAL STABILITY

Stability of multilayers depends on the microstructures and phases which make up the layers, and on the reactions between the layer materials. Although the multilayers may serve different specific purposes in x-ray optics, they all share common materials characteristics of modulated thin film structures. Reactions in thin film multilayers produce different phases in the structures for different multilayer systems. The resultant phases include elemental crystalline phases, intermetallic compounds, and amorphous alloys. Formation of the crystalline compounds, and of the elemental phases can be understood from thermodynamic and kinetic considerations that these microstructures tend to have lower free energy than that of the reactant phases. Formation of an amorphous alloy, CrC, from crystalline Cr and amorphous C structures after annealing, however, is not so intuitively understood. Discussion of the formation of these phases is presented in the following sections. Reactions between layer materials require interdiffusion. In modulated structures having steep concentration gradient such as that in multilayer structures, an interdiffusivity coefficient must be used instead of the conventional tracer diffusivities. Interdiffusivity is especially important in these x-ray multilayer structures since their modulation wavelength is only tens of monolayers thick. The relationship between interdiffusivity in a modulated structure and tracer diffusivities of the materials in the structure in relation to x-ray multilayers is discussed before considering the reactions in these multilayers.

4.2.1 Diffusion in Steep Concentration Gradient Multilayer Structures

Diffusion in a modulated structure having steep concentration gradient is discussed in detail in reference 13. The simple diffusion equation

$$\frac{dc}{dt} = D \cdot \frac{d^2c}{dx^2} \qquad [4\text{-}3]$$

where c is the atom fraction of one of the components, x a spatial coordinate, t time, and D a composition-independent diffusion coefficient, is no longer valid in the presence of steep concentration gradient for many reasons. First, the local free energy of a non-uniform system is dependent not only on the composition at a given point, but also on the spatial derivatives of the composition at that point. Secondly, strain exists in the modulated structure, although its effect is less in an amorphous structure than in crystalline or epitaxial materials. In addition, D is composition dependent. Since the composition of the layers in modulated structures changes constantly as interdiffusion occurs, D also changes significantly. The relationship between the interdiffusivity D^* in a binary system and the tracer diffusivities D_1 and D_2 of the components is given by:[14]

$$D^* = (c_1 d_1 + c_2 d_2) \cdot \frac{1 + d(\ln \gamma_2)}{d(\ln c)}, \qquad [4\text{-}4]$$

where c and γ_2 are, respectively, the concentration and activity coefficient of component 2. If thermodynamic data are available, the temperature dependence of the thermodynamic factor in the second term in the equation can be determined directly. Otherwise, an approximation must be made. In homogenizing systems, however, it was pointed out that this temperature dependent factor is weak and contributes only a few kilocalories per mole to the total activation energy of D^*.[15] In spinodally decomposing systems, this factor is very temperature dependent and its contribution is significant.

In discussion of the reactions in x-ray multilayers in the following sections, it is assumed that the contribution of the temperature dependence of the thermodynamic factor to the interdiffusivity coefficient is negligible. In addition, the tracer diffusivities

of the metals in C are assumed to be very similar to each other, and are assumed to be small compared to that of C in metal so that in comparing among different systems, only the tracer diffusivities of C in metals are considered. This may be a crude approximation, but is valid for comparison among the different systems.

4.2.2 Compound Formation: W/C and Ru/B_4C

Compound formation is observed in two multilayer systems, W/C and Ru/B_4C, after annealing. Although multilayer structures are far from equilibrium, formation of the compounds in these two systems can be predicted from their equilibrium phase diagrams. Figure 4-2 shows the phase diagram of W - C.[1] It shows the presence of two intermetallic compounds, W_2C and WC, which have, respectively, approximately 3 and 6 weight % C. It is then expected that carbide phases are formed in W/C multilayers after annealing. The driving force for compound formation in this system is to lower the free energy of the multilayer system. Consider a unit cell of multilayer structure as outlined in Figure 4-5. The free energy of the unit cell can be crudely decomposed into the bulk free energy terms and the surface, or in this case the interfacial, energy terms. It is expressed as:

$$G_{mult.} = V_m\sigma_m + V_C\sigma_C + A_{int.}(\gamma_{mC} + \gamma_{Cm}), \qquad [4\text{-}5]$$

where V_m and σ_m, and V_C and σ_C are, respectively, the volume and bulk free energy of the metal and C components, A_{int} the interfacial area, and γ_{mC} and γ_{Cm}, respectively, the interfacial energy of the metal on C, and C on metal interfaces, which may in general be different from each other. Although the thicknesses in the multilayers are approaching atomic dimensions that defining actual energy terms may be difficult, this expression is conceptually useful in discussing the free energy of the multilayers. From the expression

above, it can be seen that there are a few mechanisms to reduce the free energy of the system. Since change in the volume contributes a decrease, and change in the interfacial area contributes an increase in the free energy, the free energy can be reduced if the volumes and the area evolve to achieve a low interfacial area to volume ratio. Change in the structure and composition in the bulk and at the interfaces can also reduce the free energy. Reactions between the layers to form a new structure reduces the free energy of the components, such as transformation of the W to carbide phase in the metal layers. A reduction in the free energy from this transformation can be illustrated using the free energy curves of the phases in the W-C phase diagram. Figures 4-6a and 4-6b show the free energy curves of W-C in the temperature range up to 1250°C, and between 1250°C and approximately 2700°C, respectively. In curve 4-6a, the free energy of pure C is assumed to be higher than that of pure W, since C in the multilayers has an amorphous structure. The free energy of the W_2C phase is assumed to be lower than that of the WC phase, as drawn in Figure 6b, since the W_2C phase was observed in the structure after annealing. The formation of the W_2C phase upon annealing is observed only in the longer period W/C multilayers (7 and 12 nm) where a crystalline structure already exists in the as-prepared state. In the short period samples, high C content in the W layers probably stabilizes the amorphous structure upon annealing. The 40% thickness ratio of the metal layer to the multilayer period corresponds to a 14.5 weight % C if the structure were completely homogenized. The C content in the W layers decreases with W layer thickness or multilayer period in as-prepared samples.[7] During annealing, diffusion of the C atoms into the W layers gradually increases the C concentration in the W layers. From the phase diagram and the free energy curves, at the experimental annealing temperature, 500°C, only the carbide phase WC exists at equilibrium, while W_2C does not. The finding of W_2C after annealing results from a reduction in the free energy from the system, and probably from a low C concentration in the W layers that the WC phase is not favorable. The W_2C phase however is not expected to nucleate at

temperatures below 1250°C, according to the phase diagram. It is well known however that thin films do not necessarily have the same behavior as the bulk, and that transformation can occur at a lower temperature and shorter time in thin films than in the bulk. The effects of low-scale dimension on the temperature of reactions can be studied by *in-situ* structural observation and differential scanning calorimetry measurements of various thicknesses of W layers in W/C multilayers. It is also possible that the interfacial energy of W_2C-W interface is significantly lower than that of the WC-W interface that in structures having larger interfacial areas such as in multilayer structures, formation of W_2C is preferred.

Formation of the W_2C phase on annealing appears to depend on both the W layer thickness, and the W to C layer thickness ratio. This is illustrated by comparison among annealing results of this study and other previous studies. Annealing of multilayers having W to C layer thickness ratio of 0.66 with the W layer thickness of 2.8 nm (7 nm period) or greater in this study results in formation of W_2C. Similarly, multilayer having 4 nm W layer thickness and W to C ratio of 4.0 in annealing studies by Takagi et al. resulted in formation also of the same crystalline phase.[6] Lamble et al.,[7] however, prepared a W/C multilayer of W layer thickness 3.7 nm, and W to C ratio of approximately 0.29, and found that the structure remained amorphous after annealing at 350°C for 3 hours, although W_2C was found in their longer W to C ratio annealed samples. Thus a high ratio of W to C layer thickness appears to be required for formation of W_2C on annealing. The 4 nm period multilayer, having 1.6 nm W layer thickness and 0.66 ratio, in this study, however, does not crystallize on annealing. The initial thickness of the W layer hence is also a criterion for W_2C crystallization. High C content in short W layer thickness multilayers, which results from interdiffusion during deposition and annealing, is responsible for the stable amorphous structure after annealing in this case. It is also possible that the thickness of the W layers is less than

the critical thickness for nucleation that the amorphous structure remains. The stability of the amorphous structure in short period metal/C multilayers, as well as in alloy/C multilayers, will be discussed in detail in section 4.2.4.

Compound formation was also observed in Ru/B_4C multilayers after annealing. Formation of the boride instead of a carbide phase in the annealed Ru/B_4C multilayers is not surprising, since the Ru-C phase diagram shows a wide miscibility gap below the eutectic temperature. Thus no carbide phase is observed in the equilibrium phase diagram (Figure 4-1).[1] The Ru-B phase diagram, on the other hand, exhibits various intermetallic compounds at low temperatures, as seen in Figure 4-7.[1] A ternary phase diagram of Ru-C-B is not available, although their respective binary phase diagrams are useful in discussing the annealing results. If C were to be completely homogenized in the Ru layers without the presence of B, the structure would contain a 95 weight % Ru. Similarly, complete homogenization of B alone in Ru layers would correspond to 18 weight % B in the structure. Diffusion of C into the Ru layers is expected to be minimal due to the low solubility of C in Ru at low temperatures, and due to the lack of any carbide phase in the phase diagram. In other words, Ru and C like to be phase separated from each other. Diffusion of B into the Ru layers thus results in the formation of RuB_2, as expected from examination of the phase diagrams. The free energy curves of Ru-B at low temperatures are similar to those of the W-C system shown in Figure 4-2. Nucleation and grain growth of the boride phase results from a reduction in the free energy of the system, as in the W/C system.

4.2.3 Solid State Amorphization Reaction: Cr/C

The Cr-C phase diagram contains many intermediate carbide phases (Fig. 4-3),[1] similar to that of the W-C system. Amorphization in the 10 nm period Cr/C multilayer

upon annealing, instead of formation of a crystalline carbide phase is very different from the W/C system. An amorphous alloy can be produced by at least three different routes: 1) quenching from the high-temperature liquid, 2) codeposition from the vapor, and 3) solid-state reaction. Thermodynamic aspects of amorphous phase formation via these routes have been discussed in details by Saunders et al.[17] In the first route, the metastable phases can appear during rapid quenching because they have substantially lower entropies of fusion than the equilibrium phases.[18-19] Formation of an amorphous phase is possible by codeposition because at low enough temperature, the surface mobility is insufficient so that a single phase amorphous non-equilibrium structure is formed instead of the equilibrium multiphase structure.[20] Calculation of the Gibbs free energies of some metallic systems shows that the amorphous phase is more stable than most competing crystalline phases over a wide range of composition.[17] Therefore if formation of the equilibrium compounds is inhibited, by the composition of the alloy being off stoichiometry or due to low diffusivities inhibiting long-range ordering of the initial randomly distributed atoms, the intrinsic low temperature stability of the amorphous phase enables it to form in preference to other structures.

In the third route, an amorphous phase can be formed from the initial crystalline structures by a solid state amorphization reaction (SSAR). This reaction requires a strong chemical driving force.[21] The essential factors which permit such a reaction are that one of the constituents is a fast diffuser in the other,[21-23] and the existence of a negative heat of mixing in the amorphous alloy. The latter provides the necessary chemical driving force for the reaction. In addition, the temperature at which the reaction occurs must be sufficiently lower than the crystallization temperature of the thermodynamically preferred crystalline intermetallic compounds. SSARs have been observed in many multilayer systems: Au-La,[21] Ni-Zr,[17,24] Co-Zr and Cu-Zr,[17] Fe-Zr,[25] Al-Pt,[26] and Ti-Si.[27] The thermodynamic and kinetic principles of SSAR have also been

discussed regarding metallic systems.[17,28-29] Calculations of free energy diagrams for these systems reveal that the amorphous phase has a lower free energy than the two phase starting materials.[17,21,29-31] Once the amorphous phase nucleates, the reaction rate is limited by the diffusion of the fast diffuser through the growing amorphous layer, as indicated by the dependence of the amorphous layer thickness on the squareroot of time.[29]

In addition to the three routes described above, regions of amorphous phase have also been observed in crystalline samples after being irradiated with high-energy ions.[32-35] Irradiation produces point defects, antisite defects, and regions of local nonstoichiometry. These defects raise the free energy of the structure to the point where the defected crystalline structure has a higher free energy than that of the amorphous structure.[33] When the defects are created from irradiation rapidly enough that overlap occurs, the regions become amorphous. Formation of the amorphous phase from ion irradiation thus depends on the density of defects created during irradiation. Above a certain critical defect concentration, a spontaneous transformation occurs from crystalline to amorphous structures.[34]

Reactions between the crystalline Cr and amorphous C layers during annealing result in the formation of an amorphous phase and the disappearance of the initial Cr crystalline structure. The solid state amorphous phase formation can be explained by the two essential criteria for solid state amorphization reactions: a negative value of the enthalpy of mixing, and the fast diffusion of the constituents. The equilibrium phase diagram shows three carbide compounds, $Cr_{23}C_6$, Cr_7C_3, and Cr_3C_2. Free energy-composition diagrams would show that they have a minimum at the compositions of these compound phases, as seen in Figure 4-8. The common tangent lines between the minima of the crystalline free energy curves give the lowest free energy obtained if the

structure were to decompose into the two corresponding crystalline intermetallic phases. The free energy curve of an amorphous solid solution throughout the composition range suggests that at intermediate compositions between these minima, it is possible that the amorphous structure has a lower free energy than the decomposed crystalline phases.

The second criterion implies that one of the constituents must be able to diffuse into the other rapidly at temperatures below the crystallization temperature of the amorphous alloy. In this case, C is the fast diffuser. This is illustrated in Figure 4-9, which shows the diffusion data of Cr and C, and the crystallization temperature of the alloy. Crystallization temperatures of various equilibrium carbide phases, and some metastable phases are reported to be in the range between 600 and 700°C.[36] The values for the diffusion coefficient, D_o, and the activation energy for diffusion, Q, of C in polycrystalline Cr in the temperature range between 1200 and 1500°C have been reported.[37] They are:

$$D_o = 9 \times 10^{-3}\ cm^2 / sec,$$

and

$$Q = 26.5\ Kcal / mol.$$

The values for Cr-self diffusion in polycrystalline Cr are:

$$D_o = 0.2\ cm^2 / sec,$$

and

$$Q = 73.7\ Kcal / mol,$$

in the temperature range between 1030°C and 1545°C.[38] The diffusion data of C in Cr and of Cr self-diffusion, calculated using these values, indicate that C diffusion is much faster, 4 to 6 orders of magnitude higher, than Cr self-diffusion in the temperature range

shown. Extrapolations of these data to lower temperature provide a comparison of the diffusing species at the annealed temperature, 600°C.

SSAR in modulated structures probably depends on the magnitude of interdiffusion, or a combination of both tracer diffusions, in addition to the fact that one component is a fast diffuser in the other. This is illustrated by comparing the diffusion data of W and C and Cr and C, shown in Figure 4-9. The diffusion data of C in W were calculated using the following parameters:

$$D_o = 8.91 \times 10^{-3}\ cm^2/sec,$$

and

$$Q = 53.5\ Kcal/mol,$$

in the temperature range between 1200°C and 1600°C.[39] For W self-diffusion between 1800°C and 2403°C, they are:[40]

$$D_o = 1.88\ cm^2/sec,$$

and

$$Q = 140.3\ Kcal/mol.$$

Extrapolations of the C and W diffusion data to 500°C, the temperature that crystallization of a carbide phase was found in this experiment, indicate that C in W diffusion is at least 10 orders of magnitude higher than W self-diffusion. Diffusion of C in Cr below the crystallization temperature is also approximately 10 orders of magnitude higher than Cr self-diffusion, which is similar to the comparison in the Au-La system in which SSAR was observed.[21] Diffusion of C in Cr and Au in La, however, is at least 8 to 10 orders of magnitude higher than diffusion of C in W at low temperatures. Slow diffusion of C in W and of W self-diffusion, which leads to slow interdiffusion, hence does not result in SSAR but in recrystallization of an intermetallic compound.

The Cr/C multilayers were prepared such that the thickness of the Cr layers is approximately 40% of the multilayer period. This layer thickness ratio yields a 31.4 weight % C in the structure if it was completely homogenized. In the Cr layers in the layered structure, however, the concentration of C is near zero, and increases as diffusion progresses. It is observed that interdiffusion has occurred in the structure, and diffusion of the C atoms into the Cr layers amorphizes the initial crystalline Cr layers. The change in Cr concentration with annealing time is illustrated in Figure 4-10. At time t_0, the as-deposited multilayer is assumed to have sharp and defined interfaces. Little interdiffusion, shown by the decrease of Cr concentration at the Cr/C boundaries, results from kinetic bombardment during deposition. The thickness of the relatively pure Cr layers in this sample, as compared to that in the 5 nm period sample, is thick enough that nucleation of a crystalline phase is possible. At some later time t_1, interdiffusion and reaction occur at the interfaces, resulting in formation of an amorphous layer at the interfaces and in shorter pure Cr layers. As time increases, the thickness of the amorphous interfacial layers increases, and the thickness of the pure Cr layers decreases to the point where total disorder occurs. The temperature at which the reaction takes place is sufficiently lower than the crystallization temperature, and the fast C diffuser impedes the crystallization of the intermetallic compounds. The multilayer hence becomes amorphous. As the sample is heated to higher temperatures, however, nucleation of a crystalline phase may occur, as observed in other SSAR systems.[24-25]

Solid State Amorphization Reaction (SSAR), similar to that in Cr/C multilayers, has also been observed in other multilayer systems, for example Ti/Si[27] and Mo/Si[9,41] multilayers. SSAR in these multilayers was observed by cross-sectional high resolution TEM. The Si atoms were seen to diffuse into the metal layers and form an amorphous layer at the interfaces. As the temperature increases, the thickness of the amorphized

layers increases. The reactions in these systems occur at lower temperature (~ 300°C) than that of the Cr/C system.

4.2.4 Stability of the Amorphous Phase: WC/C and CrC/C

An amorphous structure has a thermodynamic driving force to transform to a crystalline structure to reduce its free energy. However kinetics does not always allow this transformation to happen. The presence of an amorphous structure in WC/C and CrC/C after annealing can be explained by the high C content in the alloy layers that impedes crystallization of the carbide phases. Assuming that the number of metal atoms and the number of C atoms deposited are equal during sputtering, the atomic ratio of the constituents in the alloy layers is one to one. This assumption corresponds to a 6.5 weight % C in the WC alloy, and a 23 weight % C in the CrC alloy layers. These two compositions fall in between the composition range of a carbide phase, W_2C and Cr_3C_2, and the pure C phase, as can be seen in their phase diagrams. In the case that the amorphous solid solution has a lower free energy in a wide composition range between the crystalline phases, the structure then remains amorphous in order to have the lower free energy. When the free energy curve of the amorphous phase lies above the common tangent line between the carbide and the C, the amorphous structure can reduce its free energy by decomposing into two crystalline phases of the lower free energy tangent line. Decomposition of the amorphous phase requires out-diffusion of the C atoms from the alloys to form a lower C content carbide. Random nucleation of the carbide phase may be possible due to local compositional fluctuations in the layers. Grain growth of the carbides, however, requires an uphill diffusion of the C atoms, since the as-deposited alloy layers are sandwiched between two highly concentrated C layers. Decomposition of the amorphous alloys thus is more difficult, and kinetics may not allow the transformation to occur.

A similar argument can be applied to the case of short period multilayers. Kinetic bombardment and interdiffusion during sputtering create an amorphous alloy of high C concentration at the interfaces. In short period multilayers, the metal layers are thin enough that the thickness of the interfacial layers at the two interfaces of the metal layers may be comparable to the metal layer thickness. The metal layers thus contain a high concentration of C, and hence crystallization of the carbide phases requires uphill diffusion of the C atoms, similar to the multilayers in the WC/C and CrC/C systems. The thickness of the metal layers in short period multilayers however may be less than the critical nucleation thickness required for nucleation.

4.2.5 Phase Separation: Ru/C and Cu/C

4.2.5.1 Agglomeration in Ru/C

The finding of elemental Ru crystallites in annealed Ru/C multilayers is consistent with the prediction that no carbide phase is formed from the phase diagram. For multilayers that exhibit crystalline structure in the as-prepared state, grain growth of the Ru crystallites is observed after annealing. The intriguing feature in this system is that in thin period multilayers where the Ru layers are amorphous in the as-prepared sample, crystallization of elemental Ru crystallites is observed and accompanied by agglomeration of the Ru layers into spherical crystallites. This agglomeration of the Ru layers is discussed in detail in relation to thin film and edge instability in the following sections.

4.2.5.1.1 Instability and Agglomeration

Agglomeration in thin films, or instability of the film surface or interfaces, which subsequently results in cylinderization and spheroidization, has been observed in many thin films and plates. Mechanisms for these processes leading to changes in film morphology have been studied by various groups.[42-65] One model is analogous to the Rayleigh instability in an infinitely long cylinder with isotropic surface energy, and the other model is based on grain boundary grooving of a polycrystalline film.

In the Rayleigh instability of an infinite cylinder, perturbation of the straight cylinder walls drives the structure to a spherical shape in order to reduce the surface area. There are subtle differences in the instability of a cylinder and a thin film or plate. Analysis of instability in a long rod is reviewed before discussing that in a thin plate.

An infinite cylindrical structure with an axisymmetric sinusoidal perturbation in radius possesses two principal radii of curvature: the primary radius of the cylinder r_1, and the secondary radius r_2, whose existence is attendant upon the presence of the perturbation. A schematic of a cylinder with the principal radii, adopted from reference 42, is redrawn in Figure 4-11. Change in r_1 alone induces transport of materials from points of minimum primary radius A to points of maximum primary radius B, promoting an increase in perturbation amplitude. Change in the secondary radius from A to B alone induces materials transport from B to A, opposing growth of the perturbation. As the wavelength λ of the perturbation increases, this opposition decreases because the magnitude of r_2 at both A and B increases with λ, decreasing the curvature difference due to r_2. Beyond a critical λ, there is a net transport of materials from A to B which causes the perturbation to grow. It has been shown that the magnitude of λ_{crit} can be obtained by equating the curvatures at A and B, and balancing

the forces which drive and oppose perturbation growth.[43] The surface area of the cylindrical structure is reduced if λ exceeds the circumference of the cylinder.[44-45] For structures such that the specific surface free energy is isotropic, such as liquids and amorphous structures, this reduction in area implies a reduction in the free energy of the system.[46] A value of wavelength for maximum growth rate of the instability is typically given as $\lambda_{max.} = \sqrt{2} \cdot \lambda_{crit.}$ for surface diffusion dominated process in an isotropic surface energy system.[47] Thermodynamic[46] and kinetic[48] analyses of instability with surface energy anisotropy have also been reported. Kinetic analysis of the perturbation evolution by surface diffusion showed that the ratio of $\lambda_{max.}$ to $\lambda_{crit.}$ is independent of the sign and magnitude of the anisotropy of the free surface energy,[48] and is only valid for infinitesimal perturbations in isotropic analysis. A time dependent study of the behavior of a perturbation of an isotropic surface, assuming surface diffusion, for a periodic wave of small amplitude, by Hackney indicates that no wavelength is stable with respect to perturbation.[49] Wavelength distortions will grow for all wavelengths. The author suggests that perturbation is the result of random "noise" such as temperature variation in spatial variation of the radius associated with the formation of the rod. In summary, the variation of the primary radius of curvature drives perturbation growth, and the variation of the secondary radius opposes the growth.

When applied to thin films having sinusoidal undulation, assuming all surface properties independent of crystal orientation, linear stability analysis predicts that for all wavelengths, all small perturbations decay and a flat film should remain stable.[50-51] Studies of systems with large perturbations (amplitudes of the same order as the film thickness) require nonlinear stability analysis,[52] by which it is found that thin films thus decompose by means of fluctuations only if perturbation is large enough to penetrate the film. Morphological evolution in two dimensional structures by instability have been observed in thin films,[53-56] in isolated thin plates,[42,57] intergranular film,[42] lamellar

structures,[59-62] and crack healing of brittle materials.[63] Evolution of thin films into a collection of agglomerated structures occurs by propagation of an agglomerated edge front by surface diffusion due to edge instability. A schematic diagram of the agglomeration process in thin films is illustrated in Figure 4-12. The process begins with the formation of a ridge and edge recession which either evolves into spheres (edge spheroidization) or leads to formation of fingers and eventual breakup into island chains. Agglomeration via fingering is driven by a reduction in surface areas,[56] and has been observed by TEM in thin films,[53-56] and in intergranular films.[58] By direct observation, Hackney suggested that interface instability resulted during a continuous growth of fingers, without additional nucleation of new fingers.[55] This edge instability progresses when there is a spatial variation in normal edge velocity accompanied by a thickness variation along the edge. Kedia et al. described the formation of fingers from edge instability as a buildup of mass at the tip of lagging intrusions, resulting from diffusion from the tips of the neighboring intrusions, which further reduces the velocity of the lagging intrusions.[56] This allows the neighboring intrusions to grow across the front of the lagging intrusions, resulting in growth of fingers.

Edge spheroidization of a thin film or plate is similar to fingering. This was first suggested by Nichols and Mullins for the spheroidization of single crystal platelets.[47] They deduced that the planar faces of the plate are stable against perturbations, while extensive edge recession causes the ridge to grow in girth, resulting in a doughnut-shaped rim around the perimeter of the plate. This rim has the character of a curve cylinder, which is unstable with respect to undulation along its length and thus would break up into a ring of spheres. Further recession of the film would result in repetition of the sequence, leading to a series of concentric rings of spheres. Edge spheroidization of this type has been observed not on a circular platelet but on the edges of a composite wire.[42]

Another model of agglomeration is based upon the mechanism of grain boundary grooving in polycrystalline thin films,[52,64-65] which predicts that agglomeration in polycrystalline films results from the deepening of the grooves at grain junctions, driven by the equilibrium interfacial energies during grain growth. The triple grain junction is characterized by the equilibrium dihedral angle 2ϕ in the relation $2 \cdot \gamma_s \cdot \cos\phi = \gamma_b$ (shown in Figure 4-13), where γ_s is the surface or interface tension, and γ_b is the grain boundary tension in the film. Mullins showed that the groove deepens as the fourth root of time.[42] Finite groove depth thus is possible depending on the film thickness and grain size of the polycrystalline structure.[52,64-65] In general, agglomeration in polycrystalline films from grain boundary grooving is observed when the crystalline grain size to film thickness ratio reaches a critical value that is greater than one. An analysis based on simple averaging of Fick's first law over the process, and geometrical approximations, such as the curvature differences representing the driving force, and kinetics factors such as the diffusion coefficient, distance and area, suggests that grain boundary grooving is favored when the boundary energy is high, whereas edge spheroidization is the dominant instability mode for plates with large aspect ratios and low internal boundary energies.[57]

4.2.5.1.2 Discussion

The initial Ru films in the 2 nm period Ru/C multilayers are effectively only 3 to 4 atomic layers thick and are amorphous before agglomeration, and thus the multilayer structure here is far from the equilibrium state. The assumed high free energy of the amorphous Ru layers relative to crystalline Ru may provide an additional driving force for crystallization and/or agglomeration which is not considered in the models discussed. In addition, it is difficult to differentiate the bulk from the interfacial properties at this thickness. Simple calculation of the surface areas, assuming uniform

microstructure and equal interfacial energies for amorphous and crystalline structures, indicates that agglomeration occurs more readily in thinner films, and that a spherical morphology is preferred to a flat film when the grain size is larger than the film thickness. This is consistent with the values in the reported models,[52,64-65] and with the measured values from the agglomerated 2 nm Ru/C multilayer. In the proposed mechanisms for agglomeration, the difference between the Rayleigh instability and grain boundary grooving models is that for the Rayleigh instability, the Ru layers agglomerate and crystallize, while the grain boundary grooving mechanism requires a polycrystalline structure, or that the Ru layers crystallize prior to agglomeration. It is not clear whether crystallization or agglomeration occurs first in these Ru films. Grain boundary grooving of the polycrystalline layered films that have crystallized from the initial amorphous state is possible; the equilibrium dihedral angles at the grain junctions however cannot be observed in the images since the crystalline Ru grains appear to be separated by a thick C grain boundary region. Dynamical observation of the microstructure and morphology of the films, and recording of the electron diffraction pattern during heating of the sample in the microscope would help in determining the order of agglomeration and crystallization. Agglomeration of the Ru, and thus destruction of the layered structure, would result in disappearance of the multilayer spots, while crystallization of the Ru crystallites would enhance the Ru polycrystalline rings in the diffraction pattern. The *in-situ* TEM results suggest that diffusion of the Ru and/or C atoms leads to agglomeration of the Ru layers and subsequently to nucleation of the Ru crystallites, though crystallization and grain growth occur before completion of the agglomeration process. Continuous recording by means of video-taping, and *in-situ* high resolution TEM would be helpful in determining more conclusively the mechanism of this agglomeration.[66]

In discussing the mechanism of agglomeration of the Ru layers in Ru/C multilayers in relation to the models described above, it is worthwhile to point out a few important characteristics of multilayers that are different from an isolated film. In a multilayer stack, since the Ru layers are sandwiched between the C layers, agglomeration of the Ru layers requires concurrent diffusion of both Ru and C atoms. Since solubilities of the components in each other are extremely small (0.4 weight % C is soluble in Ru, and solubility of Ru in C is near 0), interfacial diffusion is expected. Since the annealing temperature (500 or 600°C) is very low (less than one third) compared to the eutectic temperature of Ru-C (1940°C), surface or interfacial diffusion is assumed to dominate volume diffusion. Compared to an isolated film, repetition of layers of Ru and C allows cross-layer diffusion from adjacent layers if the interfaces from adjacent layers meet each other and provide a diffusion path for cross-layer diffusion. Consider a sinusoidal perturbation on the interfaces between the layers, as in an instability described earlier. In order for the interfaces to meet, the amplitude of the perturbation R must be greater than half of the multilayer period d ($R > \frac{d}{2}$) if the perturbation from adjacent interfaces occurs at the same point on the x-y plane of the film surface. This is illustrated in Figure 4-14a). On the other extreme, the high limit of R is d ($R > d$) for cross-layer diffusion (Figure 4-14b). Both of the limits result in crystallites that are larger than the initial multilayer period, which is approximately twice the initial Ru layer thickness. Cross-layer diffusion in fact is observed in the agglomerated 2 nm period Ru/C multilayer, resulting in Ru crystallites of approximately 4 nm in diameter or R = 2 nm which is equal to the initial multilayer period. Cross-layer diffusion has also been observed in the 2 nm Ru / 1 nm C and 2 nm Ru / 2 nm C samples that have been annealed at 600°C for 10 hours. Cross-layer diffusion occurs more readily in the shorter period sample (3 nm period) than in the latter sample (4 nm period), which results in larger grains that span the whole multilayer thickness. Physically, the shorter C layers provide shorter diffusion paths for cross-layer diffusion and thus grain growth. The

argument above is consistent with the observation of larger grains for thinner C layer thickness in the plan-view grain size distribution study.

Unlike the case of an infinite rod, perturbation on the surface or interfaces of the film or plate always increases the surface area of the film. The surface area is reduced only when the film has completely agglomerated, e.g. the thin film has transformed into a collection of spheres having radius sufficiently larger than the initial film thickness. Consider a thin film of thickness t, with a square surface of side l. Then the area and volume of the film is:

$$A_o = 2 \cdot l^2 + 4 \cdot l \cdot t, \qquad [4\text{-}6]$$

and

$$V_o = l^2 \cdot t. \qquad [4\text{-}7]$$

Let $l = c \cdot t$, where c is a constant. These values are then:

$$A_o = 2 \cdot c^2 \cdot t^2 + 4 \cdot c \cdot t^2, \qquad [4\text{-}8]$$

and

$$V_o = c^2 \cdot t^3. \qquad [4\text{-}9]$$

Assume that the thin film has transformed into N spheres of the same radius R. The total area and volume of the spheres are then:

$$A = N \cdot 4 \cdot \pi \cdot R^2, \qquad [4\text{-}10]$$

and

$$V = \frac{N \cdot 4 \cdot \pi \cdot R^3}{3}. \qquad [4\text{-}11]$$

Since the mass is conserved before and after transformation, and assume that the change in density is negligible, then the volumes must be equal, or:

$$c^2 \cdot t^3 = \frac{N \cdot 4 \cdot \pi \cdot R^3}{3}, \qquad [4\text{-}12]$$

which gives a value of N:

$$N = \frac{3 \cdot c^2 \cdot t^3}{4 \cdot \pi \cdot R^3}. \qquad [4\text{-}13]$$

For a reduction in the area, then an inequality is obtained:

$$N \cdot 4 \cdot \pi \cdot R^2 < 2 \cdot c^2 \cdot t^2 + 4 \cdot c \cdot t^2, \qquad [4\text{-}14]$$

which yields an expression for a critical radius R_c in terms of c and t:

$$R_c = \frac{3 \cdot c \cdot t}{2 \cdot c + 4}. \qquad [4\text{-}15]$$

For any value of film thickness t, it is observed from the above expression that the ratio of the sphere radius to the initial film thickness R/t is independent of the film thickness itself.

A plot of R_c and R_c/t as a function of $\log(l = c \cdot t)$ for d = 10 Å is shown in Figure 4-15. As l increases, the dimension of the film surface is sufficiently larger than the film thickness. From the plots, it is seen that R_c/t approaches a value of 1.5 for a very thin plate, or for $l >> t$, as in the case of a single Ru layer in the multilayers. It would be interesting to compare this value with results of thin film instability. The size of the spheres however could not be determined from low resolution TEM and SEM images presented in other studies.[53-56]

The analysis above is also valid for a multilayer stack of period d. Consider a unit cell as shown in Figure 4-5. The area and volume of the Ru layer in one unit cell are the same as in the analysis, and thus the value of R_c is given above. For a thin film or plate that the area around the edge of the film is negligible compared to the area on the surface of the film, the second term in the expression for the area of the film is ignored, and a value of $R_c/t = 1.5$ is obtained, which is consistent with the exact solution obtained in the analysis above. When a multilayer of K bilayers is considered, every term in the analysis is multiplied by K, and the expression for R_c is still the same as that of a single film. For a multilayer of any period, the thickness of the Ru layers d_{Ru} is approximately half of the period. For reduction of surface or interfacial area, the diameter of the agglomerated spherical crystallites must be at least twice R_c/t or 3/2 the multilayer period. Cross-layer diffusion hence must occur for reduction of interfacial area. For the case of 2 nm period multilayer, the diameter of the observed agglomerated Ru crystallites is 4 nm, which is larger than the 3/2 of the period. A reduction in the interfacial area and probably in the surface or interfacial free energy thus has occurred. Reduction of surface or interfacial area is not observed in the 3.5 nm period multilayer, however, since the diameter of the crystallites is smaller than 3/2 of the period. For the system to reduce its free energy, other factors must be involved. Grain growth of the Ru crystallites, which reduces the grain boundary area, probably accounts for this free energy reduction.

From the analysis above, multilayers of larger period, and effectively larger Ru layer thickness, require a larger value of R_c for reduction in surface area. Since material transport is required in transformation from thin plate to spheres, larger R_c implies more diffusion or larger perturbation is need for spheroidization to occur. This explains for the difference in the layered stability in the 1 nm Ru / 2 nm C and 2 nm Ru / 1 nm C multilayers upon annealing. The first sample agglomerates upon annealing, while the

latter remains layered. The driving force for agglomeration is reduction in the surface or interfacial area. The thinner Ru layers require a smaller R_c, which results in agglomeration of the Ru layers. The amorphous structure in this sample probably provides additional driving force for agglomeration through crystallization. Thicker films thus are more stable (less susceptible) to agglomeration than thinner ones.

Following the analysis above, the surface or interfacial area for a specific sphere radius R can be calculated. An expression for the ratio of the new area to the area of the thin film in terms of R can be obtained:

$$\frac{A}{A_o} = \frac{3 \cdot c \cdot t}{(2 \cdot c + 4)R}. \qquad [4\text{-}16]$$

Again, A/A_o is independent of K bilayers in a multilayer. The plot of A/A_o as a function of R/t is shown in Figure 4-16. It is found that this plot is almost identical to each other for $c > 100$. As can be seen from the plot, a reduction of area is obtained when R/d is greater than 1.5. Assume that these particles are single grain crystallites, then the rate of grain growth or particle growth, which is accompanied by a reduction in the surface area, is proportional to the curve in Figure 16. Grain growth thus is most rapid at the beginning of the process, or when the particles are small, which is consistent with diffusion required for further grain growth.

Crystallization and grain growth of Ru crystallites play an important role in agglomeration of the Ru layers in Ru/C multilayers. The Ru layers agglomerate, as opposed to the C layers, probably because crystallization and grain growth of Ru crystallites that accompany agglomeration reduces further the free energy of the system. A system of Ru spherical crystallites dispersed in an amorphous C matrix probably has

a lower free energy than that of spherical amorphous C particles dispersed in a randomly distributed Ru matrix.

It is unclear if edge spheroidization or perturbation on the film surface can describe the agglomeration. The ex-situ sample as heated is typically more than 2 cm in length. The area of the surface of the films in the multilayers is in the order of 10^{16} Å^2. The *in-situ* sample is a wedge shaped TEM specimen, as described in chapter 2, having a thickness variation perpendicular to the film or layer surface. Near the thinner edge of the specimen, the sample could be as thin as a few hundreds of angstroms. The surface area of the films or layers in the in-situ TEM sample thus may only be in dimension of $10^2 \times 10^6$ or equal to 10^8 Å^2 in certain places when heated. In some instances during in-situ TEM observation, it was observed that the layers at the thinner area of the wedge-shaped specimen agglomerated before those at thicker area. It is inconclusive, however, if spheroidization occurs at the edge of the layers as described earlier. The difference in the surface area and shape of the layers may result in different mechanisms for agglomeration.[42]

4.2.5.2 Immiscibility in Ru-C and W_2C-C

Predictions of agglomeration in multilayers can not naively be based solely on the presence of the miscibility gap in the equilibrium phase diagram of the layer materials. Many important thermodynamic and kinetic factors are involved in determining this morphological change upon annealing. Consider the case of the annealed W/C multilayers. Short period (2 and 4 nm) samples remain amorphous, while longer period (7 and 12 nm) samples recrystallize to form crystalline W_2C in the initial W layers. The W-C phase diagram shown in Figure 4-2 indicates that W_2C and C are immiscible in the temperature range between 1250°C and the eutectic temperature. In contrary to

agglomeration observed in short period Ru/C multilayers after annealing, the annealed W/C (or W_2C/C) multilayers remain layered. There are a few thermodynamic and kinetic differences in the two systems that may explain for the different morphological evolution under thermal activation. Immiscibility implies that decomposition into the two equilibrium phases assures the lowest free energy given by the common tangent between the phases. In the Ru-C case, phase separation between elemental Ru and C atoms suggests that the bond energy between unlike-atoms are significantly higher than that of like-atoms. In the case of W_2C-C, however, the C atoms can bond to either C or W atoms. High solubility of both W and C in this system allows a high content of C in the initial W layers. From the argument above, it can be assumed that the interfacial energy of Ru-C is significantly higher than that of W_2C-C or W-C that provides an additional driving force for agglomeration in the Ru/C to occur.

Multilayers are usually far from an equilibrium state, and thus their free energy is not at a minimum. Consider again the free energy of a multilayer unit cell in equation 4-5. The system can reduce its energy by reducing the surface or interfacial terms, or the interface to volume ratio. Agglomeration is observed in short period (2 and 3.5 nm) Ru/C multilayers, while formation of the crystalline W_2C phase is only observed in multilayers with period > 7 nm. The Ru/C samples thus have a larger interfacial area, or higher interface to volume ratio, than W/C samples. Agglomeration in the Ru/C samples results from a strong driving force to reduce this high ratio.

Kinetic factors are also important in the differences of the morphological evolution between the two systems. The eutectic temperature of Ru-C is 1940°C, while that of W_2C-C is greater than 2780°C. Diffusion in the W-C system is probably much slower than that in the Ru-C system at the same annealing condition for both systems in this study. Mechanisms of diffusion in the two systems, however, are different from

each other, based on their thermodynamic properties. As discussed earlier in this chapter, limited solubility in the Ru-C system does not allow volume diffusion between the layers. Interfacial diffusion thus dominates, which leads to morphological fluctuation of the interfaces and subsequent agglomeration of the layers. Volume diffusion is possible in the W/C multilayers due to high solubility in the W-C system, which seems to stabilize the flat interfaces or the layered structure in this system.

The problem of multilayer instability against agglomeration or morphological instability is quite complex. Many thermodynamic and kinetic factors must be considered in predicting if agglomeration were to occur. Some simple experiments such as annealing of W/C multilayers at higher temperatures, and comparisons between W/C and Ru/C multilayers of the same period annealed at comparable temperatures according to their respective eutectic temperatures, may provide a better understanding of the criteria for agglomeration.

4.2.5.3 Clustering in Cu/C

The Cu/C system has an equilibrium phase diagram similar to that of the Ru/C system. It is thus not surprising that grain growth of the elemental FCC Cu phase is found in the longer period Cu/C multilayers after annealing. Amorphization of the crystalline phase in the short period sample may be somewhat surprising under thermodynamic consideration, since annealing typically drives a system to a lower energy crystalline structure. Amorphization in this sample however may result from a solid state amorphization reaction, during which the equilibrium amorphous state seeks a lower energy than that of the crystalline structure. SSAR is highly unlikely in this case however since C is not highly soluble in Cu. It is possible that the Cu clusters in the as-prepared sample may be at or below the critical nuclear radius for the grains to grow,

and since the as-deposited structure is in a metastable state, amorphization instead of grain growth of the Cu crystallites occurs. It is unclear from current data if SSAR or classical nucleation theory applies to this case. Free energy calculation of the amorphous and crystalline structure in the system, or further annealing of the structure, is required to determine the mechanism of this amorphization. If further annealing still results in an amorphous structure, then SSAR probably occurs. If a crystalline structure is observed upon further annealing, then a critical nuclear radius, or a critical Cu layer thickness, between 2 and 4 nm, is required for grain growth to occur.

4.3 REFERENCES:

1. M. Hansen and K. Anderko, in Constitution of Binary Alloys, 2nd ed. (1989).
2. D.A. Porter and K.E. Easterling, *Phase Transformations in Metals and Alloys* (Van Nostrand Reinhold, 1988).
3. *Diffusion Data* **2**, 2 (1968) 156.
4. W.D. Westwood, MRS Bulletin **XIII**, 12 (1988) 46.
5. J.B. Kortright and J.D. Denlinger, in *Multilayers: Synthesis, Properties and Non-Electronic Applications*, T.W. Barbee, Jr., F. Spaepen, and L. Greer, eds. (MRS Proc. **103**, Pittsburgh, PA 1988) 95.
6. Y. Takagi, S.A. Flessa, K.L. Hart, D.A. Pawlik, A.M. Kaden, J.L. Wood, J.E. Keem, J.E. Tyler, in *Applications of Thin-Film Multilayered Structures to Figured X-Ray Optics*, edited by G.F. Marshall (Proc. SPIE **563**, Bellingham, WA 1985) 66.
7. G.M. Lamble, S.M. Heald, D.E. Sayers, E. Ziegler, and P.J. Viccaro, J. Appl. Phys. **65**, 4250 (1989).
8. A.K. Petford-Long, M.b. Stearns, C.-H. Chang, S.R. Nutt, D.G. Stearns, N.M. Ceglio, and A.M. Hawryluk, J. Appl. Phys. **61** (1987) 1422.
9. K. Holloway, K.B. Do, and R. Sinclair, in *Multilayers: Synthesis, Properties and Non-Electronic Applications* (MRS Proc. **103**, 1988) 167.
10. K. Murakami, H. Nakamura, T. Oshino, and H. Nikaido, in Soft X-ray Projection Lithography, J. Bokor, ed. (OSA Proc. **12**, 1991) 101.
11. Ph. Houdy, Mater. Sci. Forum 59&60 (1990) 581.

12. P. Boher, Ph. Houdy, R. Barchewitz, J.C. Joud, and L.J. Van Ijzendoorn, 12 IXCOM Conference Cracovie (1989).
13. A.L. Greer and F. Spaepen, in Synthetic Modulated Structures, L.L. Chang and B.C. Giessen, eds. (Academic Press, Inc., 1985) 419.
14. L.S. Darken, Trans. AIME 175 (1948) 184.
15. J.E. Hilliard, Acta Metall 5 (1957) 29.
17. N. Saunders and A.P. Miodownik, J. Mater. Res. **1**, 1 (1986) 38.
18. N. Saunders, A.P. Miodownik, and L.E. Tanner, in *Rapidly Quenched Metals V* (North-Holland, Amsterdam, 1985) 191.
19. U. Kambli, M. Von Allmen, N. Saunders, and A.P. Miodownik, Appl. Phys. **A36** (1985) 189.
20. N. Saunders and A.P. Miodownik, CALPHAD J. **9**, 3 (1985) 283.
21. R.B. Schwarz and W.L. Johnson, Phys. Rev. Lett. **51**, 5 (1983) 415.
22. H. Schroder and K. Samwer, Phys. Rev. Lett. **54** (1985) 197.
23. Y.-T. Cheng, W.L. Johnson, and M.-A. Nicolet, Appl. Phys. Lett. **47** (1985) 800.
24. P. Ehrhart, R.S. Averback, H. Hahn, S. Yadavalli, and C.P. Flynn, J. Mater. Res. **3**, 6 (1988) 1276.
25. B.M. Clemens and D.L. Williamson, in *Multilayers: Synthesis, Properties and Non-Electronic Applications* (MRS Proc. **103**, 1988) 159.
26. J.M. Legresy, B. Blanpain, and J.W. Mayer, J. Mater. Res. **3**, 5 (1988) 884.
27. K. Holloway and R. Sinclair, J. Appl. Phys. **61**, 4 (1987) 1359.
28. see A.R. Yavari, and P.J. Desre, ed., *Multilayer Amorphisation by Solid-State-reaction and Mechanical Alloying* (Colloque de Physique **C4**, 51, 1990).
29. W.L. Johnson, Prog. Mater. Sci. **30** (1986) 81.
30. B.M. Clemens and M.J. Suchoski, Appl. Phys. Lett. **47** (1985) 943.
31. B.M. Clemens, Phys. Rev. **B33**, 11 (1986) 7615.
32. J. Eridon, G.S. Was, and L. Rehn, J. Mater. Res. **3**, 4 (1988) 626.
33. M.L. Swanson, J.R. Parsons, and C.W. Hoelke, Radiat. Eff. **9** (1971) 249.
34. J.L. Brimhall, H.E. Kissinger, and L.A. Charlot, Radiat. Eff. **77** (1983) 237.
35. L.S. Hung, M. Nastisi, J. Gyulai, and J.W. Mayer, Appl. Phys. Lett. **42**, 6 (1983) 672.
36. E. Bouzy, G. le Caer, and E. Bauer-Grosse, Mat. Sci. Eng. **A133** (1991) 640.
37. E.V. Borisov, P.L. Gruzin, and S.V. Zemskii, Zashch. Pokryt. Metal. 2 (1968) 104.
38. J. Askill and D.H. Tomlin, Phil. Mag. **11**, 111 (1965) 467.
39. A.Y. Nakonechnikov, L.V. Pavlinov, and V.N. Bikov, Fiz. Metal i Metalloved 22 (1966) 234.
40. R.E. Pawel and T.S. Lundy, Acta Met **17**, 8 (1969) 979.

41. Y. Cheng, M.B. Stearns, and D.J. Smith, presented at Physics of X-Ray Multilayer Structures (OSA Meeting, 1992).
42. J.C. Malzahn Kampe, T.H. Courtney, and Y. Leng, Acta Metall **37**, 7 (1989) 1735.
43. T.H. Courtney, in *New Developments and Applications in Composites*, D. Kuhimann-Wilsdorf and W.C. Harrigan, Jr., eds., TMS-AIME (1979) 1.
44. Lord Rayleigh, Lond. Math. Soc. Proc. 10 (1879) 4.
45. S. Chandrasekhar, *Hydrodynamic and Hydromagnetic Stability*, Oxford Clarendon Press, Chapter XII (1961).
46. J.W. Cahn, Scripta Metall. 13 (1979) 1069.
47. F.A. Nichols and W.W. Mullins, Trans. AIME 233 (1965) 1840.
48. J.S. Stolken and A.M. Glaeser, Scripta Metall. et Mater. 27 (1992) 449.
49. S. A. Hackney, Scripta Mettal. et Mater. 25 (1991) 799.
50. W.W. Mullins, J. Appl. Phys. 28 (1957) 333.
51. W.W. Mullins, J. Appl. Phys. **30**, 1 (1959) 77.
52. D.J. Srolovitz and S.A. Safran, J. Appl. Phys. **60**, 1 (1986) 247.
53. E. Jiran and C.V. Thompson, J. Elec. Mat. **19**, 11 (1990) 1153.
54. E. Jiran and C.V. Thompson, Thin Solid Films 208 (1992) 23.
55. S.A. Hackney, Scripta Metall. et Mater. 26 (1992) 1125.
56. R.S. Kedia, T.M. Lillo, Q. Horn, M.R. Plichta, and S.A. Hackney, Scripta Metall. et Mater. 28 (1993) 269.
57. T.H. Courtney and J.C. Malzahn Kampe, Acta Metall. **37**, 7 (1989) 1747.
58. F.F. Lange and D.R. Clarke, J. Am. Ceram. Soc. **65**, 10 (1982) 502.
59. L.D. Graham and R.W. Kraft, Trans. TMS-AIME 236 (1966) 94.
60. J.D. Livingston and J.W. Cahn, Acta Metall. 22 (1974) 495.
61. S.P. Gupta, Acta Metall. 34 (1986) 1279.
62. Y.L. Tian and R.W. Kraft, Metall. Trans. 18A (1987) 1359.
63. J. Rodel and A.M. Glaeser, J. Am. Ceram. Soc. **73**, 3 (1990) 592.
64. K.T. Miller, F.F. Lange, and D.B. Marshall, J. Mater. Res. **5**, 1 (1990) 151.
65. T. Nolan, R. Sinclair, and R. Beyers, J. Appl. Phys. **71**, 2 (1992) 720.
66. T.D.Nguyen, R. Gronsky, and J.B. Kortright, Proc. EMSA (1992).

4.4 FIGURES

Figure 4-1. Equilibrium phase diagram of Ru-C (from ref. 1).

Figure 4-2. Equilibrium phase diagram of W-C, showing the intermetallic compounds (from ref. 1).

Figure 4-3. Equilibrium phase diagram of Cr-C, showing the intermetallic compounds (from ref. 1).

Figure 4-4. Cross-sectional high resolution TEM images of as-prepared 12 nm W/C multilayers, showing the amorphous layers at the interfaces.

Figure 4-5. A unit cell in a multilayer structure of period d.

Figure 4-6. Free energy curves of W-C in the temperature range a) up to 1250°C, and b) between 1250 and approximately 2700°C, according to the equilibrium phase diagram.

Figure 4-7. Equilibrium phase diagram of Ru-B, showing the intermetallic compounds (from ref. 16).

Figure 4-8. Free energy curves of Cr-C at 600°C showing the possible wide range of composition where the amorphous phase has lower free energy than the crystalline intermetallic compound and amorphous C phases.

Figure 4-9. Diffusion data of C in Cr, Cr self-diffusion, C in W, and W self-diffusion as a function of reciprocal temperature. T_x(CrC) is the range of crystallization temperatures for Cr carbide phases (ref. 36).

Figure 4-10. Concentration profiles of Cr and C in Cr/C multilayers during annealing at $t_2 > t_1 > t_o$.

Figure 4-11. A schematic of an infinite cylinder with a longitudinal perturbation in radius, which possesses two principal radii of curvature, primary r_1 and secondary r_2 (adopted from ref. 42)

Figure 4-12. Schematic showing the process of edge spheroidization.

Figure 4-13. Grain boundary grooving at a grain junction in a polycrystalline thin film resulting in the dihedral angle.

Figure 4-14. Process of cross-layer diffusion in the case a) $R > d$, and b) $R > 2d$.

Figure 4-15. Plots of R_c and R_c/d vs. log(l) for d = 10 Å. R_c/d approaches 1.5 for reduction of the surface area.

Figure 4-16. Plot of reduction in surface area vs. R/d for d = 10 Å. Notice that A/A_o is 1 when R/d = 1.5.

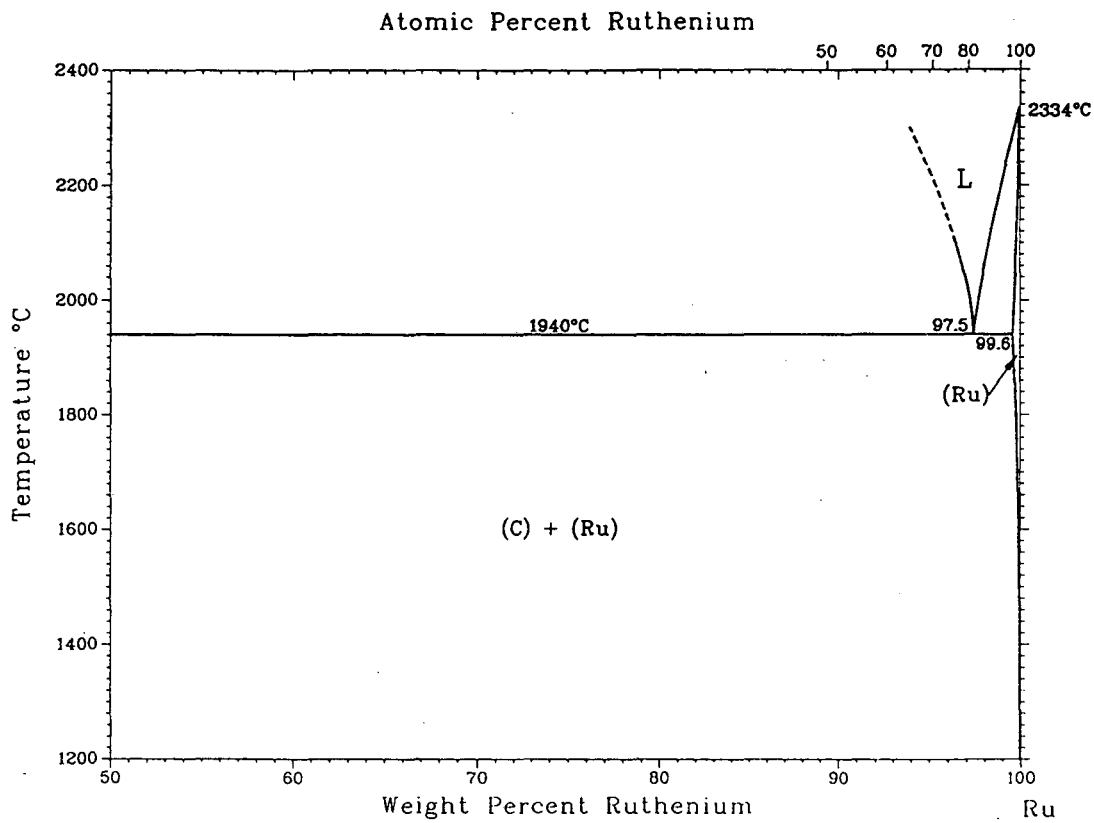
Atomic Percent Ruthenium
50
60
70
80
100
2400
2200
2000
1800
1600
1400
1200
Temperature °C
2334°C
L
1940°C
97.5
99.6
(Ru)
(C) + (Ru)
50
60
70
80
90
100
Weight Percent Ruthenium
Ru

Figure 4-1

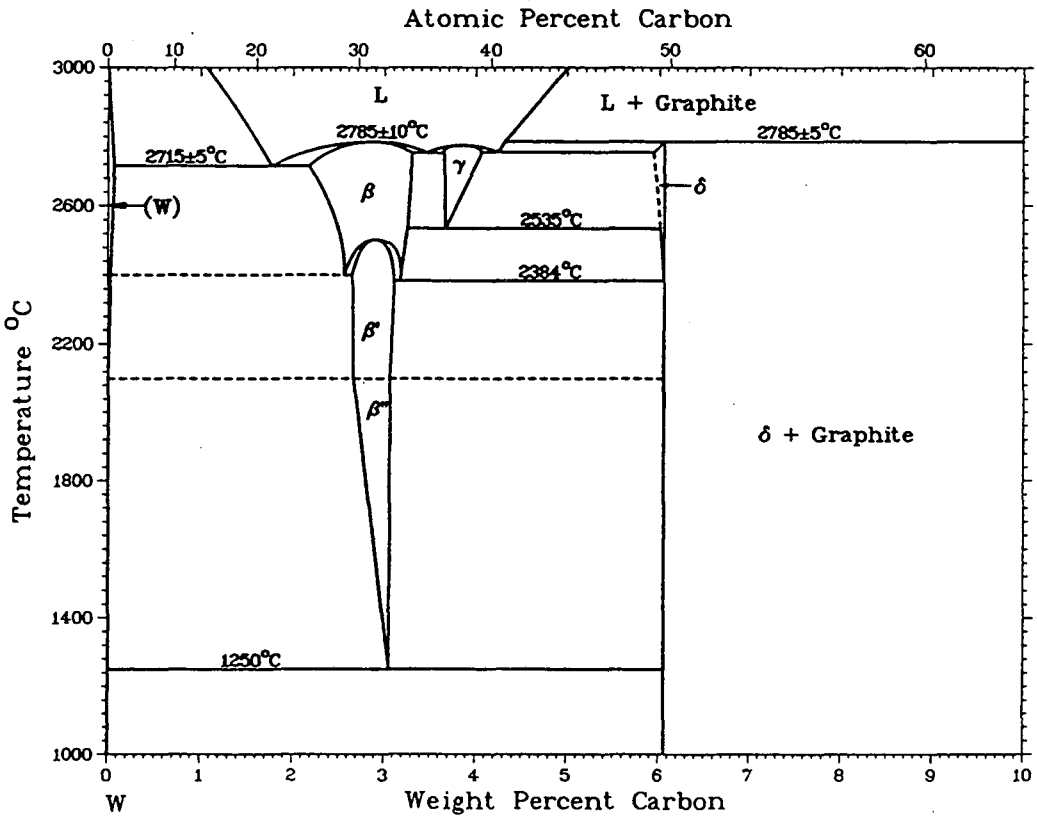
Atomic Percent Carbon
0
10
20
30
40
50
60
3000
2600
2200
1800
1400
1000
Temperature °C
L
L + Graphite
2785±10°C
2785±5°C
2715±5°C
γ
β
δ
(W)
2535°C
2384°C
β'
β''
δ + Graphite
1250°C
0
1
2
3
4
5
6
7
8
9
10
W
Weight Percent Carbon

Figure 4-2

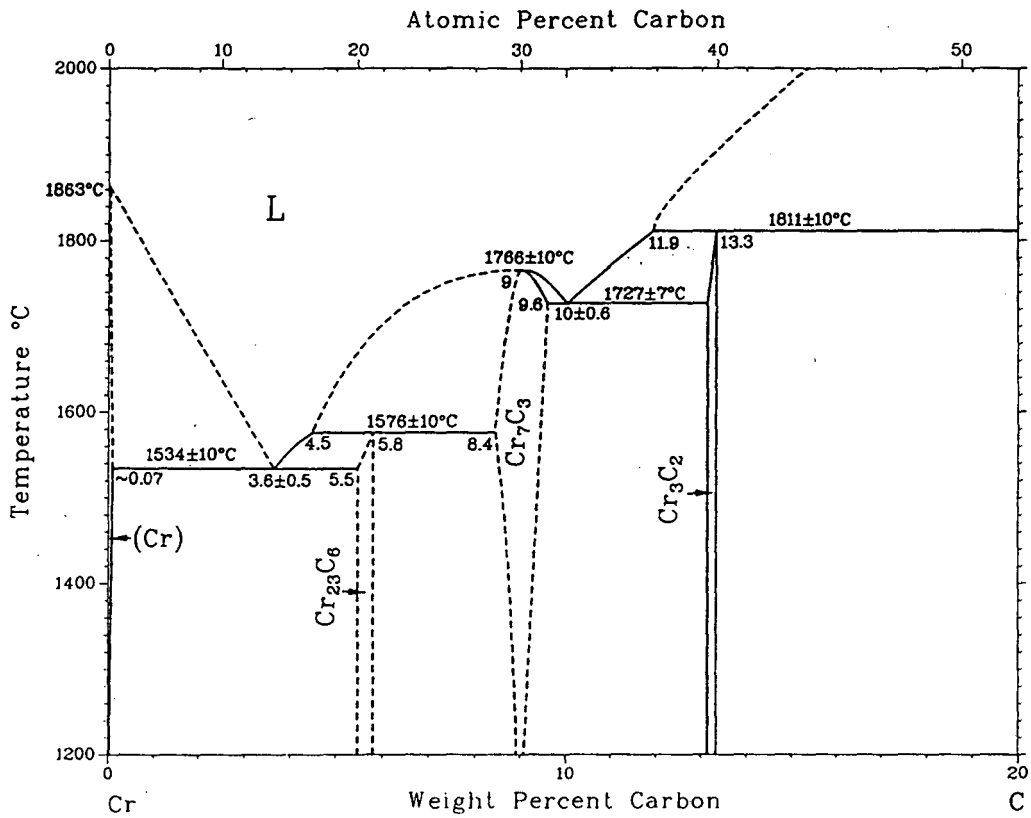
Atomic Percent Carbon
0
10
20
30
40
50
2000
1800
1600
1400
1200
Temperature °C
1863°C
L
1811±10°C
11.9
13.3
1766±10°C
9
9.6
10±0.6
1727±7°C
1576±10°C
4.5
5.8
8.4
1534±10°C
~0.07
3.6±0.5
5.5
(Cr)
$Cr_{23}C_6$
Cr_7C_3
Cr_3C_2
0
10
20
Cr
Weight Percent Carbon
C

Figure 4-3

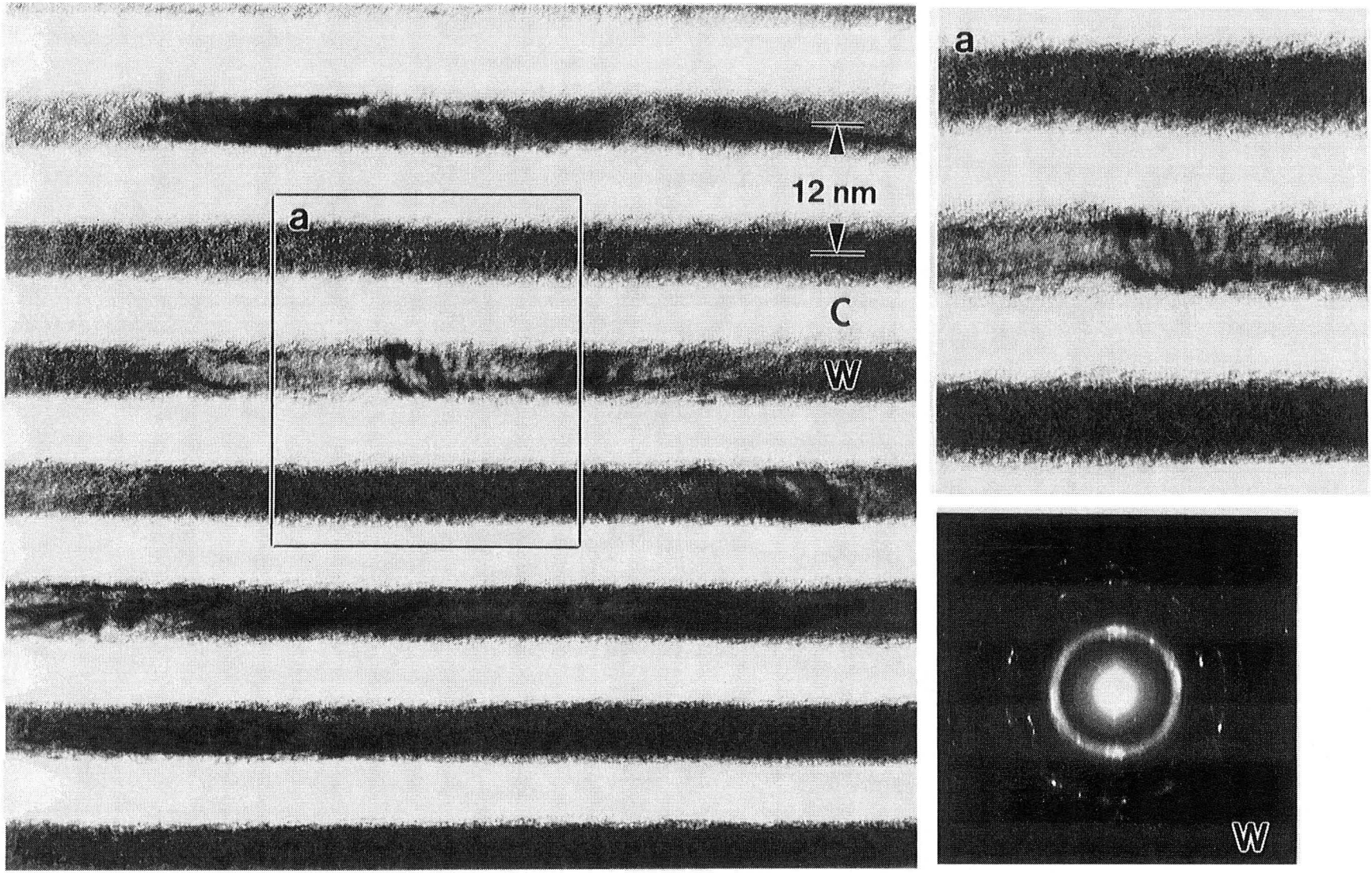

Figure 4-4

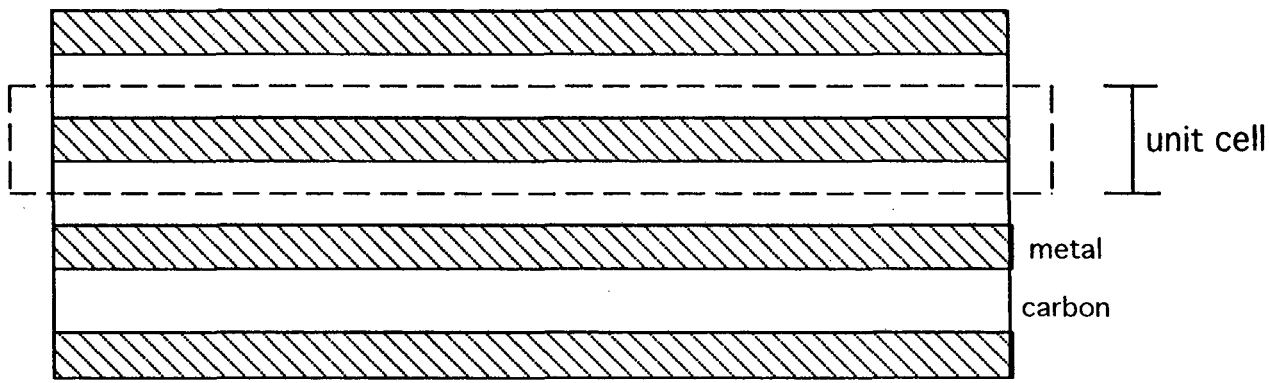

Figure 4-5

a) T < 1250°C

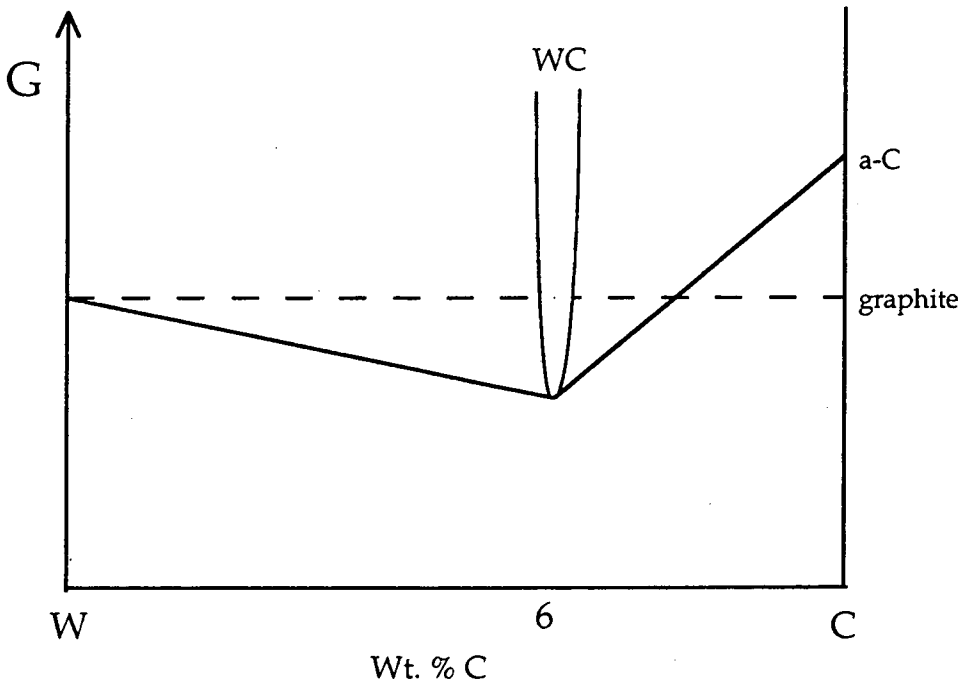

b) 1250°C < T < 2700°C

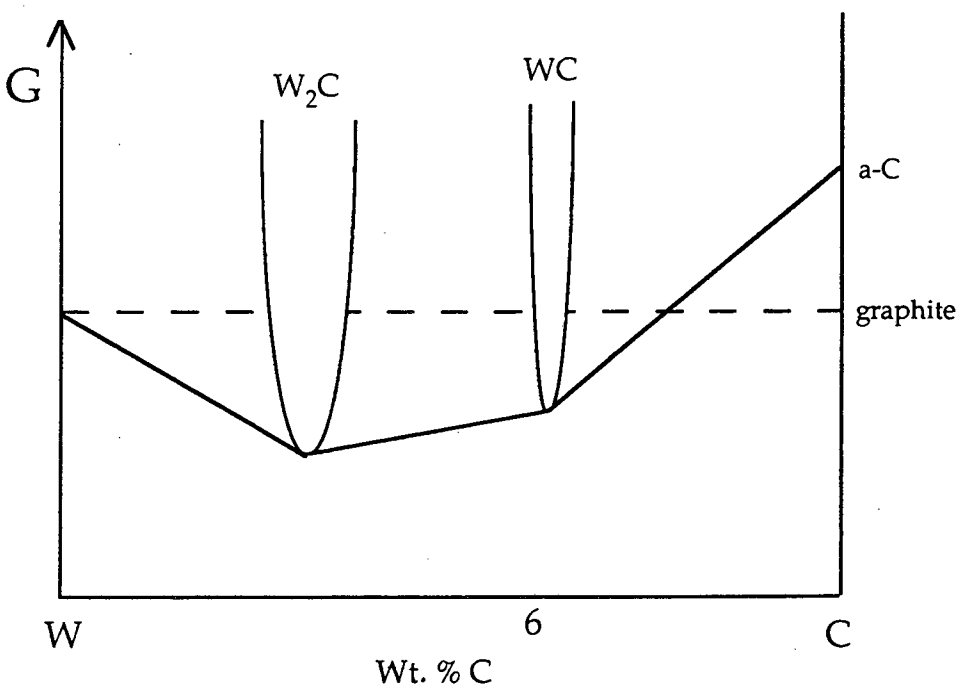

Figure 4-6

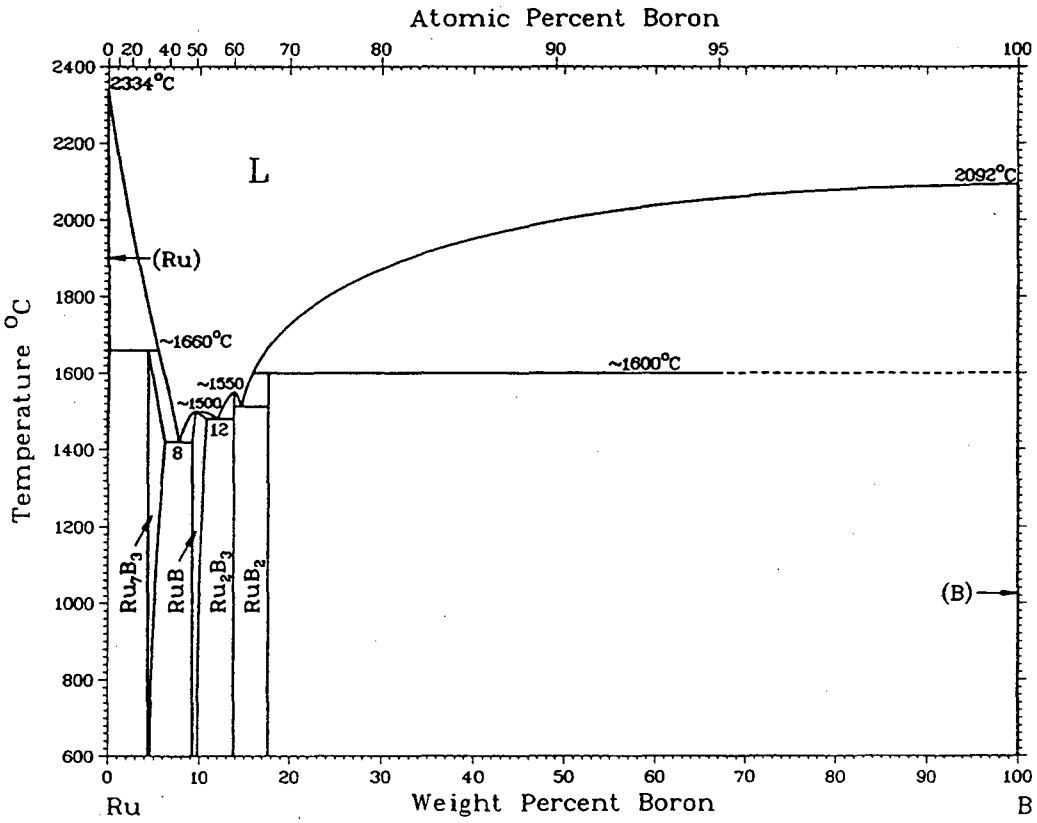
Atomic Percent Boron
0 20 40 50 60 70 80 90 95 100
2400
2334°C
2200
L
2092°C
2000
(Ru)
1800
~1660°C
~1600°C
~1550
~1500
1600
12
8
1400
1200
Ru7B3
RuB
Ru2B3
RuB2
(B)
1000
800
600
Temperature °C
0 10 20 30 40 50 60 70 80 90 100
Ru
Weight Percent Boron
B

Figure 4-7

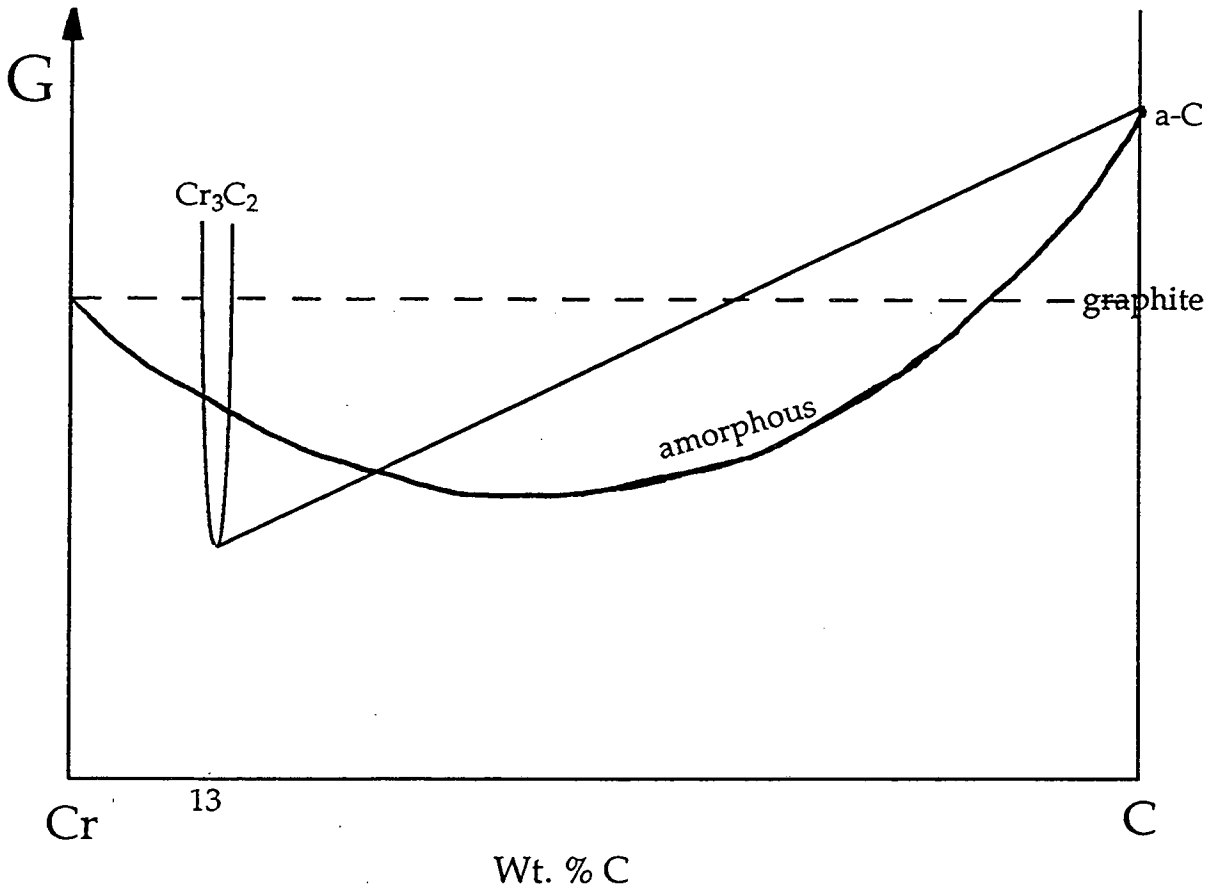

Figure 4-8

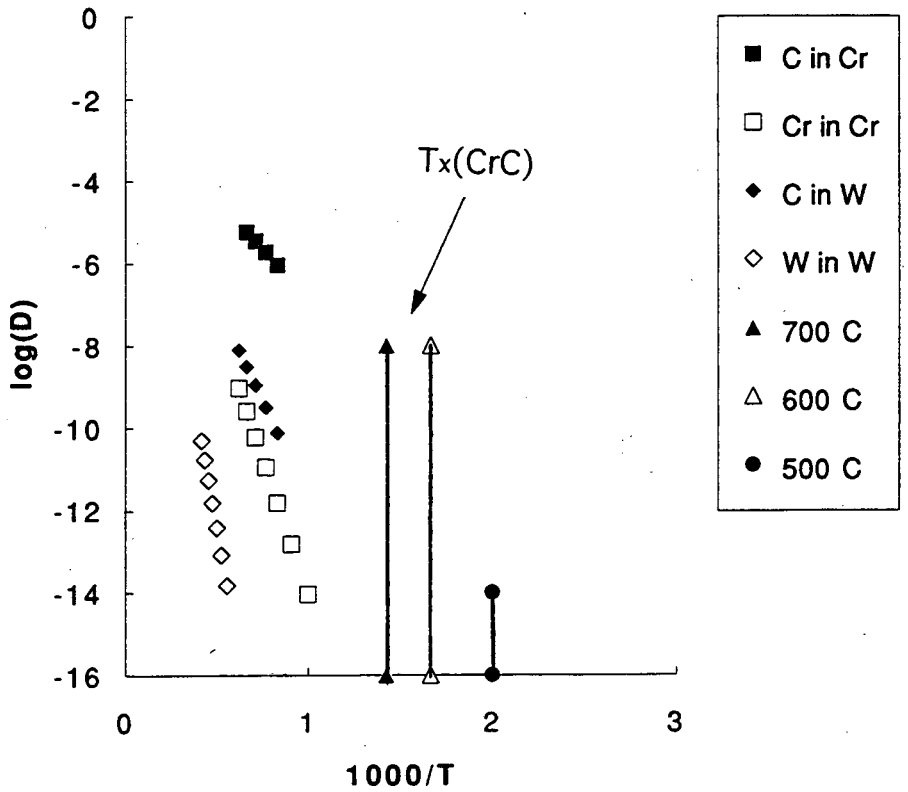
0
-2
-4
-6
-8
-10
-12
-14
-16
log(D)
0
1
2
3
1000/T
Tx(CrC)
C in Cr
Cr in Cr
C in W
W in W
700 C
600 C
500 C

Figure 4-9

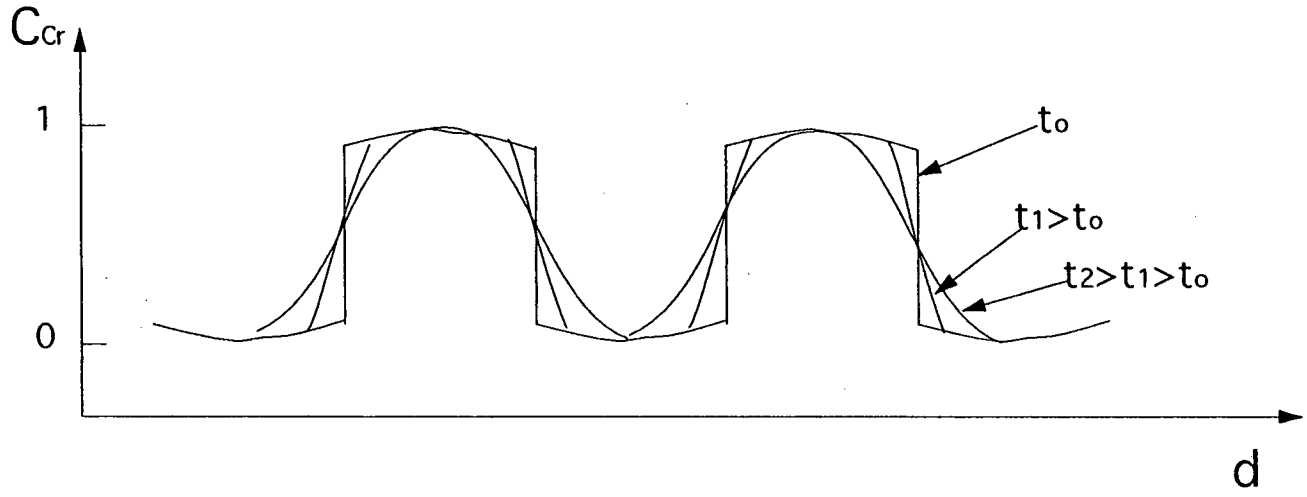

Figure 4-10

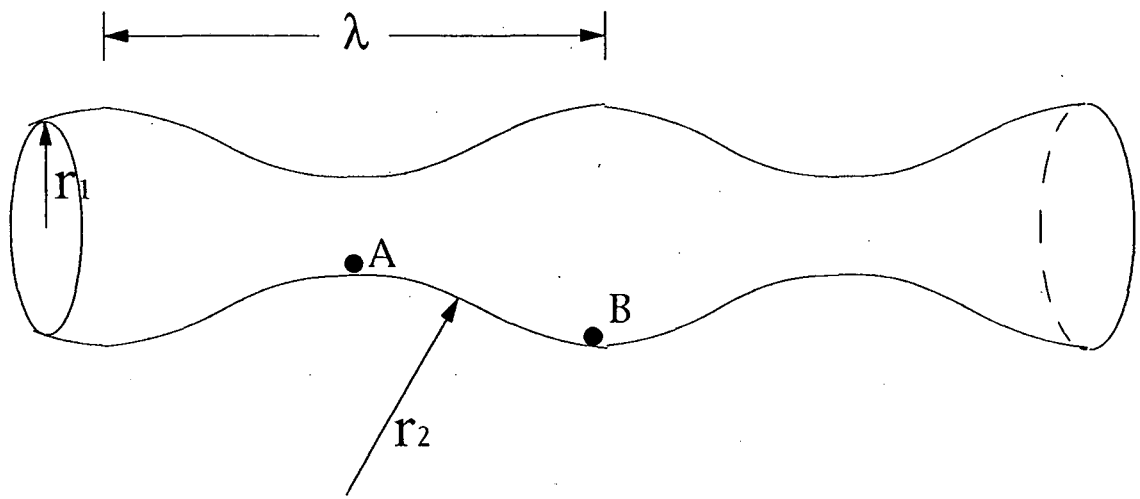

Figure 4-11

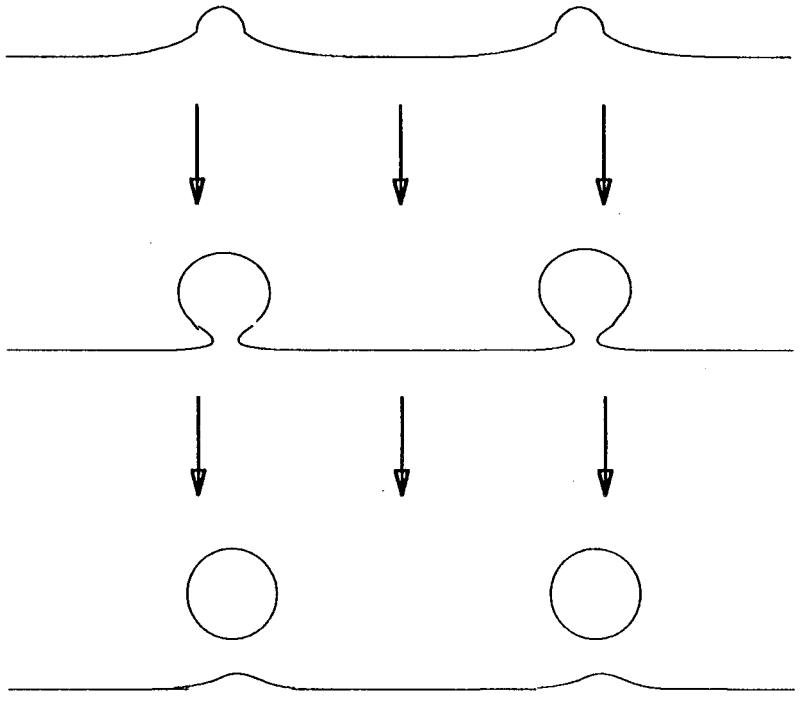

Figure 4-12

$$\gamma_{gb} = 2\,\gamma_s \cos\phi$$

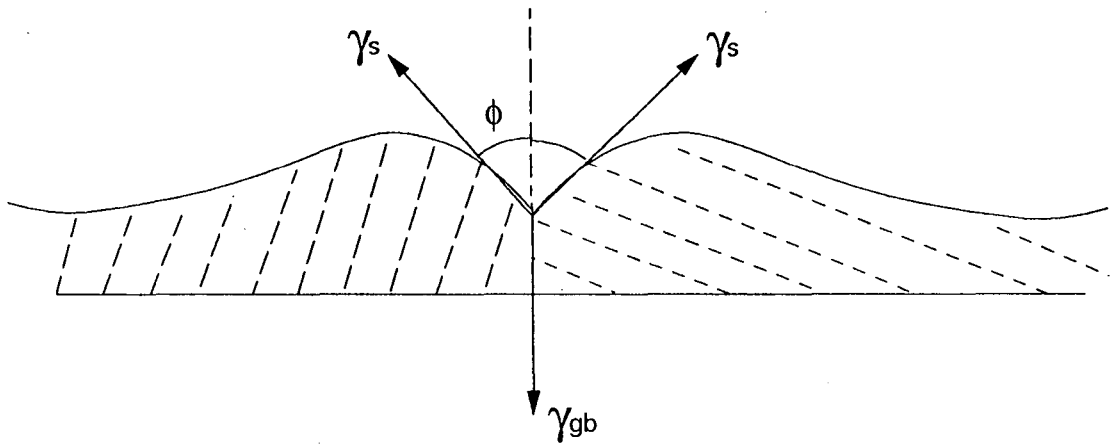

Figure 4-13

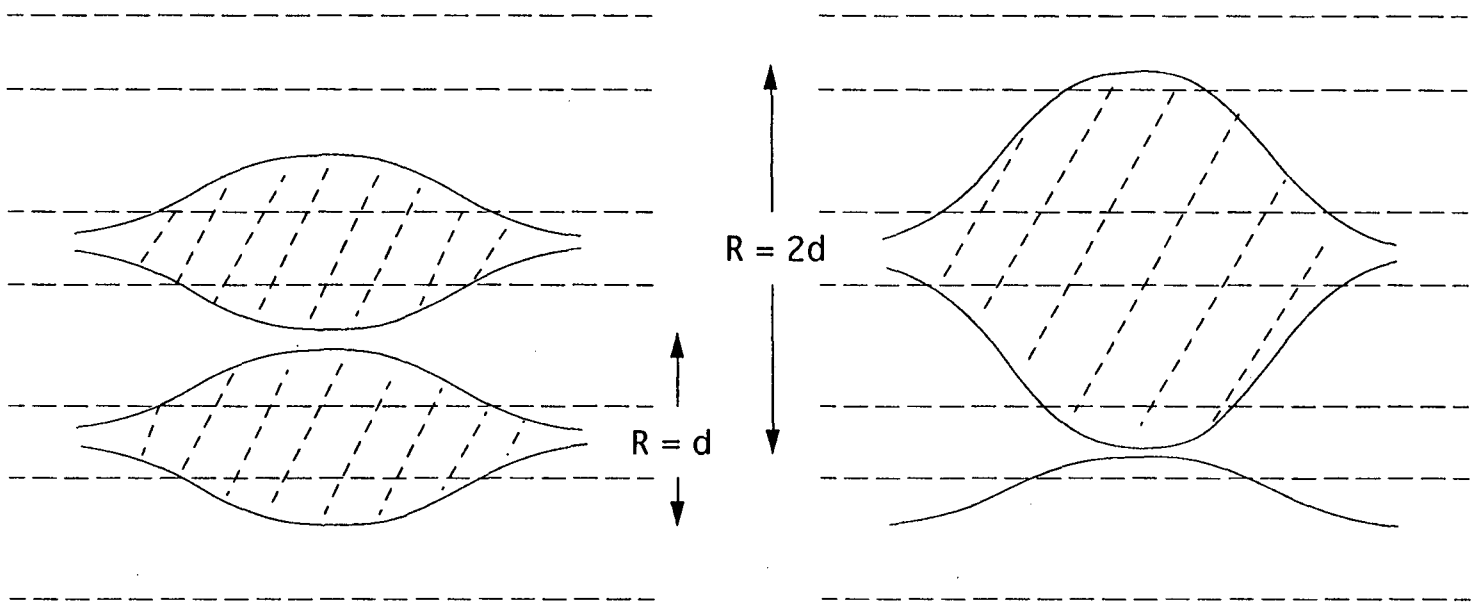

a) b)

Figure 4-14

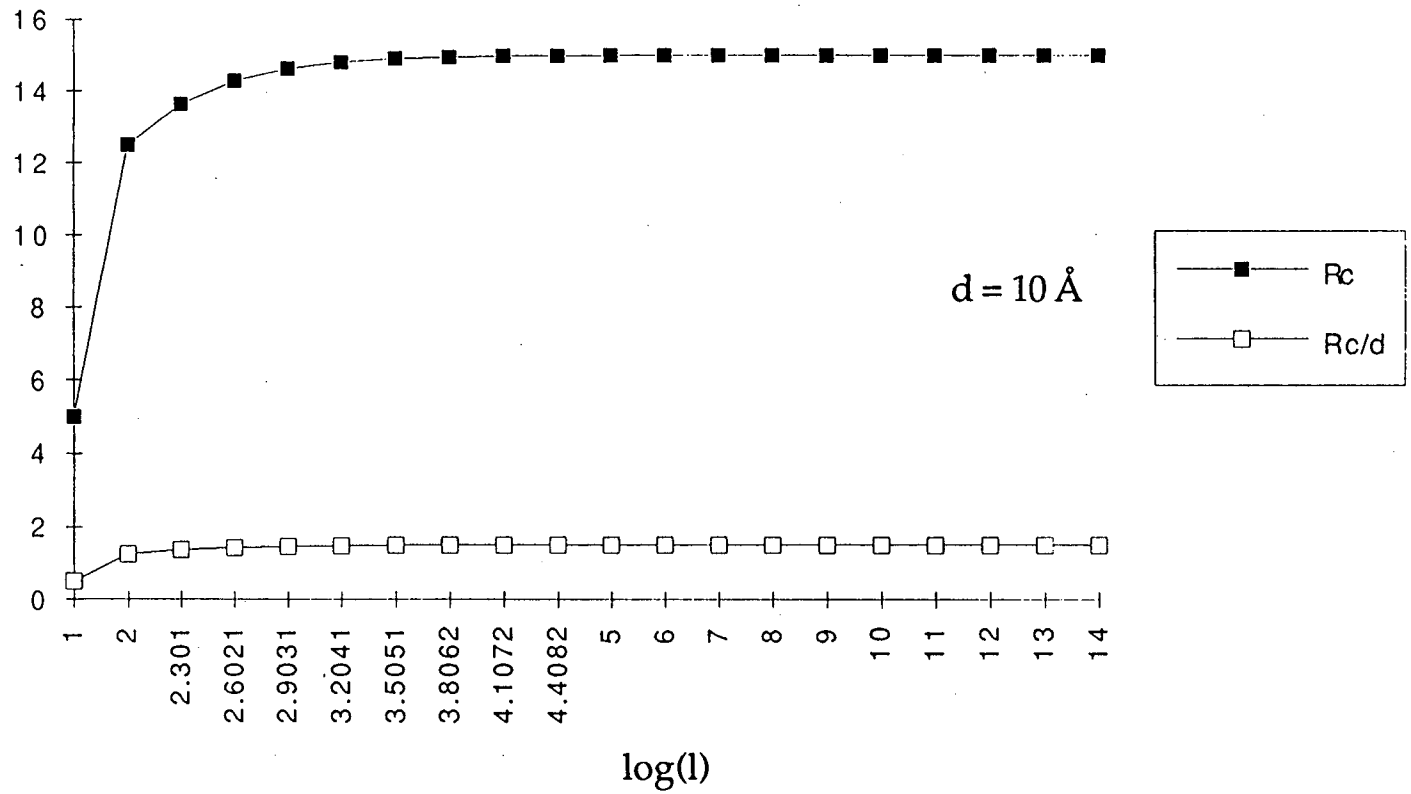
16
14
12
10
8
6
4
2
0
1
2
2.301
2.6021
2.9031
3.2041
3.5051
3.8062
4.1072
4.4082
5
6
7
8
9
10
11
12
13
14
log(l)
d = 10 Å
Rc
Rc/d

Figure 4-15

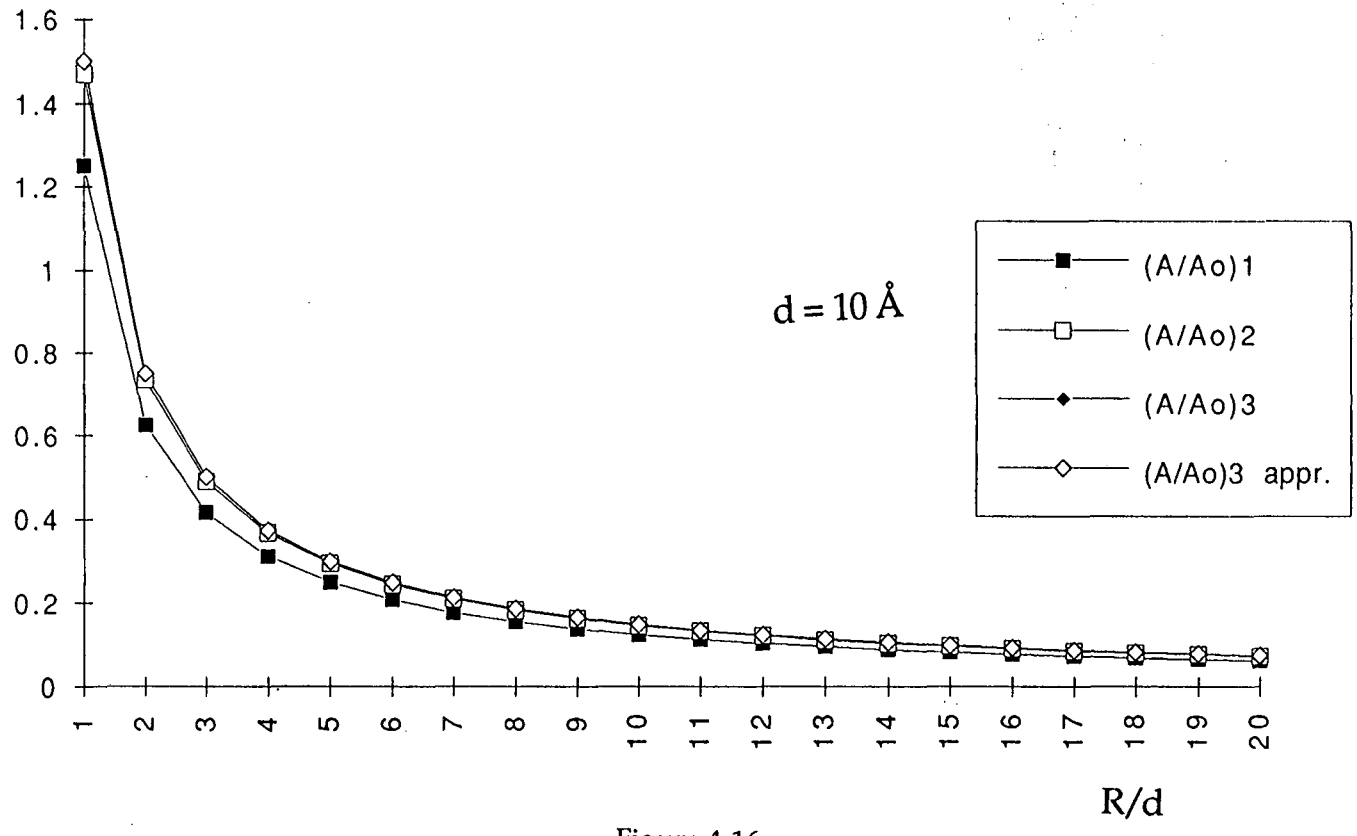
1.6
1.4
1.2
1
0.8
0.6
0.4
0.2
0
1
2
3
4
5
6
7
8
9
10
11
12
13
14
15
16
17
18
19
20
R/d
d = 10 Å
(A/Ao)1
(A/Ao)2
(A/Ao)3
(A/Ao)3 appr.

Figure 4-16

CHAPTER 5

IMPLICATIONS OF MICROSTRUCTURES ON X-RAY OPTICAL APPLICATIONS

Stability of multilayers is important in the long term durability of x-ray mirrors in practical applications. Many optics systems utilizing multilayer mirrors consist of multiple mirrors, in which reflection from each mirror must be invariant with time. From chapter 1, it was seen that the characteristics of the multilayers depend on the optical properties of the layer components, on the morphology or the interfacial structure, and on the period of the multilayers. Changes on any of these parameters, by changes in the layer structures that result from reactions between the layer constituents, would affect the performance of multilayer mirrors. The microstructures in the layers, and interactions between the layer materials in the multilayers, hence have an important effect on the interfacial structure and the performance of x-ray multilayers. The effects of the microstructural and morphological evolution on the stability of the layered structure, and of the multilayer period are discussed below.

5.1 MICROSTRUCTURE AND LAYERED STRUCTURE STABILITY

Although the resultant microstructures of each multilayer system are specific to the material constituents present in the multilayers, general trends on the microstructural and morphological evolution of multilayers upon annealing can be observed based on the experimental results and their relation to thermodynamic and kinetic properties. The

stability of the layered structure may be predicted from examination of the multilayer materials' equilibrium phase diagrams, and their interdiffusivity response to thermal anneals. The requirement of minimum intermixing and diffusion between the layers implies that conjugate-component-based multilayers whose phase diagram shows a wide miscible gap, such as Cu/C and Ru/C, are preferred to reactive-component-based multilayers whose components form intermetallic compounds. Reactive-component-based multilayers however show higher morphological stability against thermal anneals than conjugate-component-based multilayers whose layer materials prefer to remain separated. Clusters of Cu aggregates were found in as-prepared Cu/C multilayers, and short period Ru/C multilayers agglomerate into clusters of Ru crystallites in a C matrix after annealing, while multilayers of reactive-component-based systems of comparable period remain layered under similar annealing condition. Although these multilayers are far from the equilibrium state, it can be inferred that compound formation in reactive-component-based systems, which allows interdiffusion between the layers, stabilizes the layered structure, while phase separation in conjugate-component-based systems promotes agglomeration and breaking-up of the multilayers. Clustering and agglomeration in conjugate-component-based systems are driven by the reduction of the interfacial to volume ratio, since in this case, like-neighbors are preferred to unlike-neighbors in reduction of the free energy of the system.

Morphological stability in long period multilayers is less critical than in short period multilayers under similar annealing condition. All multilayers whose period is longer than 4 nm in this study remain layered under moderate annealing. Interdiffusion in reactive-component-based multilayers results in different microstructures in the layers: intermetallic compounds in W/C and Ru/B_4C multilayers, or amorphous alloys in WC/C, Cr/C, and CrC/C multilayers. As a result, the density and thus the optical

properties may change, but the layers remain flat and smooth, as seen by cross-sectional high resolution TEM.

The sharpness of the interfaces in the annealed reactive-component-based multilayers however seems to depend on the interdiffusivity coefficient of the materials constituents involved. In modulated structures, homogenization of the materials usually occurs due to the periodic chemical concentration profile, which provides a strong driving force for interdiffusion between the layers. Under similar annealing conditions, multilayer systems with low interdiffusivity exhibit sharper interfaces upon annealing than those with high interdiffusivity. This observation is illustrated by comparison of W/C and Cr/C, in which W/C has a lower interdiffusion coefficient than Cr/C, as shown by the diffusion data and discussed in Chapter 4. Cross-sectional HRTEM images of annealed W/C multilayers show a clear boundary between the carbide and the C layers, while strong interdiffusion in Cr/C multilayers leads in a gradual concentration gradient at the interfaces along with amorphization of the crystalline Cr layers. A sinusoidal, instead of a sharp square, density profile results and reduces the reflectivity of the mirrors. Further annealing of the multilayers would result in complete mixing of Cr and C, and the multilayer properties are lost.

Conjugate-component-based multilayers thus may provide high reflectance, while reactive-component-based multilayers show more stable structures in long term applications. To understand the effects of the microstructural and morphological evolution in these multilayers on the reflectance of multilayer mirrors, the relationship between the microstructural and interfacial roughness and the normal incidence reflectance of as-prepared and annealed conjugate-component-based (Ru/C) and reactive-component-based (Ru/B_4C) multilayers is studied.

5.1.1 Effects of Microstructural and Interfacial Roughness on Reflectance of Ru/C and Ru/B_4C Multilayers

5.1.1.1 Background

Multilayers of 3.5 nm period Ru/C and Ru/B_4C were used for the comparison. using specular and non-specular, diffuse x-ray scattering, and HRTEM. Beside their difference in materials characteristics mention earlier, these two multilayer systems are also good candidates for normal incidence reflecting mirrors at wavelengths near 7 nm, based on their optical properties. In this study, high angle x-ray scattering furnishes complementary information on the microstructure in the layers to the TEM results, and specular and non-specular, diffuse low angle x-ray scattering provides a measure of the interfacial roughness in the multilayers. Roughness at the interfaces reduces the specular component, and produces a diffuse component in the scattering.[1-4] The two limiting types of roughness present in the multilayer structures are correlated and uncorrelated. Correlated roughness originates from either the substrate or a defect in the structure, and grows conformally from one layer to the next, while uncorrelated roughness is intrinsic to the individual layers.

5.1.1.2 Normal Incidence Reflectance Measurements

The normal incidence reflectance of as-prepared and annealed Ru/C and Ru/B_4C multilayer samples is shown in Figure 5-1. Comparison of the reflectivities shows that the Ru/B_4C multilayer has superior performance. The reflectance of the as-prepared Ru/B_4C is 10%, while that of the Ru/C multilayer is 8%. The bandwidth is approximately 0.1 nm for both multilayers. Dramatic changes were observed in the performance of the multilayers after annealing. The reflectivity of the Ru/B_4C multilayer

decreased to 7%, while the reflectivity of the Ru/C multilayer decreased to 3%, upon annealing. The bandwidth of the Ru/B_4C multilayer remains approximately the same before and after annealing, while the bandwidth of the Ru/C shows a slight increase (~ 15%) upon annealing. The Ru/C measurements also show a shift of the peak toward longer wavelength after annealing, which indicates that the period has expanded (by 14%) upon annealing, as observed earlier in many metal/carbon multilayers.[5-7] The Ru/B_4C multilayer however shows only a slight shift or increase in the period (roughly 1%). The reflectivities of the samples are summarized in Table 5-1.

5.1.1.3 High Angle X-ray Scattering

High angle x-ray scattering of the multilayers confirms the microstructural results obtained by TEM. Figure 5-2 shows the asymmetric scans of the multilayers. The microstructures of the as-prepared multilayers are predominantly amorphous. Annealing of the multilayers results in different microstructures. The Ru/B_4C multilayer remains predominantly amorphous after annealing, as seen in scan 5-2b. Weak peaks can be detected at positions of some crystalline hexagonal RuB_2 peaks, which indicates the presence of some nano-crystallites in the layers. The amorphous as-prepared Ru/C multilayer crystallizes to form elemental Ru nano-crystallites, as identified by the peaks in scan 5-2d. Symmetric θ-2θ high angle scan of the annealed Ru/C multilayer shows that the preferred orientation of the Ru crystallites perpendicular to the multilayer surface is [101], consistent with TEM results presented in chapter 3.

5.1.1.4 Specular and Non-Specular X-Ray Scattering

Low angle x-ray measurements of the as-prepared and annealed Ru/B_4C and Ru/C multilayers are shown respectively in Figures 5-3 a-d. Each figure shows the

specular component and the non-specular component of the scattering. The specular scans contain both the specular and the diffuse components, and exhibit as high as 8 orders of Bragg peaks above the smooth background scattering. The rise in the background scattering starting around 12 degrees is from diffuse scattering from the fused silica substrate. Determination of the correlated and uncorrelated roughness is acquired from studying the specular and diffuse scattering. In general, multilayers with smooth and modulated structure show enhanced higher order Bragg peaks. Samples with a higher degree of roughness exhibit lower Bragg intensities and higher smooth background in the non-specular scattering measurements. Existing theories predict that non-specular scattering from correlated and uncorrelated roughness exhibit different scattering behaviors.[2-4] Vertically correlated components of roughness result in diffuse scattering with Bragg peaks like in specular scans. Uncorrelated components of roughness contribute a more featureless and smooth component to the diffuse intensity. In all the samples, non-specular scattering through the Bragg peaks follows closely that of the corresponding specular, which indicates the presence of correlated roughness in the multilayers.

Comparison of the x-ray measurements of the as-prepared samples indicates a higher quality in the Ru/B_4C than in the Ru/C multilayer. Both specular and diffuse scattering of the Ru/B_4C multilayer shows stronger higher order peaks than the Ru/C multilayer. The diffuse component of the as-prepared Ru/B_4C is relatively weaker than that of the Ru/C multilayer, which indicates smoother interfaces in the Ru/B_4C than in the Ru/C multilayer. The two systems exhibit very different responses to annealing. The Ru/B_4C multilayer shows little change after annealing. Measurements from the specular and diffuse components of both the as-prepared and annealed samples show almost identical scattering profiles. The first order Bragg peak in the specular scattering decreases by a small amount (70% to 60%), while that of the diffuse component shows

only a slight increase after annealing. The change in the roughness observed in the Ru/B_4C multilayer is much smaller than that in the Ru/C multilayer.

Annealing of the Ru/C multilayer results in dramatic changes in the diffuse scattering. The highest order Bragg peaks in both specular and diffuse scattering disappear after annealing, which suggests enhanced roughness at the interfaces. The first order specular Bragg peak also shows a significant decrease, from 63 to 46%, after annealing. A strong enhanced smooth diffuse background is observed in the annealed sample, which indicates that the roughness of annealed sample is much higher than that of the as-prepared sample. The increase in the smooth background indicates that this thermally induced roughness is largely uncorrelated, which is consistent with the cross-sectional TEM results that show crystallization and agglomeration occur randomly in the Ru layers. Sharp Bragg peaks in the offset scans indicate that the correlated component of roughness evident in the as-deposited sample remains after annealing. This vertically correlated component to the diffuse scattering presumably results from conformal growth induced by substrate roughness.

5.1.1.5 Analysis of X-ray Scattering Result

The ratio of the diffuse to the specular scans of the scattering provides a sensitive measure of the roughness at the interfaces. Figure 5-4 plots the ratios of the diffuse to the specular component of the as-prepared and annealed Ru/C and Ru/B_4C multilayers. Specular scans contain both the specular and diffuse components of the scattering. The ratios range between zero and one, and thus approach unity as the scattering becomes purely diffuse. As discussed earlier, samples with a higher degree of roughness have a stronger diffuse component and thus the ratios approach unity at a smaller angle than that of smooth samples. Scattering from correlated roughness results

in similar profiles through the Bragg peaks between the specular and diffuse scattering. The presence of uncorrelated roughness, on the other hand, reduces the diffuse Bragg peaks from the specular, and enhances the diffuse smooth background, which produces spikes in the ratio at the Bragg positions.

The ratios of the background scattering of the as-prepared and annealed Ru/B_4C multilayers show insignificant difference, which indicates that there were little changes in the interfacial roughness in this multilayer upon annealing. These ratios seem to approach unity at around 13 degrees. The values beyond 12 degrees however are meaningless regarding multilayer roughness since the scattering is dominated by the diffuse scattering from the bulk substrate, which is the same in the specular and non-specular scans of the multilayer scattering, as seen in Figure 5-3. They both show smooth curves, with small spikes at the Bragg positions, which suggests that roughness in these multilayers is highly correlated. The presence of some small fluctuations in the annealed sample at lower Bragg peak positions implies that the as-prepared multilayer has a higher degree of correlation in the roughness than the annealed sample.

The plots of the as-prepared and annealed Ru/C multilayers in Figures 5-4c and 5-4d show significant differences from each other. The annealed plot approaches unity at a much lower angle (between 7 and 8 degrees) than the as-prepared Ru/C (between 9 and 10 degrees) and the Ru/B_4C plots. This strong increase in the smooth diffuse background scattering upon annealing of the Ru/C multilayer indicates that the degree of roughness in the annealed sample is much higher than that in the as-prepared sample. In addition, the presence of the spikes at the Bragg positions suggests that the roughness in the annealed sample is highly uncorrelated compared to the as-prepared sample. Comparing the plots of the Ru/C and the Ru/B_4C samples shows that both the as-prepared and annealed Ru/B_4C multilayers have smoother interfaces than even the as-

prepared Ru/C multilayer. In increasing order of interfacial roughness, the smoothest sample is the as-prepared Ru/B_4C, followed by the annealed Ru/B_4C, the as-prepared Ru/C, and the annealed Ru/C multilayer.

5.1.1.6 Effects of Microstructure and Interfacial Roughness on X-ray Optical Properties

The microstructure of the multilayers can be related to their performance and stability. Analysis of the reflectivity values of the multilayers studied reveals that the as-prepared immiscible multilayer Ru/C yields a measured value that is closer to the calculated value than that of a compound forming Ru/B_4C multilayer. This observation is illustrated in Table 5-1, which shows the measured reflectivity of the multilayers before and after annealing, their calculated reflectivity assuming an ideal structure, and the ratio of the measured to the calculated reflectance. The ideal reflectivity of Ru/C multilayer before and after annealing is the same, because it was assumed that minimal interdiffusion occurs during annealing in this immiscible system. In the Ru/B_4C multilayer, however, some of the boron atoms in the B_4C layers diffuse into the Ru layers to form a boride. The effective density of the layers hence has changed after annealing. The exact composition inside the layers of the annealed sample however is not yet determined. In the calculation of the ideal reflectivity of this sample, it was assumed that change in the density of the Ru-rich layers is insignificant, since the boron atoms are much smaller and lighter than the Ru atoms, and probably diffuse interstitially into the Ru structure to form the boride, while change in the density of the B_4C layer was made to account for the loss of the boron atoms to the Ru layers. A few different densities were attempted, and they all show similar results. The number recorded in the table is an approximate of these values. The ratio of the measured to ideal reflectance of both multilayers decreases after annealing, from .38 to .14 for the Ru/C, and .27 to .2 for the Ru/B_4C multilayer. The reduction of the ratio, or the further deviation of the measured

reflectance from ideal value, is more dramatic for the Ru/C than the Ru/B4C sample. Partial agglomeration of the Ru layers, which results in change in the interfacial structure, as observed by high resolution TEM and x-ray scattering technique, accounts for the differences in the reflectivities. The finding has an important implication in the design of x-ray multilayers. Conjugate-component-based multilayers provide higher initial reflectance to the ideal values than multilayers that form compounds on annealing. Prolonged exposure of these multilayers to thermal annealing or x-ray irradiation however may decrease their performance to values lower than those of reactive-component-based multilayers. Reactive-component-based multilayers thus may be preferred in applications because of their superior stability, especially at short wavelengths or short periods.

5.2 Period Expansion in Metal/C Multilayers

X-ray measurements of the low-angle Bragg peaks of the metal/C multilayers reveal the expansion of the multilayer periods upon annealing, as indicated by the shift of the Bragg peaks to lower angles. Since experiments employing multilayer mirrors require that the reflected wavelengths, or the multilayer periods, remain stable over a long time, it is then important to understand the mechanism for this expansion, to be able to design more stable multilayers under thermal or radiation loading. Figure 5-5 shows the relative expansions of W/C, WC/C, and Ru/C after annealing at 500°C for 4 hours. All three systems show higher relative expansion ($\Delta d/d$) for shorter periods than for longer periods. The relative expansions of the WC/C and Ru/C multilayers appear almost linear with period, and are significantly higher than those of the W/C multilayers. Takagi et al. reported that expansion of the multilayer period on annealing was not observed in W/C multilayer of 4 nm-W / 1 nm-C, while multilayers having 1.5

nm-W / 1.5 nm-C, and 1 nm-W / 4 nm-C, expanded after annealing under the same conditions.[6] The expansion of the period upon annealing in these metal/C multilayers is most likely due to the transformation of the amorphous carbon into a more graphitic structure that has a lower density, and not a result of agglomeration of the metal-rich layers as reported by other group.[18] X-ray reflectivity studies of thin carbon films (5 to 40-nm) in fact reveal the expansion of the single C films on annealing.[7] Raman spectroscopy measurements of C films also show a shift of the C peaks from the sp_3 bonding of a diamond cubic structure to the graphite sp_2 bonding after annealing.[8-9]

Expansion of the carbon layers in the multilayers also explains the differences in the relative expansions among W/C, WC/C, and Ru/C multilayers. Significant intermixing between W and C in W/C multilayers compared to that in Ru/C multilayers, and lower carbon content compared to that in WC/C, accounts for the lower relative expansions in W/C multilayers. In addition, crystallization or recrystallization of the metal layers in the longer period Ru/C and W/C multilayers, which results in higher density or thinner layers, results in lower relative expansions than in the resultant amorphous WC phase in the WC/C multilayers on annealing. Comparison of the annealing results of 3.5 nm period Ru/C, Ru/B, Ru/B_4C, and Ru/BN multilayers reveal that the period of the Ru/C multilayers expands 13.8% upon annealing at 600°c for 30 minutes, compared to less than 1% in the Ru/B_4C, 5.9% in the Ru/BN, and contraction by 1.4% in the Ru/B multilayers. Evidently, ultra thin sputtered B_4C, BN, and B layers are substantially more stable with respect to volume (density) changes than are C films.

The multilayer period in metal/Si multilayers, on the other hand, tends to decrease on annealing.[10,11] The mechanism for this contraction is mainly attributed to the interficial reactions between metal and Si.[10] Studies of metal/SiC multilayers would

be interesting and may provide stable multilayers against period expansion or contraction under loading. Recent reflectance measurements of Mo/Si also indicate a reduction in the reflectance and a shift in the reflectance peak toward shorter wavelengths after the sample was left in air for a few days at room temperature.[12] The reduction in the reflectance, which results from oxidation of the top Mo layers, continues to occur as the oxide layer thickens, while the multilayer period remains unchanged after the first decrease. The authors suggest that the contraction in this multilayer results from relaxation of the structure by rearrangement of the atoms in the layers and at the interfaces.

5.3 REFERENCES

1. J.B. Kortright, J. Appl. Phys. **70**, 7 (1991) 3620.
2. D.E. Savage, J. Kleiner, N. Schimke, Y.H. Phang, T. Janskowski, J. Jacobs, R. Kariotis, and M.G. Lagally, J. Appl. Phys. **69** (1991) 1411.
3. D.G. Stearns, J. Appl. Phys. **71** (1992) 4286.
4. Y.H. Phang, R. Kariotis, D.E. Savage, and M.G. Lagally, J. Appl. Phys. **72**, 10 (1992) 4627.
5. Y. Takagi, S.A. Flessa, K.L. Hart, D.A. Pawlik, A.M. Kaden, J.L. Wood, J.E. Keem, J.E. Tyler, in *Applications of Thin-Film Multilayered Structures to Figured X-Ray Optics*, (Proc. SPIE **563**, 1985) 66.
6. Y. Lepetre, E. Ziegler, I.K. Schuller, and E. Spiller, Appl. Phys. Lett. 48 (1986) 1354.
7. C. Lucas, T.D. Nguyen, and J.B. Kortright, J. Appl. Phys. **59**, 17 (1991) 2100.
8. R.O. Dillon, J. A. Woolam, and V. Kiatkanant, Phys. Rev. **B29** (1984) 3482.
9. J. Ager, C.A. Lucas, and T.D. Nguyen (unpublished).
10. Z. Jiang, X. Jiand, W. Liu, and Z. Wu, J. Appl. Phys. **65**, 1 (1989) 196.
11. J.B.Kortright, S. Joksch, and E. Ziegler, J. Appl. Phys. **69**, 1 (1991) 168.
12. J. Underwood, K. Nguyen, and E.M. Gullikson, presented at MRS Meeting (1993).

5.4 TABLES

Table 5-1. Normal incidence reflectance and wavelength of as-prepared and annealed Ru/C and Ru/B_4C multilayers.

5.5 FIGURES

Figure 5-1. Absolute normal incidence reflectance of Ru/C and Ru/B_4C.

Figure 5-2. a)-d) Asymetric high angle scans reveals the microstructure in the multilayers. The position of hexagonal RuB_2 and Ru planes are also shown. e) Symmetric scan of the annealed Ru/C sample indicates that the preferred orientation of the Ru crystallites is 101 perpendicular to the interface.

Figure 5-3. Specular and diffuse scattering of a) as-prepared Ru/B_4C, b) annealed Ru/B_4C, c) as-prepared Ru/C, and d) annealed Ru/C multilayers. The Ru/B_4C multilayers show little changes upon annealing, while the annealed Ru/C multilayer shows an increase in uncorrelated roughness.

Figure 5-4. Ratio of the diffuse to specular scattering of the multilayers showing the correlated and uncorrelated components.

Figure 5-5. Relative expansions in metal/C multilayers.

	Ru/C		Ru/B_4C	
R	as-prepared	annealed	as-prepared	annealed
Meas.	8%	3%	10%	7%
Ideal	21%	21%	37%	~ 35%
M/I	.38	.14	.27	~ .2

Table 5-1

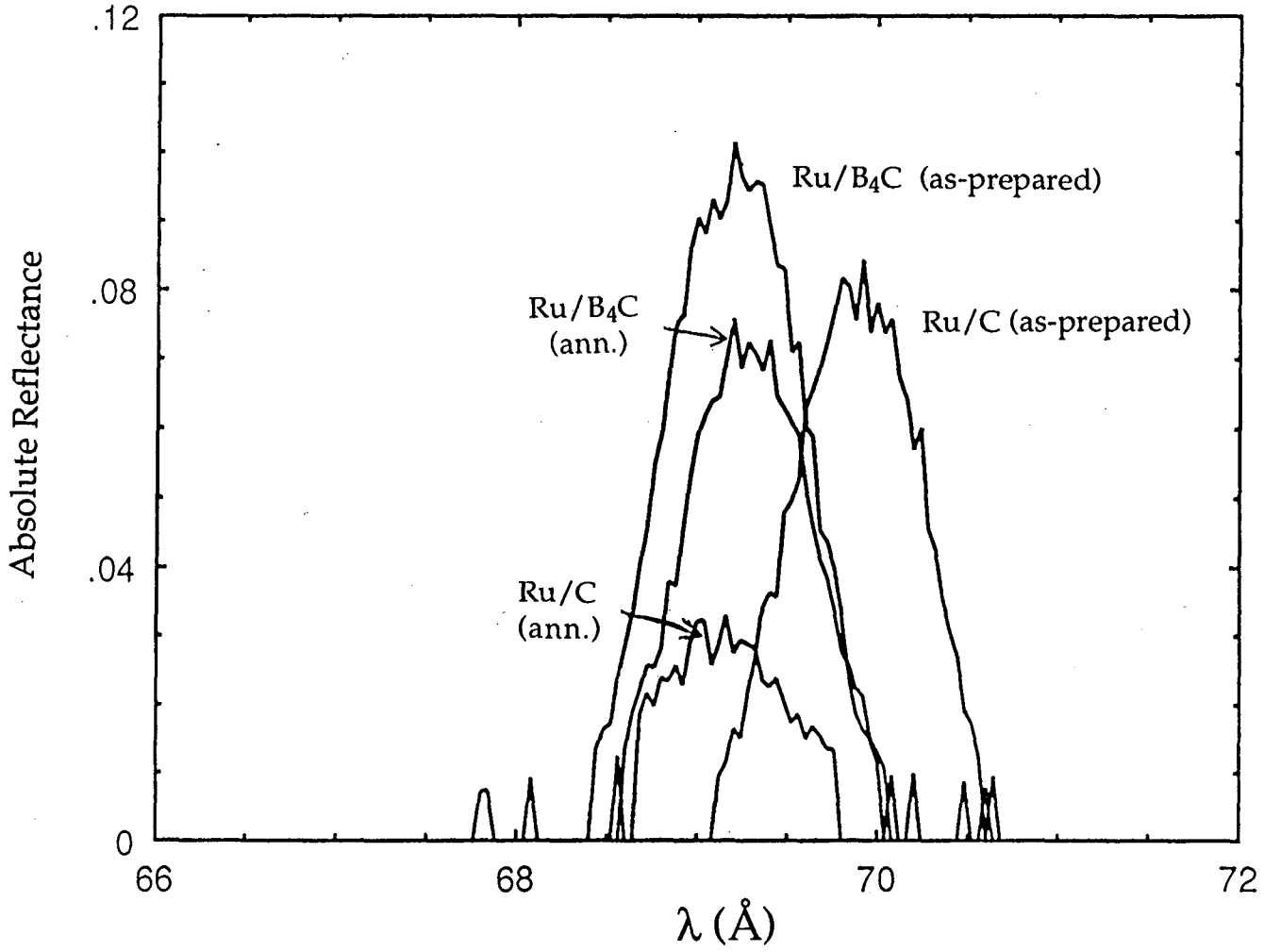
.12
.08
.04
0
Absolute Reflectance
66
68
70
72
λ (Å)
Ru/B4C (as-prepared)
Ru/B4C (ann.)
Ru/C (as-prepared)
Ru/C (ann.)

Figure 5-1

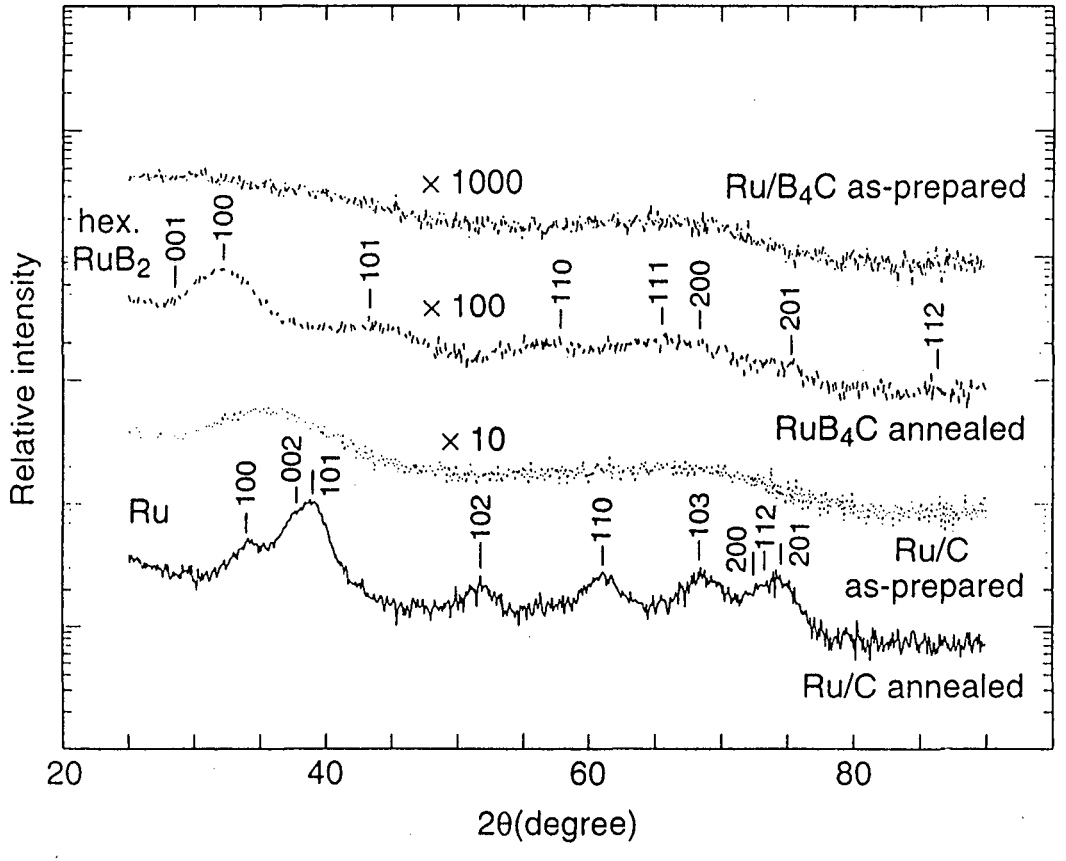

XBL 9212-5865

Figure 5-2

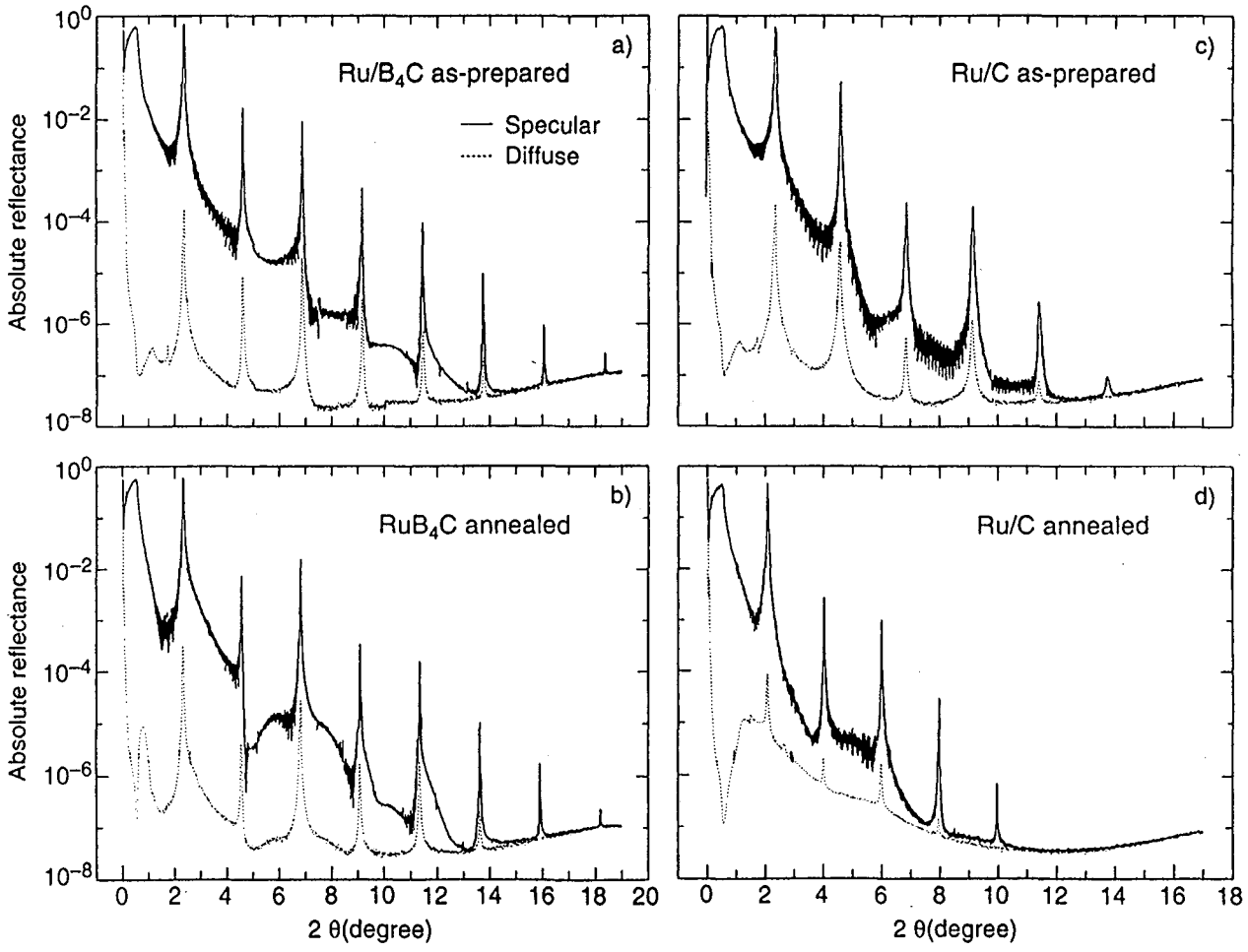
a)
Ru/B4C as-prepared
Specular
Diffuse
c)
Ru/C as-prepared
b)
RuB4C annealed
d)
Ru/C annealed
Absolute reflectance
2 θ(degree)
XBL 9212-5866

Figure 5-3

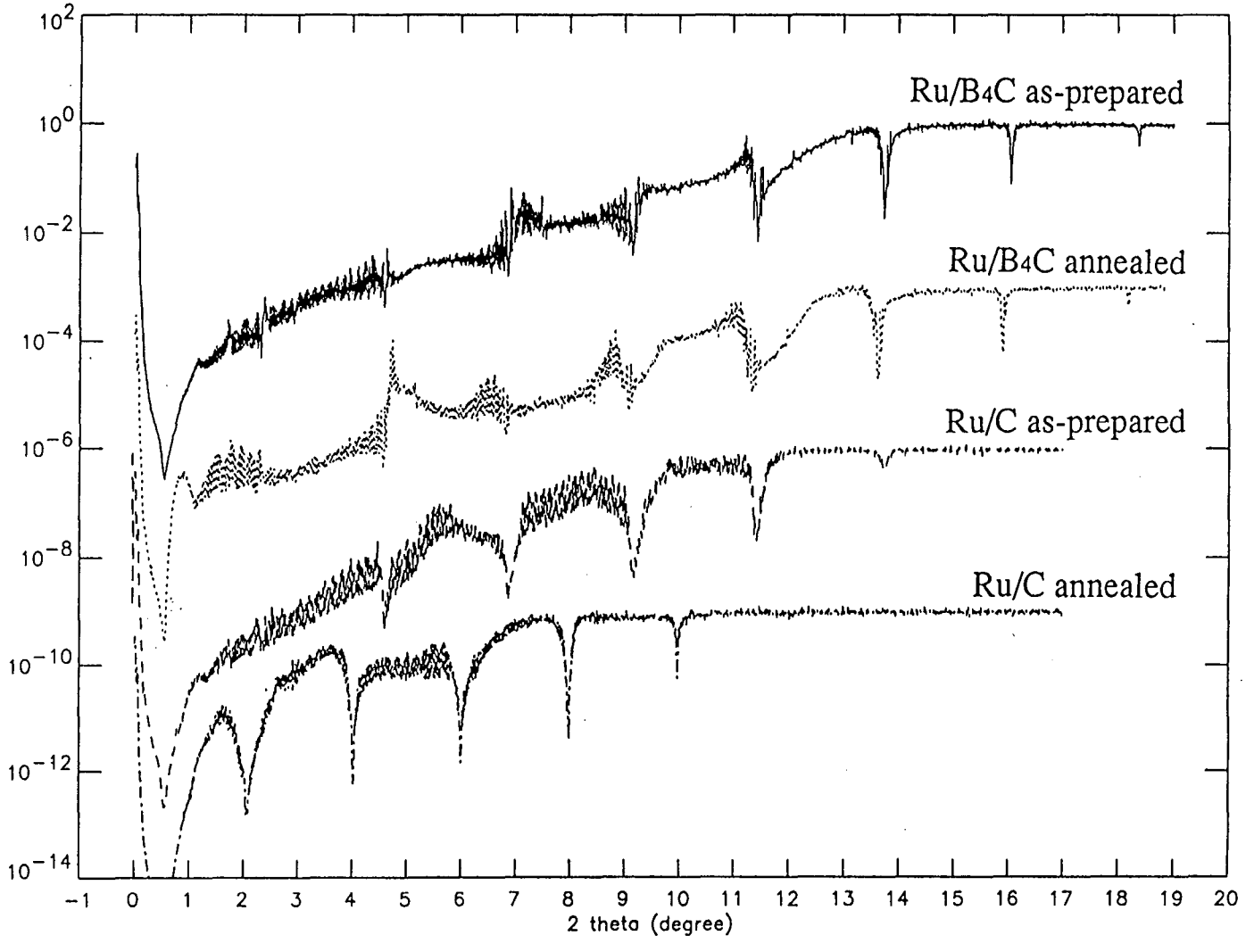
Ru/B4C as-prepared
Ru/B4C annealed
Ru/C as-prepared
Ru/C annealed
10^2
10^0
10^-2
10^-4
10^-6
10^-8
10^-10
10^-12
10^-14
-1 0 1 2 3 4 5 6 7 8 9 10 11 12 13 14 15 16 17 18 19 20
2 theta (degree)

Figure 5-4

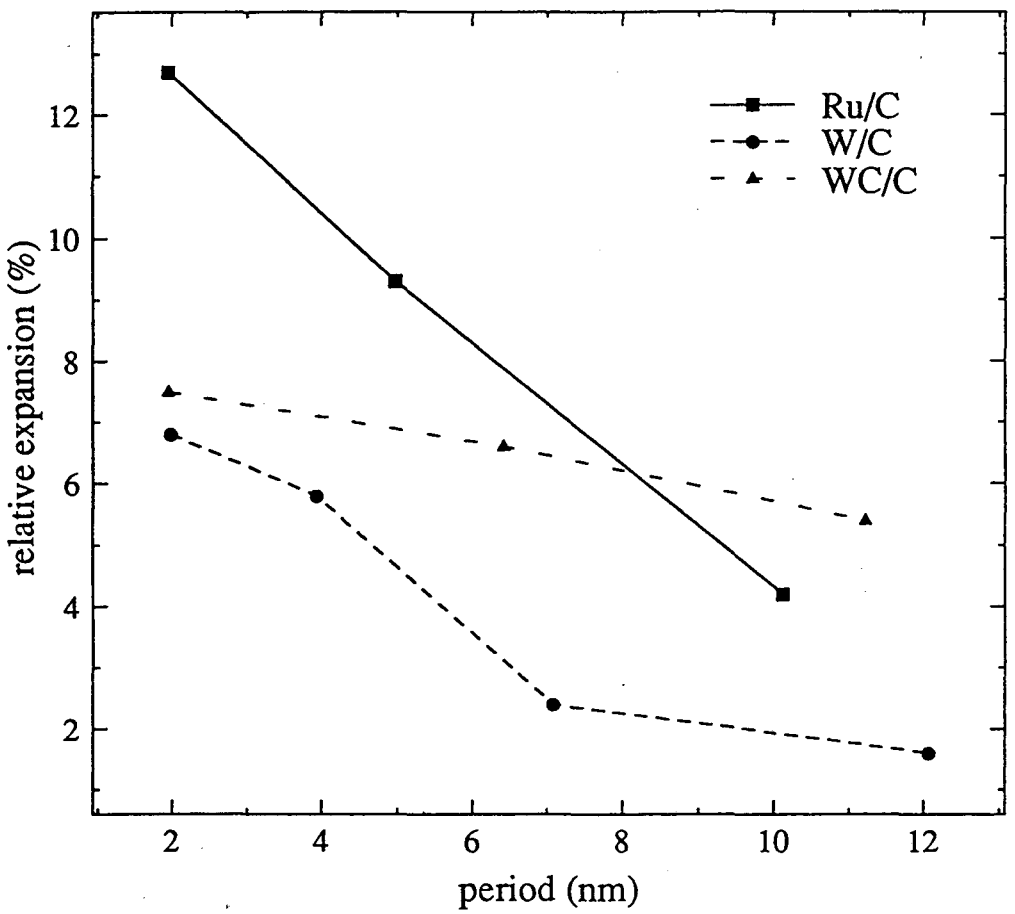

Figure 5-5

CHAPTER 6

SUMMARY

6.1 CONCLUSIONS OF THE RESEARCH

The microstructure - interface - property relationships in nanometer-period x-ray multilayer mirrors were studied. Detailed investigation of the microstructures in the multilayers under thermal treatments provides an understanding of the microstructural evolution and morphological stability of the layers in the multilayers. Comparison among different multilayers systems, and the relationships between the multilayer microstructures and their equilibrium phase diagrams were established to understand the trends observed. In cases where applicable, the microstructure and the morphology in the multilayers were related to the properties of the multilayers.

The microstructure and morphology in various period metal/C (W/C, Cr/C, Ru/C, and Cu/C) and their alloys (WC/C, CrC/C, and Ru/B_4C) multilayers were studied by cross-sectional high resolution TEM and x-ray scattering. The microstructures and their behaviors upon annealing are different for different multilayers systems, and depend on the reactions between the layer constituents. General trends among the multilayers however can be drawn from the similarities and differences in the microstructures and their evolution under thermal activation, and interpreted from their respective equilibrium phase diagrams. The two main types of multilayer systems with distinct thermodynamic and kinetic properties studied are reactive-component multilayers (W-C, Cr-C, and Ru-B_4C) whose layer materials react to form intermetallic

compounds, and conjugate-component multilayers (Ru-C, and Cu-C) whose layer materials prefer to remain separated.

In general, the microstructure of the metal layers in all as-prepared multilayers changes with period, evolving from an amorphous structure at short period to a polycrystalline one at longer period, while the layers in the alloy/C multilayers (WC/C and CrC/C) retain an amorphous structure for all periods. The different atomic sizes of the metals and carbon atoms probably impede crystallization of the intermetallic alloys at this deposition condition. Formation of the crystalline phase in the metal layers of metal/C multilayers occurs when the thickness of the "pure" metal layers reaches the critical thickness for nucleation. The "pure" metal layer thickness depends on intermixing and interdiffusion between the layer materials, which produce an amorphous alloy at the interfaces. Immiscibility and limited mutual solubility in conjugate-component multilayers promotes phase separation, and interfacial diffusion instead of volume diffusion, which leads to thicker "pure" metal layers than reactive-component multilayers for the same period. Nucleation of the crystalline phase occurs at shorter period in conjugate-component multilayers than in reactive-component multilayers.

Annealing of the multilayers results in different microstructures for different multilayer systems. Although nanometer-scale multilayer structures are far from equilibrium, and may not possess characteristics of the bulk, reactions among the constituents in the multilayers upon annealing, which results in the observed microstructure in the annealed samples, seem to be related to the characteristics of their equilibrium phase diagrams. Compound formation (W_2C, RuB_2) was observed in multilayer systems (respectively, W/C, Ru/B_4C) whose phase diagrams of the bulk exhibits the presence of intermetallic compounds at equilibrium. Because of the nano-scale of x-ray multilayers, reactions can occur at a more rapid rate than in the bulk,

which leads to crystallization and recrystallization of the intermetallic compounds at lower temperatures than those recorded in the phase diagrams. Formation of W_2C, for example, was observed in these multilayers after annealing at 500°C, although the W-C equilibrium phase diagram of the bulk indicates that this phase does not appear below ~1250°C. Solid state amorphization reactions were observed in the Cr/C multilayer system, in which interdiffusion between the polycrystalline metal layers and the amorphous C layers leads to amorphization of the structure. The driving force for SSAR is reduction in the free energy of the system, which is illustrated by the free energy curves over the composition range. The amorphous microstructure in the alloy/C multilayers (WC/C and CrC/C) remains amorphous after annealing. High carbon content in the alloy layers stabilizes the amorphous phases against crystallization under a thermal activation, probably because of kinetic factors since nucleation and grain growth of the stable intermetallic compounds may require uphill diffusion of the C atoms.

In systems that exhibit a wide miscibility gap in the solid state in their equilibrium phase diagrams (Ru/C and Cu/C), nucleation and grain growth of the elemental metals were observed after annealing, consistent with the absence of any intermetallic compounds in the phase diagrams. These immiscible phase diagrams also suggest that like atoms prefer to bond to each other, especially at the interfaces, in order to reduce the interfacial energies in the structures. Phase separation by means of clustering of Cu aggregates in a C matrix during deposition, and agglomeration and crystallization of the Ru layers in Ru/C multilayers during annealing in an attempt to reduce the interfacial area to volume ratio, thus is understood from a thermodynamic viewpoint. The mechanism of agglomeration of the Ru layers upon annealing however depends on kinetic factors. Thin amorphous Ru layers coalesce via interfacial diffusion, and crystallize concurrently before complete agglomeration occurs. Agglomeration and

grain growth are also observed in thicker polycrystalline Ru layers only after subjected to a more intense thermal activation. In thinner period multilayers, cross-layer diffusion between adjacent layers is possible, which results in Ru crystallites that are significantly larger than the initial multilayer period.

Agglomeration of the layers, which leads to changes in the interfacial morphology in the structures, is undesirable in practical x-ray optical applications since the layered structure in multilayer mirrors is no longer retained, and as a result, the performance of the mirrors is significantly reduced. The layered structure in multilayers that react to form compounds (W/C and Ru/B_4C) or remain amorphous (WC/C and CrC/C) after annealing was shown to be relatively much more stable under thermal treatments than that in immiscible systems. Change in the microstructure in these reactive-component multilayers may reduce the performance of the mirrors, although the effect is not as drastic as in the agglomerated multilayers whose interfaces are no longer flat and uniform. This observation was illustrated by studying the thermal evolution of the microstructure and interfaces, and their effects on the normal incidence reflectance of a conjugate-component (Ru/C) and a reactive-component (Ru/B_4C) multilayer. In the as-prepared state, the Ru/C multilayer showed a better performance than the Ru/B_4C multilayer, because the Ru/C multilayer possesses more defined interfaces that result from lower like-atom bond energies in the Ru-C system. Upon annealing, a greater reduction in the performance of the Ru/C multilayer was observed due to partial agglomeration of the Ru layers during annealing. Although the results of the study are specific to the multilayers investigated, some general conclusions on the microstructure - interface - property relationships can still be drawn. Multilayers, whose homogenization by interdiffusion between the layer constituents is possible, exhibit more stable layer structure and higher performance in high temperature or long-term applications than multilayers that exhibit phase separation between the layer constituents.

These studies of the microstructures and morphology in x-ray multilayers, and their evolution with period and under thermal activation, provide a basis for understanding the fabrication of smooth interfacial and more stable short period multilayer structures. Reactive-component multilayers provide multilayer structures of smooth layers and interfaces, even at 2 nm period. Conjugate-component multilayers supposedly exhibit more compositionally defined interfaces than reactive-component multilayers. High interfacial energy between the components and high mobility of the constituents in some conjugate-component multilayers however may result in clustering of the layers and thus not in a layered structure, especially when the period becomes short. Of those conjugate-component multilayers that form layered structures during deposition, the layers coarsen and agglomerate under thermal activation. Hence in high temperature and long term applications, reactive-component multilayers are expected to be more stable than conjugate-component multilayers.

6.2 SUGGESTIONS FOR FUTURE RESEARCH

Further studies of nanometer period multilayer structures are required obtain a complete understanding of the factors that affect the performance and stability of x-ray mirrors. Nanometer period multilayers also provide many academically interesting studies of fundamental materials science issues. Some suggestions based on this work include:

1) Determination of interdiffusion coefficient in steep gradient multilayers by x-ray diffraction.

2) Determination of the crystallization temperature of W_2C with layer thickness, and compare with the value recorded in the equilibrium phase diagram of the bulk, to study the crystallization temperature dependence on dimension.

3) Further studies of SSAR in Cr/C and other multilayers.

4) Further instability studies and agglomeration mechanism in Ru/C multilayers.

5) Studies of the interfacial roughness by quantitative analysis of the specular and non-specular, diffuse scattering.

6) Studies of surface roughness evolution of crystalline (W) and amorphous (a-WC) films with film thickness by specular and non-specular x-ray scattering.

7) Studies of the effects of roughness and interdiffusion at interfaces on reflectance by x-ray scattering, TEM Fresnel fringe, and other techniques.

8) Normal incidence reflectance studies of multilayers at 7 nm and shorter wavelengths.

9) Studies of stress in thin films and multilayers, and its relationship to their microstructures.

APPENDIX A

OPTICS OF MULTILAYER STRUCTURES

A.1 OPTICAL PROPERTIES AT SHORT WAVELENGTHS

Changes in the nature of interactions between photons and electronic states in solids with energy or wavelength result in dramatic changes in optical properties, from the visible to the extreme ultraviolet and x-ray regions of the electromagnetic spectrum. In the visible and ultra-violet (UV) spectral regions, photon energies correspond to differences between valence and conduction electronic levels. Thus the optical properties of pure materials tend to reflect bulk properties of the materials, and are different for metals, semiconductors, and insulators. As the wavelength decreases, almost all materials become absorbing, as the photon energies exceed the band gap energies of the structures.[1] Absorptions in solids at high energies in the extreme ultra-violet (EUV) region result from many intraband and interband transitions of the electrons as described in details in many materials science texts.[2-3] In the x-ray region, the energy of the incident photons is high enough to excite the core electrons, which results in strong absorption of the incident radiation. Because atomic core excitation dominates those optical properties in the x-ray range, bulk optical properties of materials are often described in terms of the constituent atoms' optical properties.

The refractive index is generally expressed as:[4]

$$n(\lambda) = 1 - \delta(\lambda) - i\beta(\lambda). \qquad \text{[A-1]}$$

In this expression, δ represents the refractive phase effect, β represents the loss due to absorption. The value of β is comparable to that of δ, and both δ and β are much less than unity. The x-ray optical constants $\delta(\lambda)$ and $\beta(\lambda)$, which depend on both the incident wavelength and the specific atoms present, are related to the real and imaginary parts of the atomic scattering factors, $f_o + f'(\lambda)$ and $f''(\lambda)$, respectively, by the relations:

$$\delta(\lambda) = \frac{N_a r_e \lambda^2}{2 \cdot \pi} \cdot (f_o + f'(\lambda)) \qquad \text{[A-2]}$$

$$\text{and } \beta(\lambda) = \frac{N_a r_e \lambda^2}{2 \cdot \pi} \cdot f''(\lambda) \qquad \text{[A-3]}$$

where N_a is the atomic number density and r_e is the classical electron radius,

$$r_e = \frac{e^2}{m_o \cdot c^2}. \qquad \text{[A-4]}$$

In this equation, e and m_o are, respectively, the charge and mass of the electron, and c is the speed of light. In these expressions, f_o approaches the number of electrons in the atom for forward scattering, and $f'(\lambda)$ and $f''(\lambda)$ are associated with excitation of the core electrons by the incident photons, and thus show strong characteristic spectral structure near absorption edges of the atoms.

A.2 REFLECTION AT AN INTERFACE

The physics of reflection from an interface is described in many optics texts.[4-5] When an electromagnetic wave is incident on a surface or an interface between two media, part of the wave is transmitted into the second medium, and part is reflected back into the first medium. At the interface, where the incident, transmitted, and reflected waves meet, they must obey certain boundary conditions demanded by Maxwell's equations, i.e., the normal component of the magnetic field and the transverse component of the electric field E are continuous across the interface. The electric field amplitudes of the waves are obtained by solving these boundary equations, which give the Fresnel equations that describe the behavior of the waves at an interface. The reflection coefficient, or the ratio of the reflected to the incident field amplitudes for waves at an interface between two media, or layers, *i* and *j*, are:[4]

$$r_{i,j} = \frac{|E_i'|}{|E_i|} = \frac{(N_i - N_j)}{(N_i + N_j)}, \qquad \text{[A-5]}$$

in which:

$$N_{i,j} = n_{i,j} \cdot \cos\phi_{i,j} \qquad \text{(s-polarization)} \qquad \text{[A-6]}$$

$$N_{i,j} = \frac{n_{i,j}}{\cos\phi_{i,j}} \qquad \text{(p-polarization)} \qquad \text{[A-7]}$$

n_i, n_j are the complex indices of refraction of layers *i* and *j*, respectively, and ϕ_i, ϕ_j are the angles of incidence, and transmission, measured perpendicular to the surface. The reflection from the interface is defined in terms of the reflection coefficients as:

$$R = r_{i,j}^2. \qquad \text{[A-8]}$$

For normal incidence (ϕ=0) the ratio of the field amplitudes reduces to:

$$r_{i,j} = \frac{(n_i - n_j)}{(n_i + n_j)} \qquad \text{[A-9]}$$

so that the reflection coefficient at normal incidence is:

$$R = \frac{\left|(n_i - n_j)^*(n_i - n_j)\right|}{\left|(n_i + n_j)^*(n_i + n_j)\right|}. \qquad \text{[A-10]}$$

For x-ray wavelengths, $n = 1 - \delta - i\beta$, which yields:

$$R = \frac{\left|(\delta + i\beta)(\delta - i\beta)\right|}{\left|(2 - \delta + i\beta)(2 - \delta - i\beta)\right|}, \qquad \text{[A-11]}$$

and δ and β are typically much smaller than unity, $\delta << 1$ and $\beta << 1$, then:

$$R = \frac{\delta^2 + \beta^2}{4} \qquad \text{[A-12]}$$

which is the reflection coefficient for a single interface at normal incidence.

A.3 CALCULATION OF MULTILAYER REFLECTANCE

Reflectance from a multilayer of N periods is calculated by combining reflectances from all interfaces in the multilayer structure. A multilayer of N bilayers has 2N interfaces between the layers, and interfaces between the top layer and vacuum, and between the last layer and the substrate. The calculation thus involves interference from 2N + 2 interfaces and 2N individual layers. There are two approaches to this calculation: kinematical theory and dynamical theory. Kinematical theory treats the reflection from each layer as being independent of those from other layers. This is quite a crude approximation since it neglects all wave interactions such as multiple reflections and reduction of the transmitted wave as it travels through the layer in the structures.

A more appropriate computational method for calculating reflectance of multilayer structures employs the dynamical theory of scattering, which accounts for all wave interactions. The two most popular computational methods are the recursive,[6-7] and matrix methods.[8-9] In the recursive method, the recursion formula for reflection from one layer f is:

$$r_f = \frac{r_j + r_{j+1} \cdot \exp(-2i\alpha)}{1 + r_j r_{j+1} \cdot \exp(-2i\alpha)} \qquad \text{[A-13]}$$

in which

$$\alpha = \frac{2 \cdot \pi \cdot d_f \cdot n \cdot \cos\theta_i}{\lambda} \qquad \text{[A-14]}$$

and r_j, r_{j+1} are the reflected amplitudes form the top and bottom, respectively, of the layer f, and a is the phase retardation of the wave propagating through the thickness d_f

of the layer. Repeated application of these formula to interfaces from the substrate to the top layer of the multilayer yields the total reflection R of the multilayer.

The matrix method was first derived by Abeles.[10] In this method, the values of **E** and **H** of the jth layer are related to those of the $(j+1)^{th}$ layerd by a 2 x 2 characteristic matrix:

$$\begin{bmatrix} E_j \\ H_j \end{bmatrix} = \begin{bmatrix} A & B \\ C & D \end{bmatrix} \cdot \begin{bmatrix} E_{j-1} \\ H_{j-1} \end{bmatrix}. \qquad \text{[A-15]}$$

The four elements in the characteristic matrix are complex for soft x-ray and x-ray incident wavelengths. Derivations of these quantities can be found in reference 4. The characteristic matrix for the whole multilayer is simply the product of all matrices relating each pair of adjacent layers in the multilayer. For bilayer-period multilayers used in optical applications, however, this matrix is simply the product of the matrices corresponding to the layers in one period raised to the number of periods in the multilayer. Reflectance R of the multilayer structure is obtained from the ratio of the reflected to incidence amplitudes, similar to the derivation of the Fresnel equations, with exception that the whole multilayer is treated as one single surface.

A.4 MULTILAYER IMPERFECTIONS

The Fresnel equations for reflection by a single surface or multilayer structures assume that the interfaces between the layers are perfectly smooth and flat. These models, however, are an approximation of the interfaces in real multilayers. Roughness at interfaces may result from differences in local arrangements and intermixing of the atoms at the interface, and can involve thicknesses of many atomic planes. Interfacial

roughness can reduce reflectivity to values that are much lower than that given by the Fresnel equations for an ideal structure.

The theory of multilayer structures with rough interfaces has been developed by several authors.[8-9,11-12] They assumed that the height variations at the interfaces can be described by a Gaussian curve with an rms roughness σ.[12] The modified reflectance is determined by introducing a correction factor for the reduction of the reflectivity,

$$r = \exp\left(-2\cdot\left(\frac{2\cdot\pi\cdot\sigma\cdot\cos\theta_i}{\lambda}\right)^2\right). \qquad \text{[A-16]}$$

The reduced reflectance is the product of this Debye-Waller factor and the reflectance obtained from the Fresnel equations. Much experimental work remains to be done, however, in the experimental validation and control of this effect.

More accurate calculations of the reflectivity of multilayers with rough interfaces require rigorous examination of scattering from non-ideal surfaces or interfaces. Rough surfaces or interfaces yield an additional non-specular component in the scattering, and results in the reduction of the specular component. The scattering geometry of the non-specular component is such that the scattering vector points away from the surface normal, whereas that of the specular is perpendicular to the surface. Scattering of the non-specular component in W/C multilayers has been measured to be about one to three orders of magnitude lower than that of the specular, depending on the degree of roughness of the interfaces in the multilayers.[13-14] The theory of x-ray scattering from interfacial roughness in multilayer structures has been developed,[13,15-16] although refinement is still needed to fit with the experimental measurements to understand its effects on the reflectivity performance of multilayers. Non-specular scattering studies

can also be used as a tool to characterize the roughness of the interfaces and the quality of the multilayer structures.

A.5 REFERENCES

1. J.B. Kortright, in *Free Electron Laser Handbood* (Elsevier Science Publishers B. V., Amsterdam, The Netherlands, 1988).
2. F. Wooten, *Optical Properties of Solids* (Academic Prss, New York, 1972).
3. R.B. Bube, *Electronics in Solids - An Introductory Survey*, 2nd ed. (Academic Press, 1988).
4. M. Born and E. Wolf, *Principles of Optics*, 6th ed. (Pergamon Press, NY, 1980).
5. J.D. Jackson, *Classical Electrondynamics*, 2nd ed. (John Wiley & Sons, New York, 1975).
6. J.H. Underwood and T.W. Barbee, Jr., AIP Conf. Proc. **75** (1981) 170.
7. J.H. Underwood and T.W. Barbee, Jr., Appl. Optics **20** (1981) 3027.
8. A. E. Rosenbluth and J. M. Forsyth, AIP Conf. Proc. **75** (1981) 280.
9. P. Lee, X-Ray Diffraction in Multilayers, Opt. Comm. **37**, 3 (1981) 159.
10. F. Abeles, Ann. Phys. 12th Series **5**, 596 (1950) 709.
11. A. Rosenbluth and P. Lee, AIP Conf. Proc. **75** (1981).
12. E. Spiller, AIP Conf. Proc. **75** (1981) 124.
13. D. E. Savage, J. Kleiner, N. Schimke, Y.-H. Phang, T. Jankowski, J. Jacobs, R. Kariotis, and M. G. Lagally, J. Appl. Phys. **69** (1991) 1411.
14. J. B. Kortright, J. Appl. Phys. **70** (1991) 3620.
15. D. E. Savage, N. Schimke, Y.-H. Phang, and M. G. Lagally, J. Appl. Phys. **71**, 7 (1992) 3283.
16. D. G. Stearns, J. Appl. Phys. **65** (1989) 491.

APPENDIX B

EFFECTS OF FRESNEL FRINGES ON INTERPRETATION OF INTERFACIAL STRUCTURES IN MULTILAYERS FROM CROSS-SECTIONAL HRTEM IMAGES

B.1 INTRODUCTION

Cross-sectional High-Resolution Transmission Electron Microscopy (HRTEM) has proved to be a powerful technique in examining the structure and morphology at multilayer interfaces at an atomic scale. Assessment of the interfacial structures quantitatively from these TEM images in some cases however can be difficult due to the Fresnel fringe effects, which produce different apparent structures with specimen thickness and defocus values in the images. An example of the effects is illustrated in Figure B-1, which shows a cross-sectional HRTEM image of a wedge-shaped specimen of a 4 nm period W/C multilayer. In this image, the specimen is thicker at the Si substrate, and gradually becomes thinner toward the specimen edge. The fringes appear more visible, and their spacing appears to be larger at the thinner edge than at the thicker region of the specimen. Even with a uniform thickness specimen, however, the intensity of the fringes also increases with increasing defocus away from the minimum contrast. Optimum resolution in bright-field imaging is obtained at the Scherzer defocus, which is about 50 nm from the minimum contrast for most high resolution microscopes, and thus Fresnel fringes are present in the images when imaging at this optimum condition. The effects of these fringes have been commonly overlooked in efforts of making quantitative interpretation of interfacial profiles.

Fresnel-fringes however offer a unique technique to characterize the structures and composition at interfaces. This method has been employed in the investigation of structures and defects in grain boundaries,[1-4] dislocations,[5-6] precipitate platelets,[7] twin boundaries,[8] metal interfaces,[9-14] and multilayer structures.[15-18] Modeling of the structures to correlate the fringe contrast with defocus and interfacial composition[14,16] for different layer widths[13] have also been attempted quite extensively. It has been demonstrated that the Fresnel fringe spacing primarily relates to the layer thickness, while the fringe contrast or intensity as a function of defocus, relates to the magnitude of the localized change in the scattering potential and thus to the change in composition.[3] The form of the fringes is more closely related to the abruptness of the composition change at the interface.[13] It has been shown that the fringe intensity is a function of the layer or boundary width, scattering potential, specimen thickness, and beam convergence.[3] The intensity depends more strongly on the interface potential than on the layer or boundary thickness, and it is proportional to the specimen thickness at constant $\Delta V/V$, where ΔV is the potential difference across the interface, and V is the potential of the layer. The limiting factor in the accuracy of the method hence depends on the accurate determination of the thickness of specimen under observation.

Fresnel fringes result from the electrons experiencing an abrupt change in the scattering potential parallel to the electron beam path. Imaging of multilayers in cross-section, in which the electrons travel parallel to the interfaces between the two layer materials, always results in such fringes. X-ray multilayers having alternating layers of very different atomic numbers or scattering powers are more prone to these fringes than the heterostructures having less contrast layers. The high-Z layers in the multilayers represent the strong, while the low-Z layers represent the weak scattering potential regions in a periodic well potential profile. Most of previous calculations of the Fresnel contrast with defocus have simulated their models based on perfect, or symmetrical

trapezoid-shaped potential wells,[13] as shown in Figures B-2a and B-2c. The interfaces in the multilayers are not perfect, e.g., they can not be represented by a square-well potential profile, due to intermixing and diffusion between the layers, which create a potential gradient at the interfaces. Furthermore, the gradients at interfaces of high-Z/low-Z layers may be different from those at low-Z/high-Z interfaces. The multilayers thus can have one of the four potential profiles shown in Figure B-3. In these profiles, the potentials have been assumed to be uniform across each layer. The infinite slopes in the potential wells in Figure B-2a represent the perfectly sharp interfaces between the layers, while the finite slopes in Figure B-2b to B-2d represent the intermixing of the constituents in the layers, where in this case a linear gradient in the composition of the mixing has been assumed. The true composition at the interfaces, however, can also be of a non-linear shape representing a non-uniform change in the constituents across the interface. The boundaries of each layer could be of any combination of perfectly sharp and intermixing interfaces, as of a perfectly sharp and a mixing of interfaces shown in Figure B-2b, of a symmetrical mixing of interfaces in B-2c, and asymmetrical interfaces in B-2d.

In this appendix, simulation of the Fresnel fringes of a Mo/Si multilayer using the projected charge density approximation is used to illustrate the characteristics of the fringes from different interfacial structures. Observation of the Fresnel fringes in nanometer period Mo/Si, W/C, and WC/C x-ray multilayers in the microscope is described. Through-focus-series TEM images of the fringes are analyzed in relation to the simulated results to understand the effects of the specimen and microscope conditions on the fringes. Implications of experimental and simulated Fresnel fringes on quantification of the interfacial structures are discussed.

B.3 SIMULATION OF FRESNEL FRINGES

Simulated Fresnel fringes of a 9 nm period Mo/Si multilayer is generated using the projected charge density approximation method. The simulation assumes a uniform potential for each of the layer in multilayers. Previous studies by Ness et al. indicated that uniform potential model can provide a reasonable approximation as long as the layers are weakly diffracting and there are no strongly excited g-vectors normal to the interface.[3] In x-ray multilayers, the layers are very thin and disordered so this approximation can be applied. A unit cell of the multilayer has the shape similar to that shown in B-2d. The period of the multilayer is 9 nm, with a Γ value (the ratio of the Mo layer thickness to the period) is 0.4. At the interfaces, two finite linear potential gradients are assumed for the study, with one of the slope twice as large as the other. The calculation produces line tracings of the intensity across a multilayer period, similar to the micro-densitometry traces of the experimental TEM images. Four main parameters involved in the simulated include 1) the condition of the microscope, such as defocus, tilting, and beam divergence, 2) the characteristics of the specimen such as thickness, 3) the contrast between the materials or the potential difference, and 4) the characteristics of the interfaces including the interfacial layer thickness and the abruptness of the interfacial structure. The microscope used in the simulation is the JOEL JEM 200CX operating at 200 kV, which was also used to obtain the experimental HRTEM images (Cs = 1.1 mm, DEL = 8 nm, divergence = 0.8 mr, R = 0.5, and vibration = 0). Through-focus-series of the fringes are simulated in step of 72 nm in both positive and negative defocus values.

Three different specimen thicknesses of 2, 5, and 10 nm were simulated to study the effects of specimen thickness on the intensity and spacing of the fringes. Comparisons of the thicknesses are shown in Figure B-3. In the range of specimen

thickness studied, it is found that the fringe intensity increases with the specimen thickness, although careful measurements shows that it is not a linear relationship. The fringe contrast is more intense at the interface with smaller interfacial layer thickness or higher potential gradient. The sign of the phase component of the fringes changes from positive to negative defocus, and the fringe spacing increases with specimen thickness when the phase is positive, and decreases with specimen thickness when the phase is negative.

Comparison of structures of different potential difference (ΔP), transition layer thickness (d_{tr}) and slope (m_{tr}), and their combinations, are used to study the characteristics of the fringes. Figures B-4 and B-5 show through-focus-series fringe profiles of, respectively, two specimens having different ΔP, and two specimens with same ΔP but different interfacial layer thickness or interface abruptness. Similar to the result found in Figure B-3, the fringes have higher contrast at higher defocus values, and change in sign from positive to negative defocus. The contrast or intensity is higher for larger potential difference between the layers. Change in ΔP with constant transition layer thickness, and hence change in the slope or abruptness in change of composition, does not result in significant difference in the spacing of the fringes. The profile however varies for different ΔP with the same slope from positive to negative defocus. For the same potential difference, the contrast increases with higher slope and shorter d_{tr}, while the spacing increases with lower m_{tr} and longer d_{tr}. Comparison of the fringe intensities and spacing of two different transition layer thicknesses with the same slope and hence of two different ΔP, reveals that the difference in the intensity is significantly higher for the shorter d_{tr} and higher ΔP, while the spacing is much wider in the longer d_{tr} and lower ΔP. This observation indicates that the potential difference and the abruptness of the interfacial composition change are a strong function of the fringe contrast, while the fringe spacing depends more strongly on the thickness of the transition or interfacial

layer. In summary, the simulated results indicate that the intensity of the fringes is stronger for larger defocus value, for larger potential different between the layer materials, for increased abruptness at the interfaces, and for smaller interfacial layer thickness, while the fringe spacing is closely related to the thickness of the interfacial layer.[19]

B.3 Experimental TEM Observation of Fresnel Fringes

Fresnel fringes are observed in TEM images of Mo/Si, W/C, WC/C, and many other multilayers. Figures B-6 to B-8 show HRTEM though-focus-series images and micro-densitometry traces across the interfaces of, respectively Mo/Si, W/C and WC/C multilayers. The traces are obtained from averaging 20 lines taken at approximately one nm from each other. The micro-densitometry traces show similar behaviors as those observed from the images, and they can be used for quantitative comparison with calculation to determine the interfacial profiles. Similar to the simulated results, the contrast of the fringes is higher with increasing defocus both positive and negative values from the minimum contrast condition. The fringes in the W/C and Mo/Si appear symmetrical on the two interfaces of the W-rich and Mo-rich layers signifying similar structures at high-Z/low-Z and low-Z/high-Z interfaces. The fringes in the WC/C multilayers however show different characteristics at the two interfaces of the WC-rich layers, which likely indicates different shapes of the potentials and hence of the chemistry or the composition at the two interfaces.

B.4 CONCLUSIONS

The presence of Fresnel fringes at interfaces in HRTEM images makes interpretation of the interfacial structure difficult. The effects are more dramatic in x-ray multilayers where the difference between the scattering potentials of the layer materials is large. The larger the difference the greater the effects of the fringes on the images. Fresnel fringes are visible at when imaging these multilayers at optimum defocus, and thus quantification of the interfacial structure difficult. Simulation of the fringes however can help to understand the characteristics of these fringes. Comparisons of different properties of interfaces, such as potential difference, interfacial layer thickness, and abruptness of the compositional gradient, provide an understanding of the fringes. Comparisons of the experimental fringes to the simulated profiles are possible to obtain quantitative information on the interfacial structures. The difficulty however lies on the accurate knowledge of the specimen thickness in modeling of the fringes.

B.5 REFERENCES

1. D.R. Clark, Ultramicroscopy **4** (1979) 33.
2. N.W. Jepps, T.F. Page, and W.M. Stobbs, in: Grain boundaries in semiconductors, Eds. H.J. Leamy et. al. (North-Holland, Amsterdam, 1982) 45.
3. J.N. Ness, W.M. Stobbs, and T.F. Page, Phil. Mag. **54** (1986) 679.
4. D.R. Rasmussen et. al., Ultramicroscopy **30** (1989) 52.
5. M. Ruhle, and S.L. Sass, Phil. Mag. **49** (1084) 759.
6. C.B. Boothroyd, and W.M. Stobbs, Phil. Mag. **A49**, 1 (1984) L5.
7. L.A. Bursill, J.C. Barry, and T.R.W. Hudson, Phil. Mag. **A37** (1978) 789.
8. W.M. Stobbs, and D.J. Smith, in EMA (Inst. of Phys., London, 1981) 373.
9. G.J. Wood, W.M. Stobbs, and D.J. Smith, Phil. Mag. **A50** (1984) 375.
10. W.M. Stobbs, G.J. Wood, and D.J. Smith, Ultramicroscopy **14** (1984) 145.

11. C.S. Baxter, and W.M. Stobbs, Ultramicroscopy **16** (1985) 213.
12. C.B. Boothroyd, and W.M. Stobbs, Phil. Mag. **54** (1986) 663.
13. F.M. Ross, and W.M. Stobbs, MRS Proc. **105** (1988) 259.
14. C.B. Boothroyd et. al., Ultramicroscopy **29** (1989) 18.
15. C.S. Baxter and W.M. Stobbs, Appl. Phys. Lett. **48** (1986) 1202.
16. W.M. STobbs, in Mat. Res. Soc. Symp. Proc. Vol. **103** (1988) 121.
17. W.C. Shih and W.M. Stobbs, Ultramicroscopy **32** (1990) 219.
18. T.D. Nguyen, R. Gronsky, and J.B. Kortright, ICEM Proc. **4** (1990) 442.
19. Simulation of the fringes is a collaborative project with M.A. O'Keefe and R. Kilaas at the National Center for Electron Microscopy, Lawrence Berkeley Laboratory.

B.6 FIGURES

Figure B-1. Over focus cross-sectional HRTEM image of 4 nm period W/C multilayer showing the presence of Fresnel fringes at the interfaces.

Figure B-2. Different potential gradients at interfaces.

Figure B-3. Comparison of simulated fringes of 2, 5 and 10 nm thick sepcimens.

Figure B-4. Comparison of different potential difference ΔP.

Figure B-5. Comparison of different interfacial layer thickness.

Figure B-6. Experimental TEM through-focus-series images and their micro-densitometry traces of a 9 nm period Mo/Si multilayer.

Figure B-7. Experimental TEM through-focus-series images and their micro-densitometry traces of a 7 nm period W/C multilayer.

Figure B-8. Experimental TEM through-focus-series images and their micro-densitometry traces of a 7 nm period WC/C multilayer, showing the asymmetry of the fringes on the two sides of the WC layers.

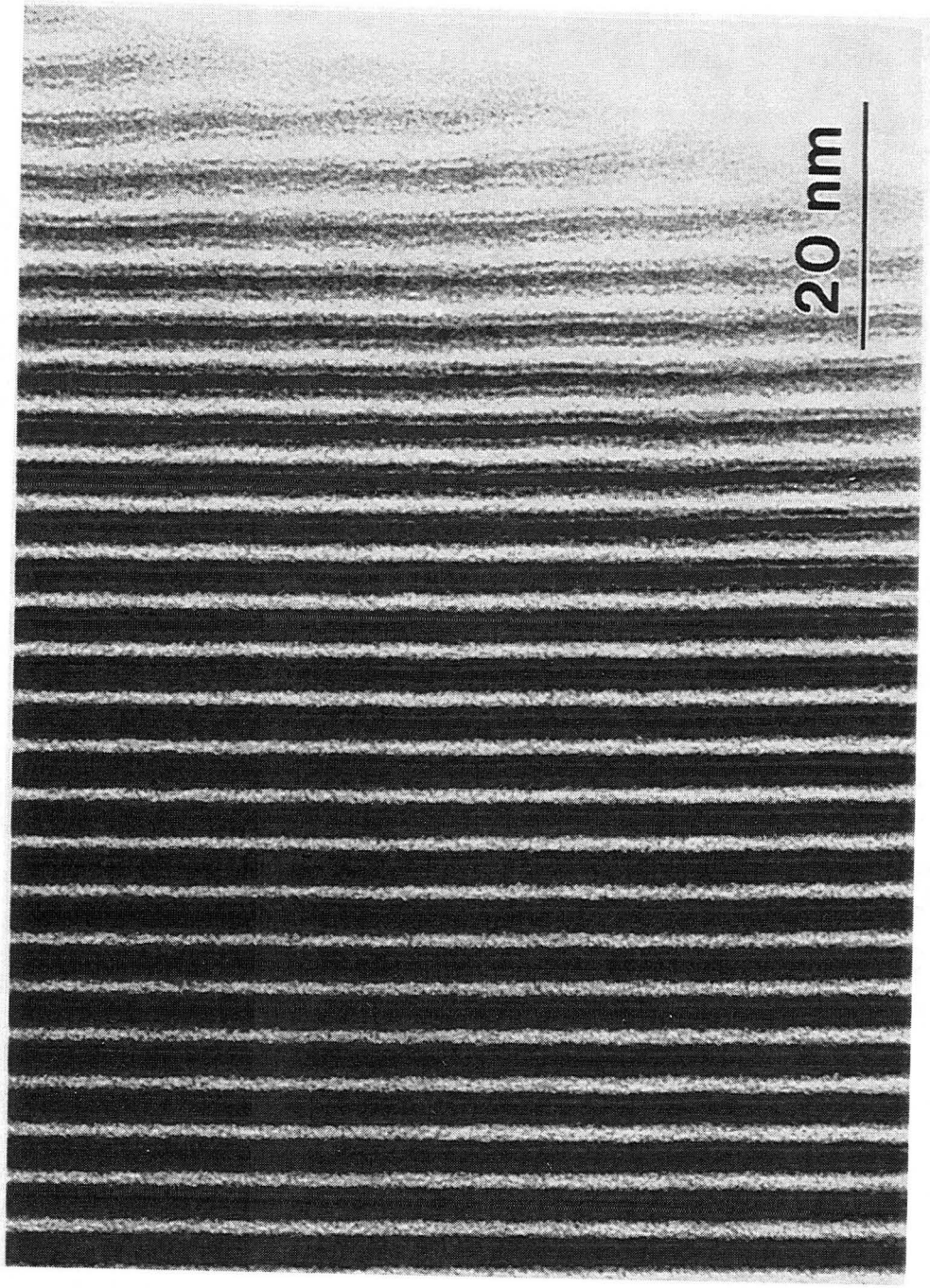
20 nm

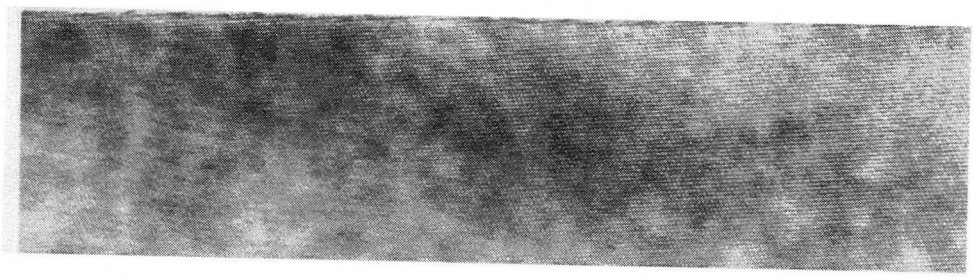

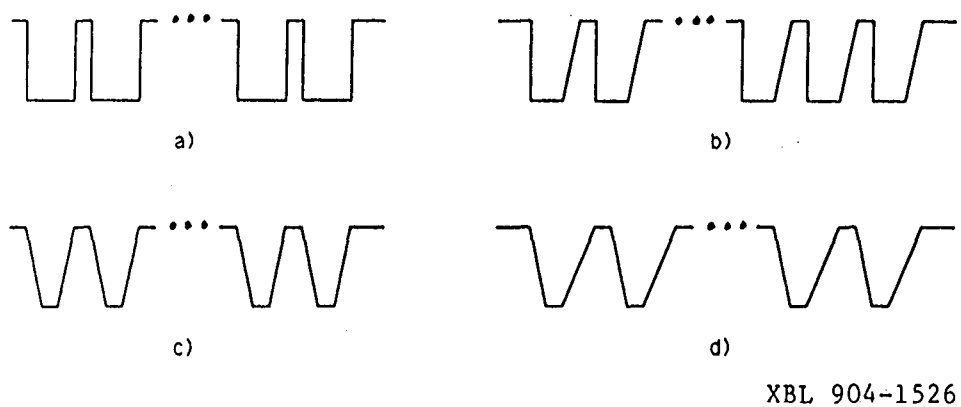

Figure B-2

Fringe intensity increases with increasing sample thickness

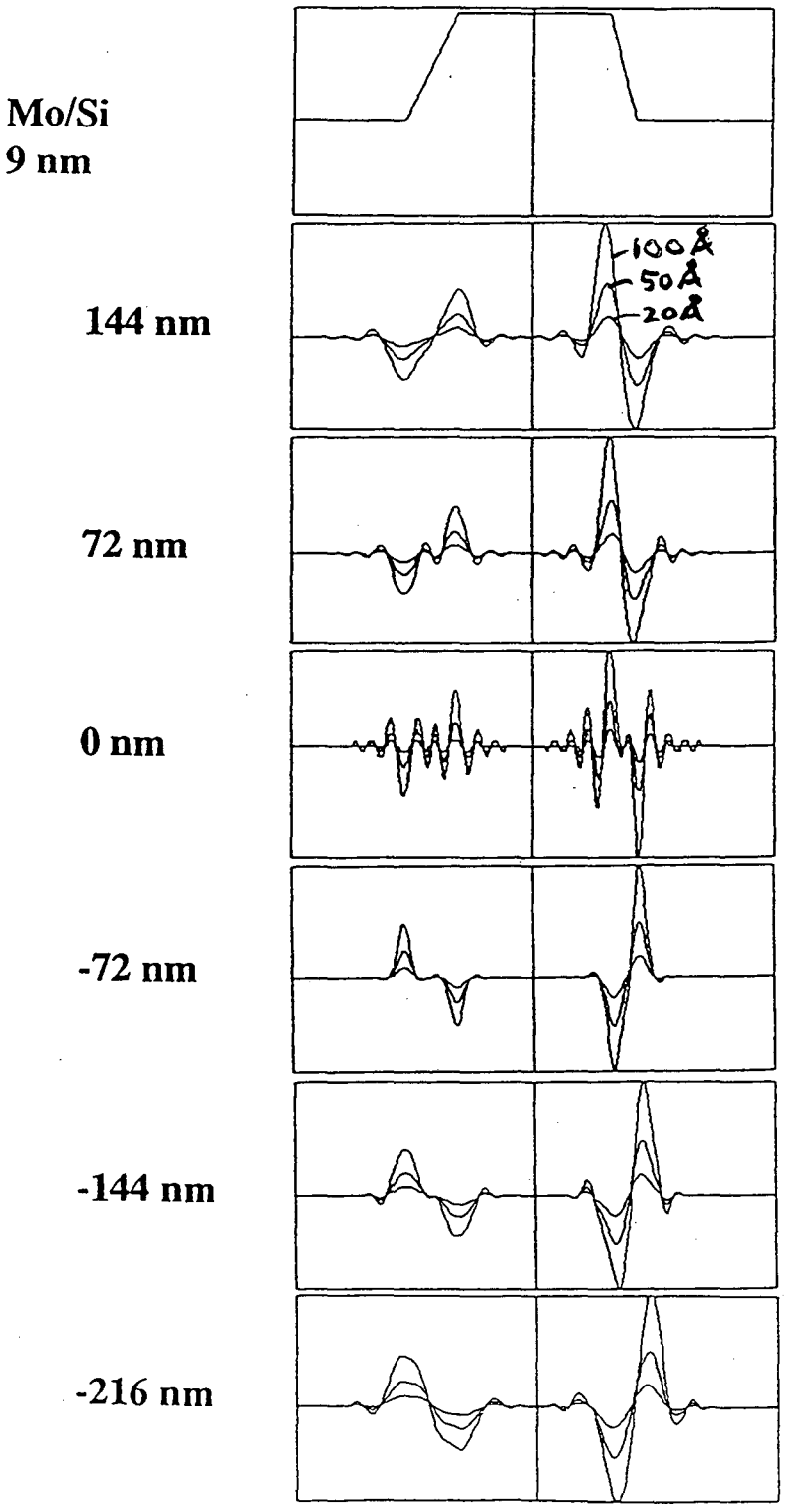

Figure B-3

Higher fringe contrast for larger potential difference (ΔP)

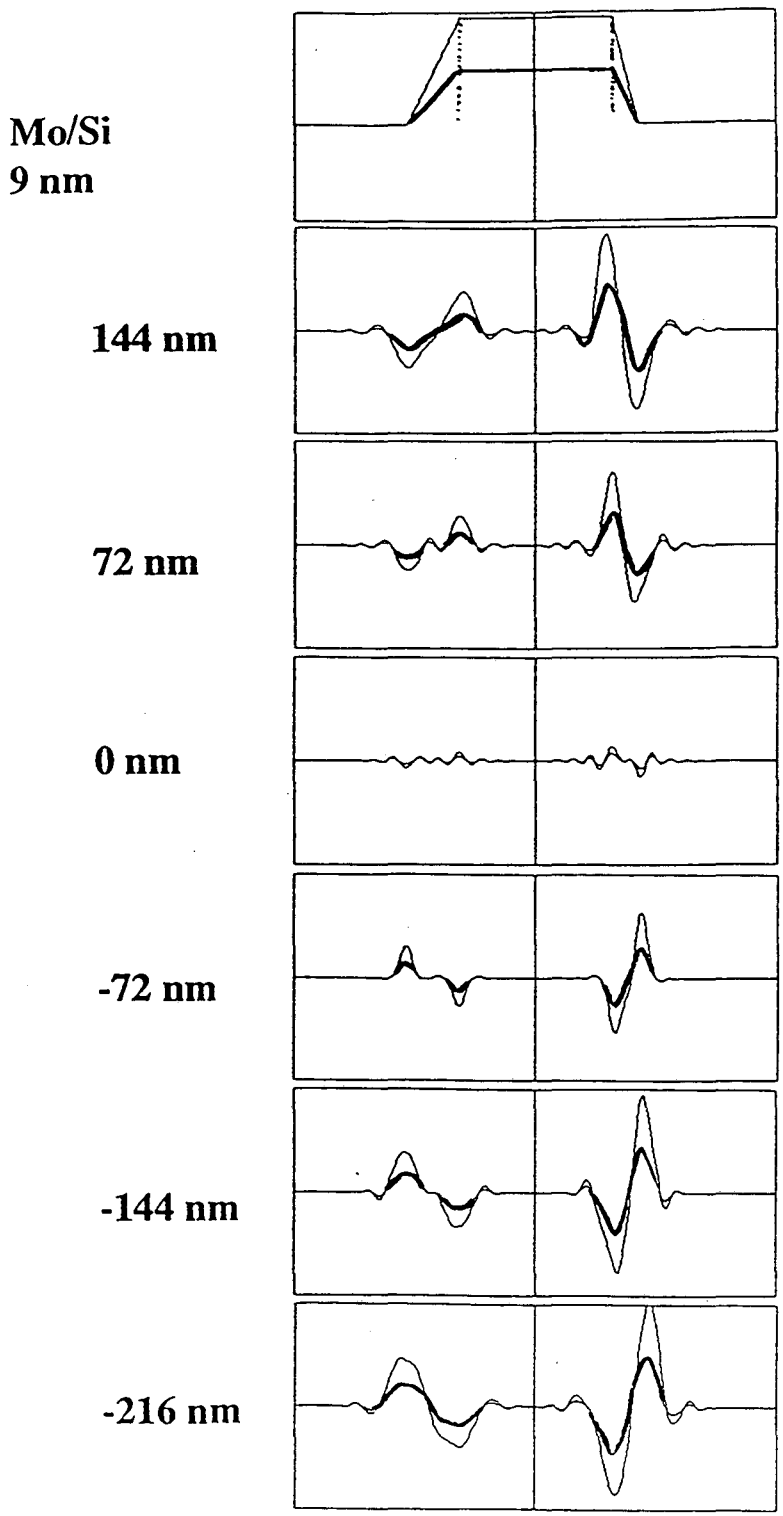

Figure B-4

Comparison of compositional abruptness at interfaces

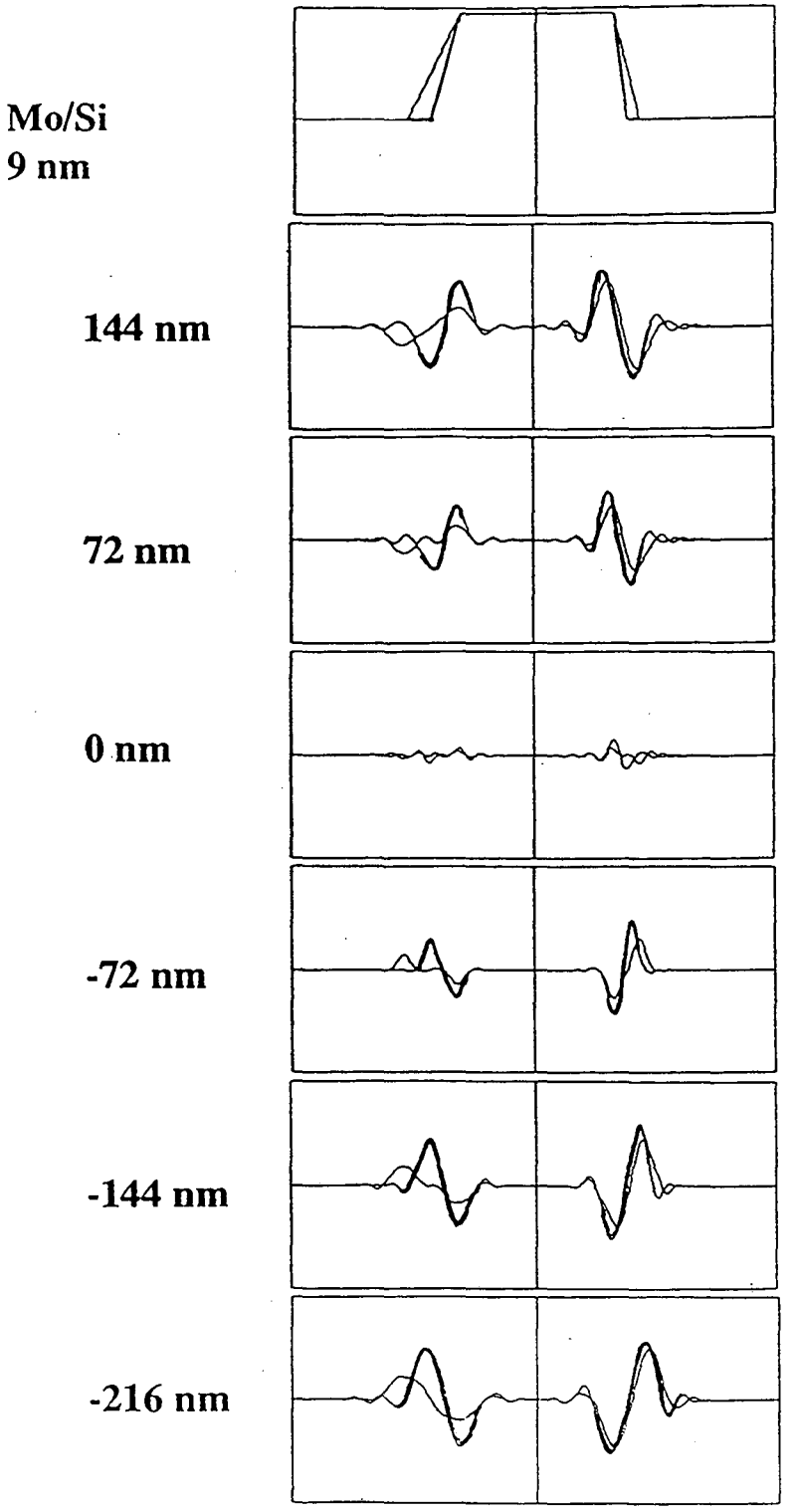

Figure B-5

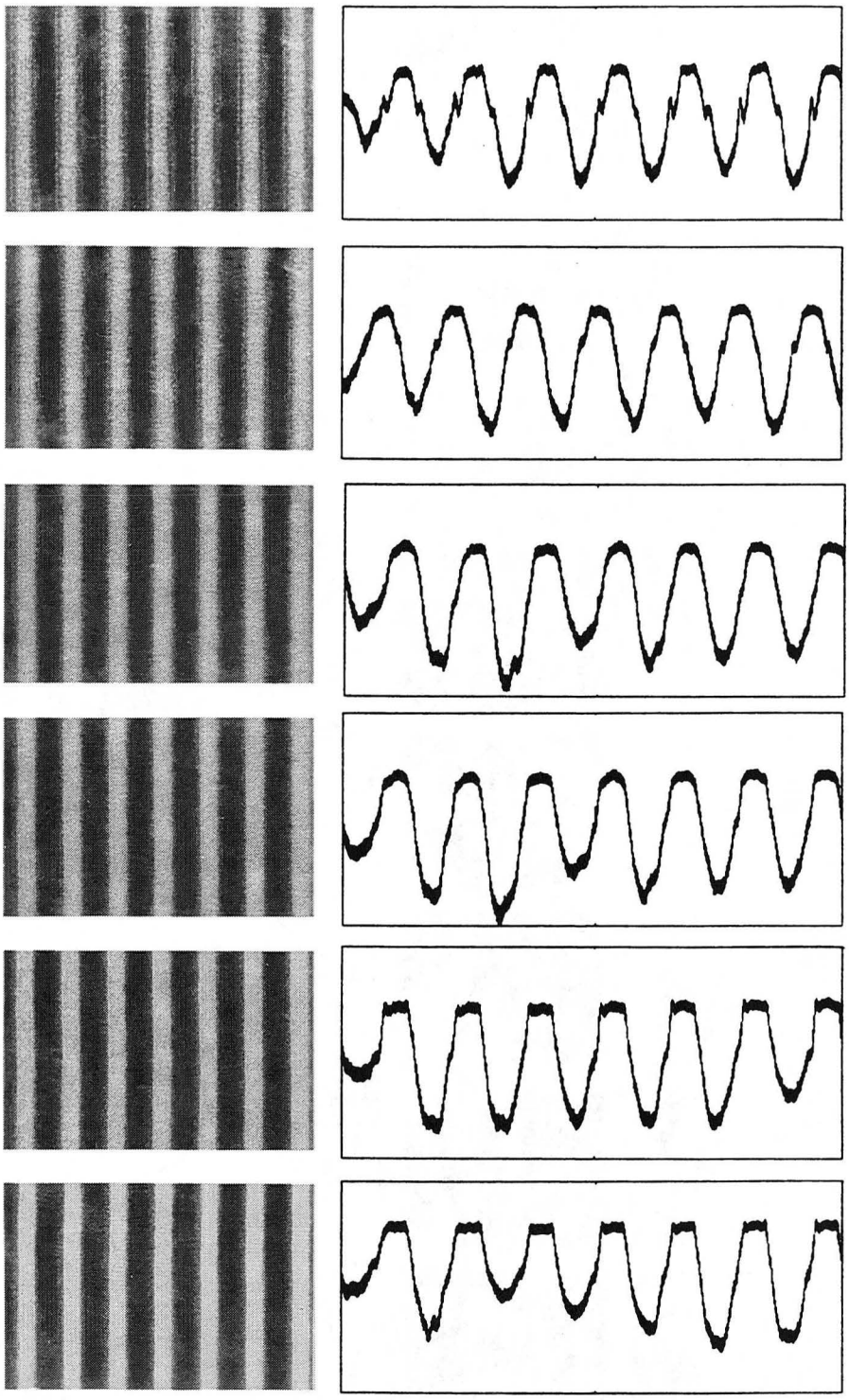

Figure B-6

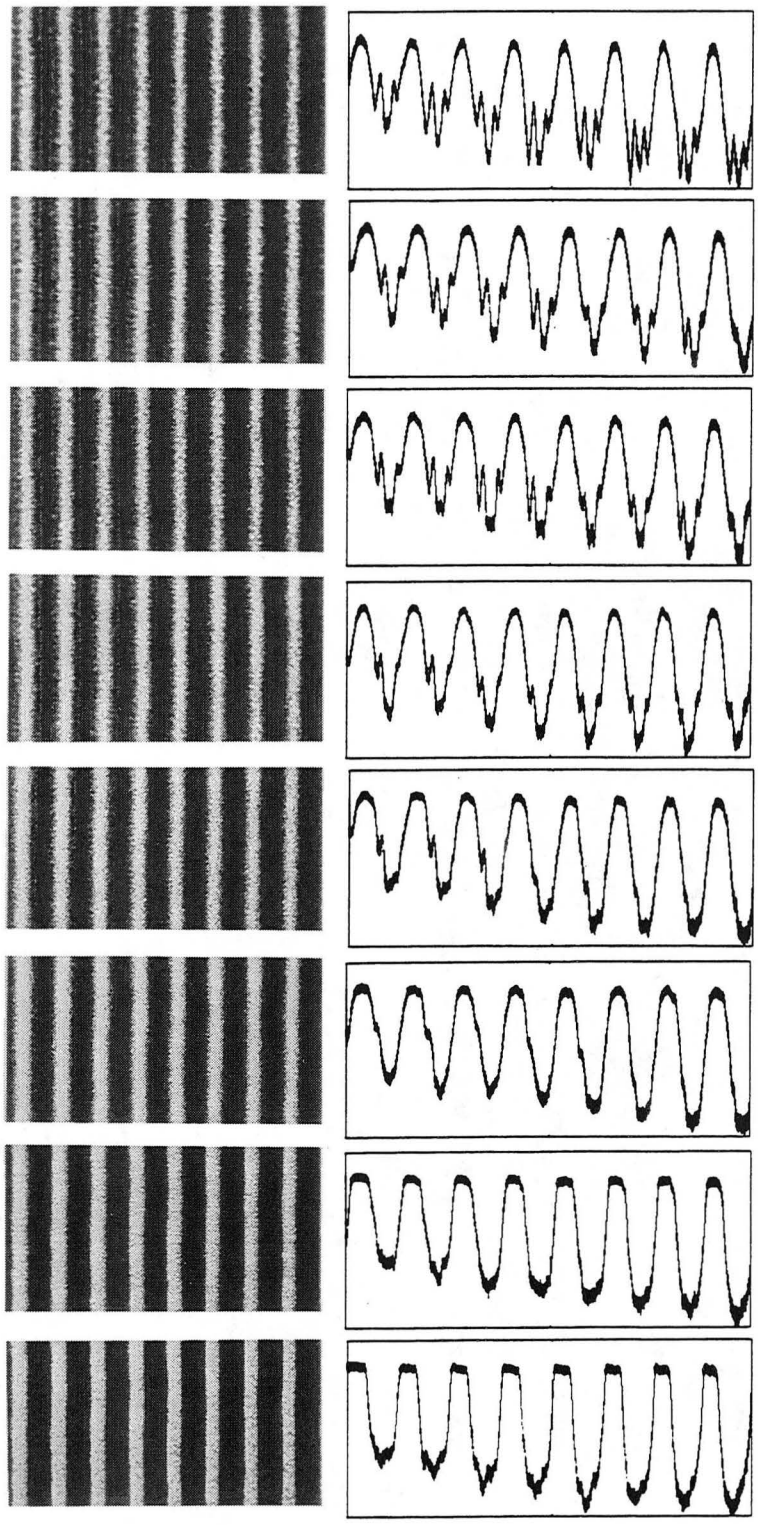

Figure B-7

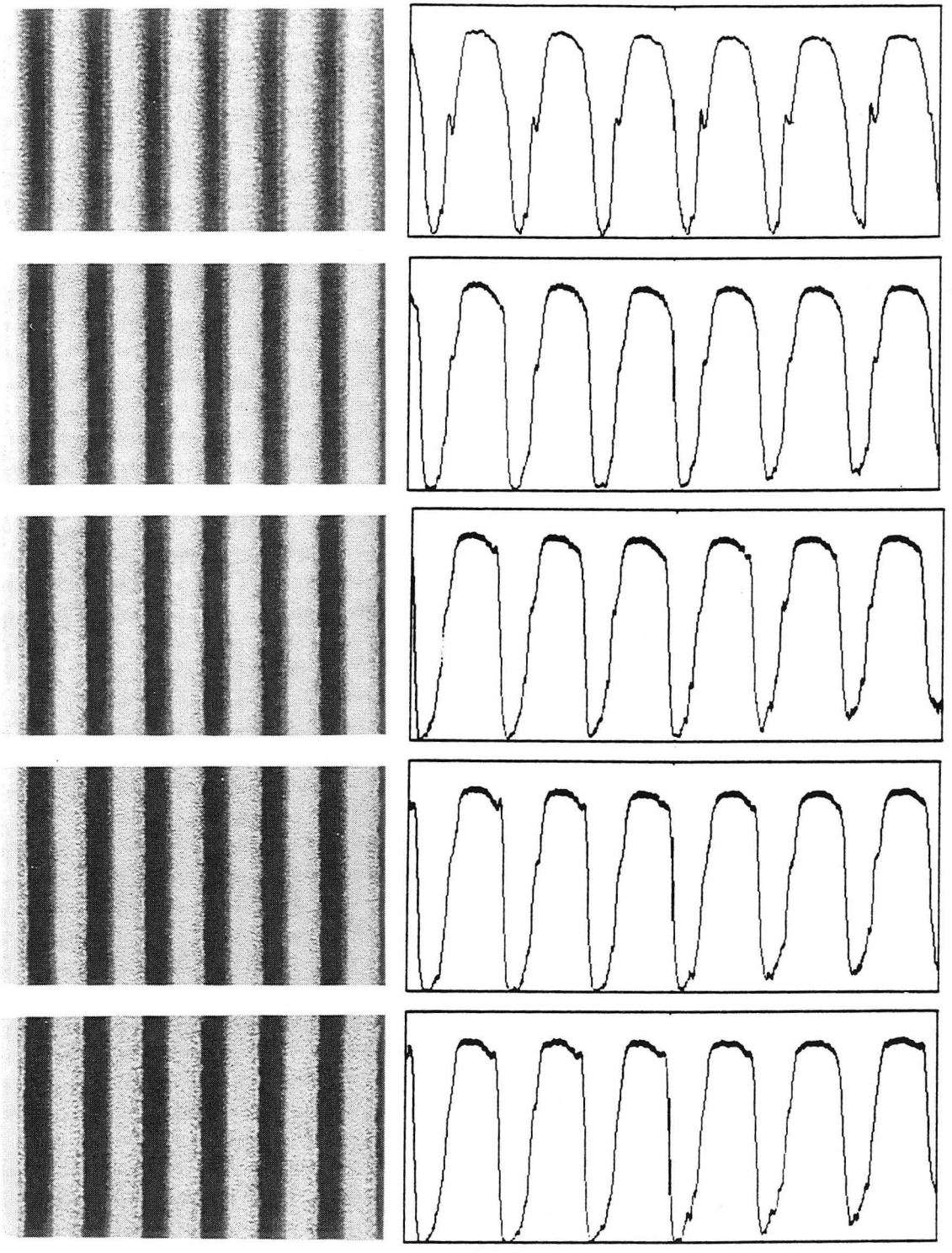

Figure B-8

ERNEST ORLANDO LAWRENCE BERKELEY NATIONAL LABORATORY
ONE CYCLOTRON ROAD | BERKELEY, CALIFORNIA 94720

Prepared for the U.S. Department of Energy under Contract No. DE-AC03-76SF00098